

Master of Science Thesis

Aeroacoustics and Flow Dynamics of an airfoil with a Gurney Flap

A study using Time-Resolved Particle Image Velocimetry

Jiggar Shah

October 16, 2015

Aeroacoustics and Flow Dynamics of an airfoil with a Gurney Flap

A study using Time-Resolved Particle Image Velocimetry

Master of Science Thesis

For obtaining the degree of Master of Science in Aerospace Engineering
at Delft University of Technology

Jiggar Shah

October 16, 2015



Delft University of Technology

Copyright © Aerospace Engineering, Delft University of Technology
All rights reserved.

DELFT UNIVERSITY OF TECHNOLOGY
DEPARTMENT OF AERODYNAMICS

The undersigned hereby certify that they have read and recommend to the Faculty of Aerospace Engineering for acceptance the thesis entitled “**Aeroacoustics and Flow Dynamics of an airfoil with a Gurney Flap**” by **Jiggar Shah** in fulfillment of the requirements for the degree of **Master of Science**.

Dated: October 16, 2015

Supervisors:

Prof. Dr. Fulvio Scarano

Dr. Andrea Sciacchitano

Dr. Stefan Pröbsting

Dr. Gerrit E. Elsinga

Preface

This thesis marks the end of my MSc education in Aerodynamics and Wind Energy at TU Delft. At this point, I would like to thank a number of people who have helped me throughout my studies here.

I would like to thank Prof. Fulvio Scarano for introducing me to the promising field of Particle Image Velocimetry and his useful suggestions throughout the thesis.

To my advisor, Andrea Sciacchitano, I would like to express my deep gratitude for being an excellent mentor and for always finding the time to help. Thank you Andrea for teaching and guiding me throughout the thesis.

Many words of gratitude to Stefan Pröbsting for his friendly guidance and discussions on aeroacoustics. I would like to thank all the technicians in the aerodynamics department, their help is greatly appreciated.

To all the friends I made during my time in Delft, Thank you! A special mention is due to Remco, Koen, Eelco, Vinod, Ananth, Stevie, Caddie, Vishy, Stefano, Martina, Juriaan, Jaap, Tim, Tipnis, Lucas and Pieter. I have learnt a lot from you and you all made my time really enjoyable. Thank you for all the great memories!

Most importantly, I would like to thank my wonderful family for their unconditional love and support. Thank you for putting up with all the frustrations associated with me studying abroad. This thesis is dedicated to you.

Jiggar Shah
Delft,
12th October 2015

Abstract

Aircraft noise has come under severe scrutiny due to growing number of airports and airline operations. The noise generated by high lift devices is now comparable to the turbofan engines due to increasing bypass ratios. A Gurney flap is a suitable starting point to study trailing edge flap aeroacoustics due to additional lift characteristics and a simple geometry. The thesis aims in using Time-Resolved Particle Image Velocimetry to understand the dynamics of flow as well as identifying structures responsible for the tonal noise in a Gurney flap.

TR-PIV was used to obtain, at a high spatial and temporal resolution, the flow dynamics associated with a Gurney flap at low Mach and high Reynolds number. A part of the thesis focussed on validating the two modes of shedding as an additional lift increment mechanism in a Gurney flap in case of a fully developed turbulent boundary layer. Flow statistics showed an upstream recirculation region, upper and lower separating shear layers and a main recirculation region whose size varied with Gurney flap size and angle of attack downstream of the flap. The instantaneous velocity and vorticity fields showed the flapping motion of the von Kármán wake and corresponding vortex roll-up and shedding process. The power spectral density of flow fluctuations as well as the acoustic spectra, however, did not indicate any second mode of shedding. The Strouhal numbers of the vortex shedding for various Gurney flaps were close to that of a bluff body in a flow. Stereoscopic PIV measurements showed the periodic vortex shedding to be highly correlated in the spanwise direction (correlation length of 4cm). The large spanwise correlation length indicates the use of serrations can be useful in breaking-down such coherent structures.

The tonal peaks were clearly audible and correspond to the vortex shedding frequency. *Causality correlation* between pressure fluctuations generated in the far-field and the near-field fluctuations indicate a high correlation with unsteady vertical velocity in the wake (associated with unsteady lift). It was found that the dynamics in the upstream recirculation region (cavity) was not responsible in the production of noise. Further, the results indicate the location of the actual source of noise to be the flap. The high values of correlation further downstream are due to the presence of an upstream source (the flap) and are not sources of sound themselves. Thus, TR-PIV in a way clears the ambiguity expressed by other researchers in the past in interpreting the high values of correlation to be sources of sound.

Table of Contents

Preface	v
Abstract	vii
List of Figures	xiii
List of Tables	xix
1 Introduction	1
2 Background	5
2.1 Gurney Flap	5
2.1.1 Flow Structure	8
2.1.2 Lift increment mechanisms	11
2.2 Aeroacoustics	14
2.2.1 Properties of Sound	14
2.2.2 Mechanisms of noise generation	15
2.2.3 Approach	16
2.2.4 Aeroacoustic Analogies	17
2.3 Research Objectives	22
3 Experimental Techniques and their application in Aeroacoustics	23

3.1	Flow Measurement: Particle Image Velocimetry	23
3.1.1	Working Principle	23
3.1.2	Tracer fidelity	24
3.1.3	Illumination	25
3.1.4	Particle Imaging	26
3.1.5	Evaluation of particle image motion	27
3.1.6	Stereo - PIV	28
3.1.7	Time Resolved - PIV	28
3.2	Acoustic Measurement: Microphones	29
3.2.1	Acoustic source localization	30
3.2.2	Array Resolution	30
3.3	PIV and Aeroacoustics	31
3.3.1	Causality correlation applied to a Cylinder	37
3.3.2	Causality correlation applied to a Rod - Airfoil	40
3.3.3	Causality correlation applied to a Slat: High Lift Device	42
3.4	Data Reduction	45
3.4.1	Spectral Analysis	46
3.4.2	Proper Orthogonal Decomposition	48
4	Experimental Set-up	49
4.1	Wind tunnel facility	49
4.2	Models and Test section	50
4.3	Planar PIV set-up	51
4.4	Stereo PIV set-up	54
4.5	Microphone Measurements	55
4.6	PIV image processing	56
5	Results	57

Table of Contents	xi
5.1 Characterization of the Boundary layer	57
5.2 Flow Statistics	60
5.3 Flow dynamics: Time Resolved	63
5.4 Power Spectral Density	69
5.5 Proper Orthogonal Decomposition	73
5.6 Causality Correlation	74
5.7 Coherence	82
5.8 Spanwise correlation length: Stereoscopic PIV	83
6 Conclusions	85
Bibliography	91

List of Figures

1.1	An airplane landing at Heathrow Airport and aircraft noise source during landing	1
1.2	Aircraft engine noise reduction	2
1.3	High lift flaps	3
1.4	CATIA model of an airfoil with a Gurney flap	3
2.1	Gurney flap on a Porsche sports car [10]	5
2.2	Gurney flap on the tail section of a Bell 222U(top),Apache(bottom) Helicopter, [11]	6
2.3	Wing with MiTEs [12]	6
2.4	Microtab load control in a wind turbine blade [15]	6
2.5	Flow structure in the vicinity of the Gurney flap	8
2.6	Smoke flow visualization[22]	9
2.7	Strouhal frequency: LDV for e423 wing [22]	9
2.8	Bimodal vortex shedding [32]	10
2.9	Spectral analysis PIV, Hot Wire [32]	10
2.10	Summary of primary and secondary Strouhal numbers [33]	11
2.11	Lift, drag coefficients, L/D ratio and velocity profile [28]	12
2.12	Pressure distributions over an airfoil with a Gurney flap [28]	13
2.13	Different mechanisms of noise generation	15
2.14	Aeroacoustics: Different approaches	16

2.15	Instantaneous pressure perturbation for a heated coaxial jet [43]	17
2.16	Source and Listener location in Lighthill's analogy [44]	19
2.17	Source and sound scales [41]	20
3.1	A typical PIV experimental set up and its working principle [46]	24
3.2	Intensity of scattered light ($1\mu\text{m}$ particle) [46]	25
3.3	Particle imaging optics (modified from Raffel <i>et al.</i> [46])	26
3.4	Particle image evaluation [48]	28
3.5	Typical setup of Stereo-PIV reproduced from Tropea <i>et al.</i>	29
3.6	Condensor Microphone	29
3.7	Wind turbine noise source [2]	30
3.8	Principle of Array beamforming [51]	30
3.9	Aeroacoustics of cavity using TR-PIV [54]	31
3.10	Jet aeroacoustics using 4D PIV [57]	32
3.11	Second temporal derivative of Lamb Vector spatial distribution along jet axis [57]	32
3.12	Velocity, reconstructed pressure and predicted far-field noise spectrum for a Rod-airfoil case [59]	33
3.13	Understanding the main sources of noise	34
3.14	Normalized correlation coefficients for $u, \rho u u$ measured at $x/D=10$ and centerline of $M=1.4$ jet, [65]	35
3.15	Peak correlation coefficients for high speed jet [65]	35
3.16	Schematic for experimental set-up in cylinder case [60]	37
3.17	Time sequence of the recorded sound pressure and corresponding acoustic power spectrum (Henning <i>et al.</i>)	37
3.18	Instantaneous distribution of normalized cross correlation coefficient ($R_{\omega',p'}$) and $R_{u',p'} R_{v',p'}$ [60]	38
3.19	Temporal evolution of normalized cross correlation coefficient and corresponding cross spectrum [60]	38

3.20	Instantaneous distribution of correlation coefficient using coefficients/amplitude time series of different eigenmodes (1-top left, 2-top right, 3-bottom left) $R_{v'p'}$ and spectra using amplitude time series of the 1st eigenmode [60]	39
3.21	Flow statistics and acoustic spectrum [66]	40
3.22	Maximum correlation coefficient $R_{v',p'}$ for Rod-Airfoil case [66]	41
3.23	Temporal evolution of normalized cross correlation coefficient and corresponding cross spectrum [66]	41
3.24	Cross section of the F16 wing model used to study slat noise [68]	42
3.25	Mean velocity vector maps for different angles of attack [68]	42
3.26	Acoustic spectrum for different angles of attack [68]	43
3.27	Spatial distribution of the maximum coefficient values $R_{vp}(x, \tau)$ [68]	43
3.28	Instantaneous distribution of $R_{vp}, \tau = 0$ [68]	44
3.29	Space-time distribution of Correlation coefficient for Rod-airfoil case [66]	44
4.1	Schematic diagram: Vertical Wind Tunnel [74]	49
4.2	Gurney flap models manufactured at TU Delft	50
4.3	Test Section for PIV (left), Acoustics (right)	50
4.4	Schematic diagram for the Planar PIV set-up (shown without the test section for clarity)	51
4.5	Photograph of the experimental set up to acquire simultaneous measurements	52
4.6	Photograph of the set-up showing the camera positions and the far-field microphones	53
4.7	Schematic diagram for the Stereoscopic measurements	54
4.8	Photograph of the stereoscopic PIV set-up	54
4.9	Microphones used for far-field acoustic measurement	55
4.10	Velocity field obtained at camera 1 (left), camera 2 (right)	56
4.11	The stitched velocity field	56
5.1	Measured Boundary layer on the suction side of GF4-AOA4-V30 (left) u component (right) v component	58

5.2	Boundary layer velocity profile at $x/c=0.97$, (left) dimensional wall distance (right) normalized with boundary layer thickness, y/δ	58
5.3	A typical turbulent boundary layer profile(blue-not measured),(red-measured using PIV)	59
5.4	Flow statistics for GF6-AOA8-V30, \bar{u} (top left), \bar{v} (top right), u'_{rms} (bottom left) v'_{rms} (bottom right) at $Re_c = 0.4$ million	60
5.5	GF6-AOA8-V30: Streamlines	61
5.6	Time averaged velocity field: \bar{u} for different cases (top left, top right: GF% decrease; top left, bottom left: Re decrease; top left, bottom right: α increase)	61
5.7	RMS velocity field: v'_{rms} for different cases (top left, top right: GF% decrease; top left, bottom left: Re decrease; top left, bottom right: α increase)	62
5.8	RMS velocity field: u'_{rms} for different cases (top left, top right: GF% decrease; top left, bottom left: Re decrease; top left, bottom right: α increase)	63
5.9	Instantaneous u component at different time instants: GF6-AOA8-V30 at $Re_c = 0.4$ million	64
5.10	Instantaneous v component at different time instants: GF6-AOA8-V30 at $Re_c = 0.4$ million	65
5.11	Instantaneous ω_z component at different time instants: GF6-AOA8-V30 at $Re_c = 0.4$ million	66
5.12	Instantaneous L_x component at different time instants: GF6-AOA8-V30 at $Re_c 0.4$ million	67
5.13	GF6-AOA8-V30: v component, A, B and C are locations where PSD is calculated	69
5.14	PSD v component: GF6-AOA8-V30; The amplitude of the power spectrum calculated here is not scaled, the plots are mainly to show different frequencies	69
5.15	Power spectrum of far-field pressure fluctuations measured on the suction side microphone: Varying α , Varying Re , Varying GF % Size and Shedding frequency/St values	70
5.16	Values of primary von Kármán shedding frequency and corresponding Strouhal number of far-field pressure fluctuations measured on the suction side microphone	71
5.17	Frequency peak of PIV and microphone for the GF6-AOA8-V30 case at position C	72
5.18	Shape of the first, second and third POD modes along with the distribution energy, (A scaling for the velocity fields is applied), $Re_c = 0.4$ million	73
5.19	Maximum value of $R_{v'p'}(X, Y, \tau)$ for the GF6-AOA8-V30 (pressure side microphone)	74
5.20	Maximum value of $R_{\omega'v',p'}(x, y, \tau)$, $R_{\omega'v',p'}(x, y, \tau)$ for GF6-AOA8-V30	75

5.21	Maximum value of $R_{v'p'}(X, Y, \tau)$ by varying Re , α and GF %	76
5.22	$R_{v'p'}(\tau)$ as a function of τ at Point C(X,Y:32.5,5) in the wake	77
5.23	$R_{v'p'}(\tau)$ at Point C (zoomed in)	77
5.24	Contour plot of $R_{v'p'}(\tau)$ at different τ shift	78
5.25	Contour plot of $R_{\omega'p'}(\tau)$ at different τ shift	79
5.26	Contour plot of $R_{\omega'v',p'}(\tau)$ at different τ shift	80
5.27	Contour plot of the magnitude square-coherence $\gamma_{v',p'}^2$ at shedding frequency and the corresponding phase difference plot	82
5.28	Schematic showing the v component for the GF6-AOA4-V20 case (video available in the online version)	83
5.29	Streamwise mean flow, \bar{u} for GF6-AOA4-V30 case	84
5.30	Spanwise Correlation length obtained for GF6-AOA4-V20/30 cases	84
6.1	Flap side edge noise: Transavia flight landing at Rotterdam Airport	87
6.2	Non-simultaneous measurement GF6-AOA8-V30: Maximum value of $R_{v'p'}$ and as a function of τ , $R_{v'p'}(\tau)$	89
6.3	Simultaneous measurement, Correlation - Maximum value of $R_{v'p'}$ (top left) and $R_{v'p'}(\tau)$ (top right), Cohrence: $\gamma_{v',p'}$ at shedding frequency and the corresponding phase difference plot	90

List of Tables

4.1	Boundary layer: 2C-PIV recording and flow parameters	52
4.2	Simultaneous, synchronized measurements: 2C-PIV recording and flow parameters	53
4.3	Stereoscopic Measurements: 3C-2D PIV recording and flow parameters	55
5.1	Boundary layer properties at $x/c=0.97$	59
5.2	Boundary layer division (Pope [77])	59
5.3	Strouhal numbers calculated using the distance between the shear layers	71

Chapter 1

Introduction

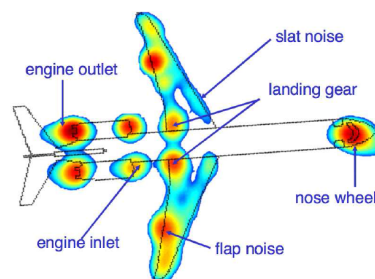
Turbulence is the most important unsolved problem of classical physics.

Richard Feynman

A thorough understanding of aerodynamics is essential to *accurately* quantify lift, drag, moments, boundary layer properties and heat transfer when airflow passes through wings, helicopter rotor blades and other lifting surfaces. In general, fluid flows are governed by the Navier-Stokes equations. These equations are complicated and the current understanding of them is very limited. They are part of the ‘Millennium Prize Problems’ in mathematics and so far, a mathematical theory that gives an insight into existence and smoothness of a solution to these equations has not been developed except for few simple cases. The non-linearity of these governing equations makes fluid phenomena like turbulence, flow induced noise, hard to understand.



(a) Residential areas near airport [1]



(b) Aeroacoustic noise source [2]

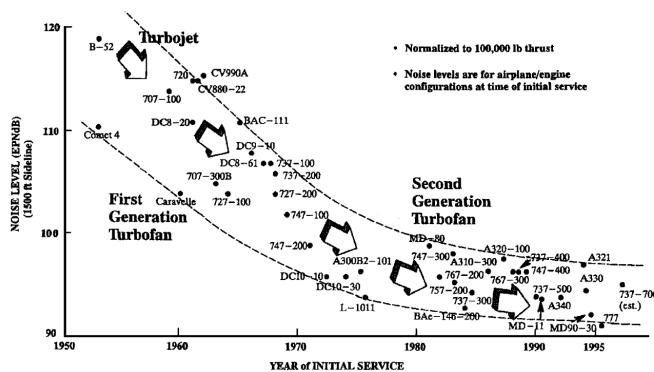
Figure 1.1: An airplane landing at Heathrow Airport and aircraft noise source during landing

Current research aims in developing an understanding of flow induced noise which remains to be a serious problem in many engineering applications. In most applications noise causes human discomfort and a prolong exposure to noise has a detrimental effect on human health [3]. In other applications flow induced noise in addition to being a nuisance also causes unwanted interference like in military operations which involve stealth or use of sonar.

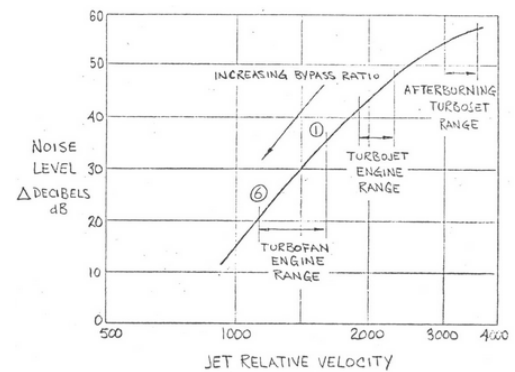
Motivation

Today, air traffic is growing rapidly due to an ever increase in demand for transportation. As a result, there is a tremendous increase in noise pollution in residential areas closer to airports (Figure 1.1(a)). This has led aeronautical certification authorities impose stricter noise regulations and penalties to airlines which do not fulfil these regulations [4]. This in turn has driven research in the area of aeroacoustics which deals with understanding aerodynamically generated sound [5].

Unfortunately, peak noise from an aircraft comes during its landing and take off phase. The main sources of aircraft noise are the engines and airframe [6]. Noise from the engine depends on the jet exhaust velocity (eighth power law, Lighthill). In order to achieve a certain amount of thrust a turbofan jet engine requires lower exhaust jet velocity as compared to the earlier turbojet engines since thrust is also generated by the fan. This makes turbofan engines not only more efficient but also reduces the noise level significantly as shown in 1.2(a) [7, 8]. At present, turbofan engines with increasing bypass ratios are expected to reduce noise levels even further (Figure 1.2(b)).



(a) Aircraft noise reduction [7]

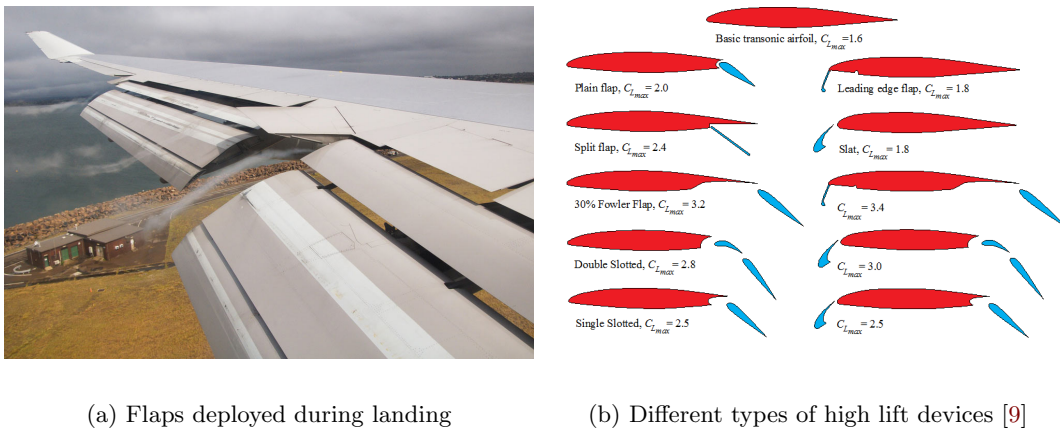


(b) Exhaust noise level Vs Jet Velocity

Figure 1.2: Aircraft engine noise reduction

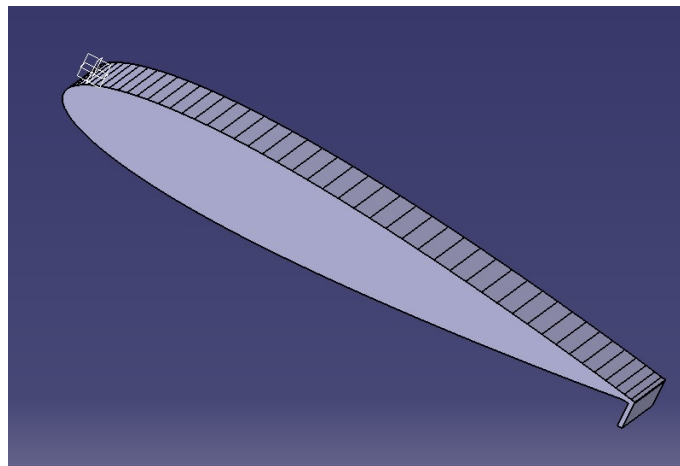
Airframe noise includes noise generated by high lift devices and landing gear. Aircraft need high lift devices like flaps as shown in Figure 1.3 and slats in order to sustain flight by increasing lift at lower speed which occur during take off and landing. The noise generated by high lift devices and landing gears is now comparable to the engines as shown in Figure 1.1(b) [2]. This has motivated research in the area of trailing edge aeroacoustics.

High lift devices increase $C_{l,max}$ by increasing camber, effective wing area and by re-energizing the boundary layer due to presence of slots as shown in Figure 2.7(a). These devices make steeper ascent after take off possible which help in reducing fuel consumption and mitigate noise to the surrounding areas. The different types of trailing edge flaps are also shown in Figure 1.3(b). Most modern aircraft use a double slotted Fowler flap with a slat. These flaps have a complicated geometry and are expensive to manufacture. On the other hand, a Gurney flap is a flat plate located at the trailing edge of an airfoil which is perpendicular to the chord as shown in 2.11(d). Due to its simple geometry (low manufacturing costs) and similar lift characteristics when compared to a complex flap, the Gurney flap is a suitable starting point to study trailing edge flap aeroacoustics. To the knowledge of the author, an aeroacoustic study on a Gurney flap has not been performed so far.



(a) Flaps deployed during landing

(b) Different types of high lift devices [9]

Figure 1.3: High lift flaps**Figure 1.4:** CATIA model of an airfoil with a Gurney flap

The next chapter describes the current understanding on Gurney flaps and aeroacoustics. It also discusses the research objective of the thesis. Chapter 3 describes the experimental techniques, its application in aeroacoustics and the data reduction methods that are used in

the thesis. The experimental set up is presented in Chapter 4 and the results obtained from the experimental campaigns are presented in Chapter 5. In Chapter 6, the general conclusions of the investigation are drawn and recommendations for further study are discussed.

Chapter 2

Background

Science is nothing but perception.

Plato

The introduction chapter described the main motivation to study trailing edge flap aeroacoustics using a Gurney flap. In this chapter, relevant background on Gurney flaps is introduced. Particular attention is paid to the flow structure around the Gurney flap and the different lift increment mechanisms. Thereafter, the fundamental aspects of an aeroacoustic study are discussed. An overview of a variety of approaches for aeroacoustic investigations is presented. Finally, the research objectives for the thesis are presented.

2.1 Gurney Flap

A Gurney flap was first added to a race car by Dan Gurney in the 1970's in order to increase downforce. This increased traction made faster turns at corners possible. It was the first aerodynamic innovation which originated from race cars and applied to the aerospace industry.

Gurney flaps are sometimes used in helicopters to improve aerodynamic performance during climb (AH-64 Apache), increase lift and reduce control input (Sikorsky S-76), or correct angle of incidence (Bell Jet Ranger) [11].



Figure 2.1: Gurney flap on a Porsche sports car [10]

Future aircraft design concepts include the development of Miniature trailing edge effectors (MiTEs). These are Gurney flaps at or near a trailing edge which can be deployed individually at various angles whenever required. They can be used for active pitch, roll, yaw and lift control in blended wings and rotor blades [12, 13].

Apart from the aerospace industry, Gurney flaps can be applied to wind turbines to increase the power output [14, 15]. A similar device as MiTEs called a microtab, as shown in, Figure 2.4 has gained increasing attention for active load control from gusts, turbulence, in a wind turbine blade as blades become longer and more flexible.



Figure 2.2: Gurney flap on the tail section of a Bell 222U(top),Apache(bottom) Helicopter, [11]



Figure 2.3: Wing with MiTEs [12]

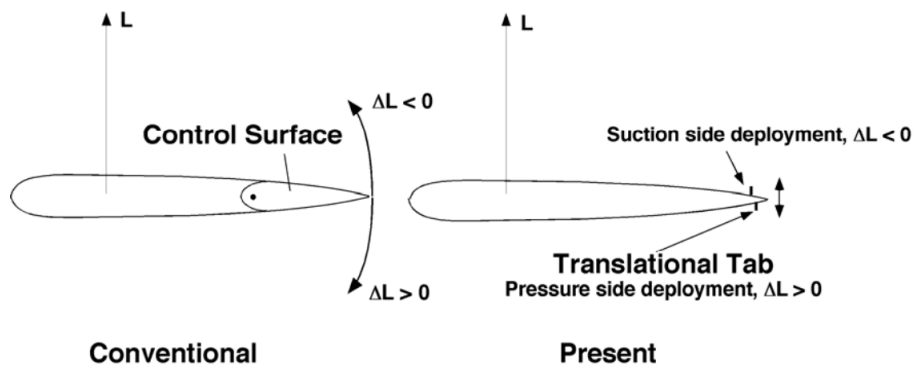


Figure 2.4: Microtab load control in a wind turbine blade [15]

A Gurney flap is a counter intuitive device for aerodynamicists, as it is essentially a flat plate perpendicular to the flow, and hence the drag penalty should be too high to have any applications in engineering. However, previous research on Gurney flaps has shown that under certain conditions a Gurney flap has potential applications and advantages. For example, Kentfield [16] installed Gurney flaps on helicopter rotors and achieved a lift increment of 10% without increasing engine power or rotor diameter. A brief history based on previous studies on advantages, disadvantage of a Gurney flap including the geometry and flow conditions are listed below:

Geometry and flow conditions:

- Gurney flap height within the local boundary layer thickness at the trailing edge. Various studies [17, 18, 19] indicate the drag increases substantially if the Gurney flap is not fully submerged in the boundary layer.
- Gurney flap most effective at the trailing edge. A study by Li *et al.* [18] indicates the reduction in $C_{l,max}$ to 13.6% from 17.4% of clean $C_{l,max}$ when the 1.5% c flap on NACA 0012 moves upstream by 6% c .
- Gurney flap mounting angle: 45°- 90°. Li *et al.* [20] showed that $C_{l,max}$ increased to 17.4% for the 90° flap as compared to 12.3% for the 45° flap.
- Boundary layer: Laminar/Turbulent for Gurney flaps. Maughmer *et al.* [21] performed wind tunnel studies for free and fixed transition cases on Gurney flaps and found that the drag penalty is more severe with increasing flap height when the flow is mostly laminar. In the case where the boundary layer is mostly turbulent, increasing height of flaps does not cause a large increase in drag.

Advantages:

- A substantial increase in lift coefficient, maximum lift coefficient in airfoils [18, 22, 23], high lift devices [24, 25], delta and double delta wings [26].
- Delay (more aft location of separation on the suction side) or elimination of flow separation due to the low pressure region in the wake caused by von Kármán vortex shedding [27].
- At higher lift coefficients, effect on lift-to-drag ratio is small, whereas lift coefficient is significantly increased [18].
- The increase in drag due to the Gurney flap to the total drag of an aircraft is relatively small. In particular for higher lift coefficients, when the comparison is made for the same lift coefficient, a wing with a Gurney flap will require a smaller angle of attack, hence lesser pressure drag than a clean wing [28].

A disadvantage as mentioned earlier, is the drag penalty associated with a Gurney flap.

2.1.1 Flow Structure

Mean flow field

Liebeck [29] first experimentally studied Gurney flap on a Newman airfoil which resulted in a higher lift coefficient for the 1.25% c flap. He found that maximum aerodynamic benefits could be achieved when flap height is within the boundary layer (1-2% c). Drag increased significantly for height more than 2% c . He suggested that the Gurney Flap altered the flow field near the trailing edge thereby altering Kutta condition and the resulting circulation. He proposed the existence of counter-rotating vortices in the downstream of the flap using tufted probe as depicted in Figure 2.5.

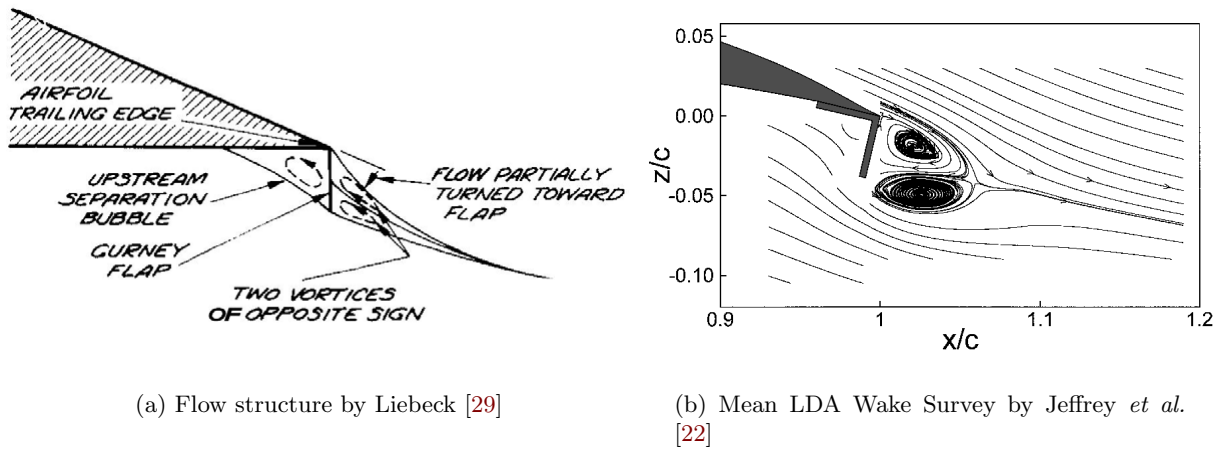


Figure 2.5: Flow structure in the vicinity of the Gurney flap

Flow visualization in a water tunnel study on NACA 0012 wing with different Gurney flaps by Neuhart *et al.* [30] showed Liebeck's proposed flow field was indeed correct. Jang *et al.* [23] performed RANS computations for a Gurney flap on a NACA 4412 airfoil. The time averaged RANS simulations showed a pair of counter rotating vortices downstream of the flap and a small recirculation zone upstream of the flap. Jeffrey *et al.* [22] performed laser doppler velocimetry (LDV) measurements on an e423 wing with 4% c Gurney flap (no forced transition of the boundary layer) and also showed the pair of counter rotating vortices. In addition, Jeffrey *et al.* showed the stagnation point was further downstream where the streamlines meet to form the wake.

Instantaneous flow field

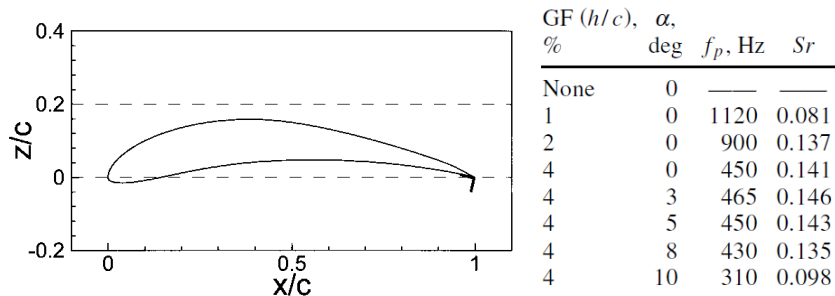
Smoke flow visualization and LDV measurements carried out by Jeffrey *et al.* in the wake of the Gurney flap gave evidence of alternate von Kármán vortex shedding as shown in Figure 2.6. Using spectral analysis they reported principal frequencies, Strouhal numbers ($St = f_p d / U$) of vortex shedding for different flap sizes and incidence as shown in Figure 2.7. An explanation for the dependence of frequencies with flap height and angle of incidence was given using Gerrard's [31] widely accepted postulate for the mechanism of formation of von Kármán vortex street for bluff bodies. A Gurney flap is similar to a cylinder in a flow, the boundary layers on the upper and lower surface separate to form two shear layers of opposite



Figure 2.6: Smoke flow visualization[22]

vorticity. One of these separating shear layer rolls up and forms a vortex. The other shear layer which consists of opposite vorticity cuts off the supply of vorticity in the first shear layer thereby shedding a vortex in the process. The separation point remains fixed on the pressure side due to the flap. The separation point on the suction side varies with angle of incidence and Reynolds number. The most important results obtained in the study were :

- Reducing the flap height from 4% to 2% increased the frequency (450 Hz to 1120 Hz) of shedding but decreased the Strouhal number (0.141 to 0.081). It was concluded that decreasing the distance between the two separating shear layers (by decreasing the flap height) decreased the time it takes for the second shear layer to interact and cut off the supply of vorticity to the first shear layer. This causes the frequency of shedding to increase.
- On the other hand, increasing incidence from 0° to 10° reduced both frequency (450 Hz to 310 Hz) and the Strouhal number (0.141 to 0.098). An explanation for the trend was that increasing incidence, increased the boundary layer thickness. A thicker boundary layer has a much weaker velocity gradient across it and consequently lower vorticity. This increased time for sufficient vorticity to cut off the shear layer, thereby reducing the frequency. Increasing $\alpha=8^\circ$ to 10° , caused an upward movement of separation point on the suction side which increased the vertical distance between the shear layers and hence reduced the shedding frequency further.



(a) Model Jeffery *et al.*

(b) Frequencies and Strouhal numbers

Figure 2.7: Strouhal frequency: LDV for e423 wing [22]

Troolin *et al.* [32] used the technique of Time Resolved-Particle Image Velocimetry (TR-PIV) on a NACA 0015 with different sizes of Gurney flaps (no forced transition of the boundary layer) and discovered two modes of shedding as shown in Figure 2.8. Spectral analysis on TR-PIV images showed the primary mode consisted of von Kármán vortex shedding and secondary mode was caused by fluid recirculating in the cavity upstream and subsequently ejecting downstream of the flap as shown in schematic Figure 2.8(a). Hot wire anemometry was carried out upstream of the Gurney flap which also indicated the presence of a second peak as shown in Figure 2.9.

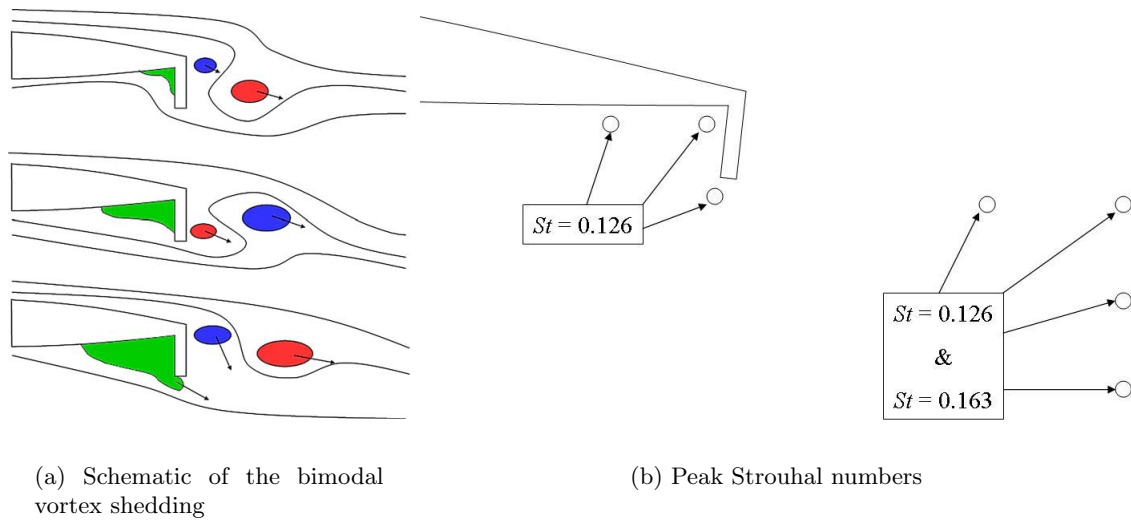


Figure 2.8: Bimodal vortex shedding [32]

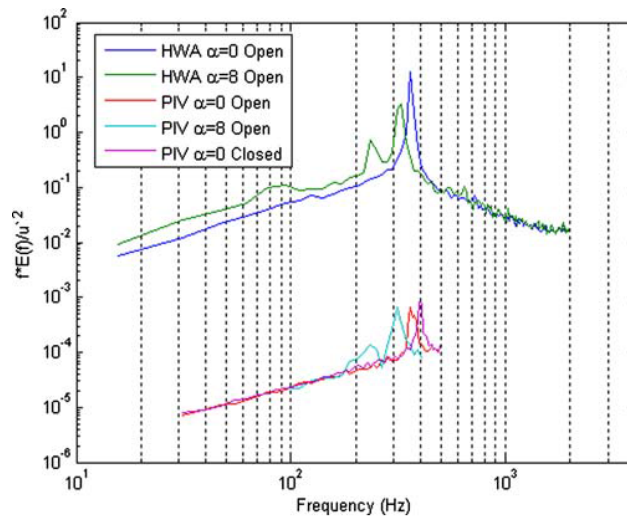


Figure 2.9: Spectral analysis PIV, Hot Wire [32]

The different frequencies, Strouhal number based on flap height ($St=fh/U$) for various flap sizes and angles of attack are shown in Figure 2.10. The main results based on the study were:

- The primary frequency of vortex shedding decreased with an increase in flap height and angle of attack.
- The secondary shedding frequency was lower than the primary von Kármán shedding and became more coherent as the angle of attack increased.
- The two modes interacted downstream of the flap constructively or destructively depending on their phase.
- Coherent structures scaled approximately with the height of the flap.
- Primary Strouhal number decreased with increase in angle of attack due to an increase in boundary layer thickness as was also proposed by Jeffrey *et al.*
- Decreasing flap height decreased the volume of trapped fluid in the recirculating region, thereby increased the frequency of the secondary mode.
- A ‘closed’ model of the Gurney flap showed no secondary shedding.

Re = 2.1×10^5							Re = 1.0×10^5						
Gurney Flap	Alpha (deg)	Primary Frequency (Hz)	Secondary Frequency (Hz)	Primary St# (1)	Secondary St# (2)	Ratio of St#(2) / St#(1)	Gurney Flap	Alpha (deg)	Primary Frequency (Hz)	Secondary Frequency (Hz)	Primary St# (1)	Secondary St# (2)	Ratio of St#(2) / St#(1)
4%	0	371		0.186			4%	0	176	154	0.186	0.163	0.88
	4	337		0.170				4		142		0.152	
	8	323	250	0.163	0.126	0.77		8	166	139	0.179	0.150	0.84
	12	323	239	0.164	0.121	0.74		12					
2%	0	626		0.168			2%	0	154		0.087		
	4	560	400	0.151	0.108	0.71		4	200		0.115		
	8	475	326	0.128	0.088	0.69		8	262		0.151		
	12	418	318	0.113	0.086	0.76		12					

(a) At Re: 2.1×10^5 (b) At Re: 1.0×10^5 **Figure 2.10:** Summary of primary and secondary Strouhal numbers [33]

2.1.2 Lift increment mechanisms

A review paper by Wang *et al.* [28] is a comprehensive summary of previous studies on Gurney flaps. The current understanding of different mechanisms by which a Gurney flap increases lift is also discussed in the paper. In their words:

“It is fair to say that the mechanisms responsible for the lift enhancement of the GF have not been fully understood. As a part of effort to shed some light on this issue, pressure and velocity measurements over the airfoil surface as well as PIV measurement and dye-injection visualization around the trailing edge of the airfoil have been carried out with and without the GF.”

Li *et al.* [18] obtained lift and drag coefficients for NACA 0012 with 0.5 to 3%*c* Gurney flaps. As compared to a clean airfoil, the maximum lift coefficient increased and stall angle decreased as shown in Figure 2.11. They observed that the Gurney flap on a NACA 0012 increased maximum lift coefficient due to an **increase in the effective camber of the airfoil**. The wake profile also shows a downward turning of the flow suggesting an increase in camber. Their results agree with Liebeck’s prediction of significant drag increase for flap height of more than 2%*c*. Liu *et al.* [34] showed the special camber effect of the Gurney flap using thin airfoil theory.

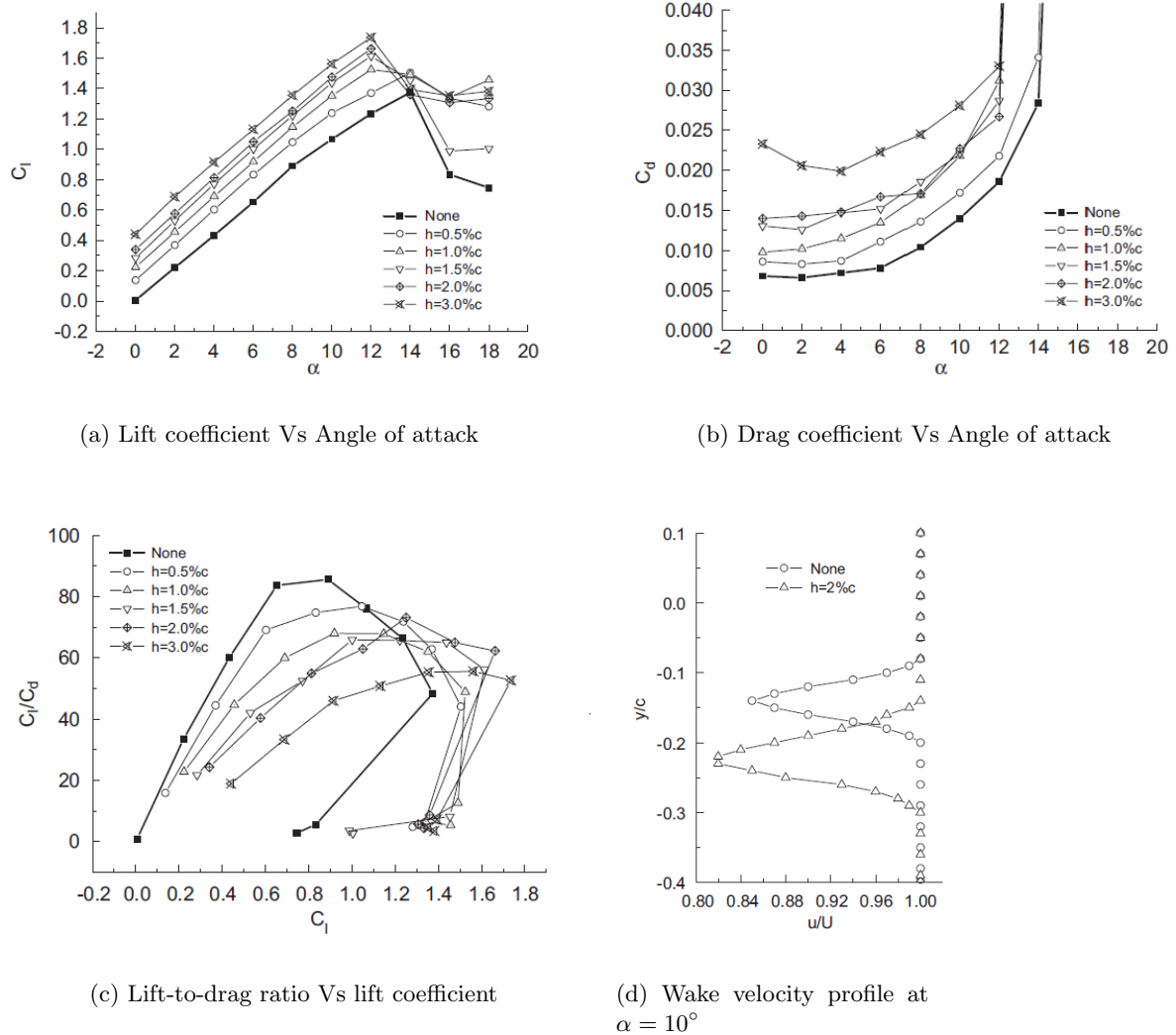


Figure 2.11: Lift, drag coefficients, L/D ratio and velocity profile [28]

Li *et al.* measured airfoil pressure distribution for the 2% c case using pressure taps. Pressure distribution obtained shows (Figure 2.12) an **increased suction on the upper surface and an increased pressure on the lower surface** as compared to the clean NACA 0012 airfoil. Jeffrey *et al.* suggest the increase in the overall loading in a Gurney flap is due to finite pressure difference that a Gurney flap introduces at the trailing edge. The von Kármán vortex shedding increases base suction at the trailing edge which is almost constant downstream of the flap. Jeffrey *et al.* also used panel method to show that a finite pressure difference at the trailing edge increases total circulation and therefore lift.

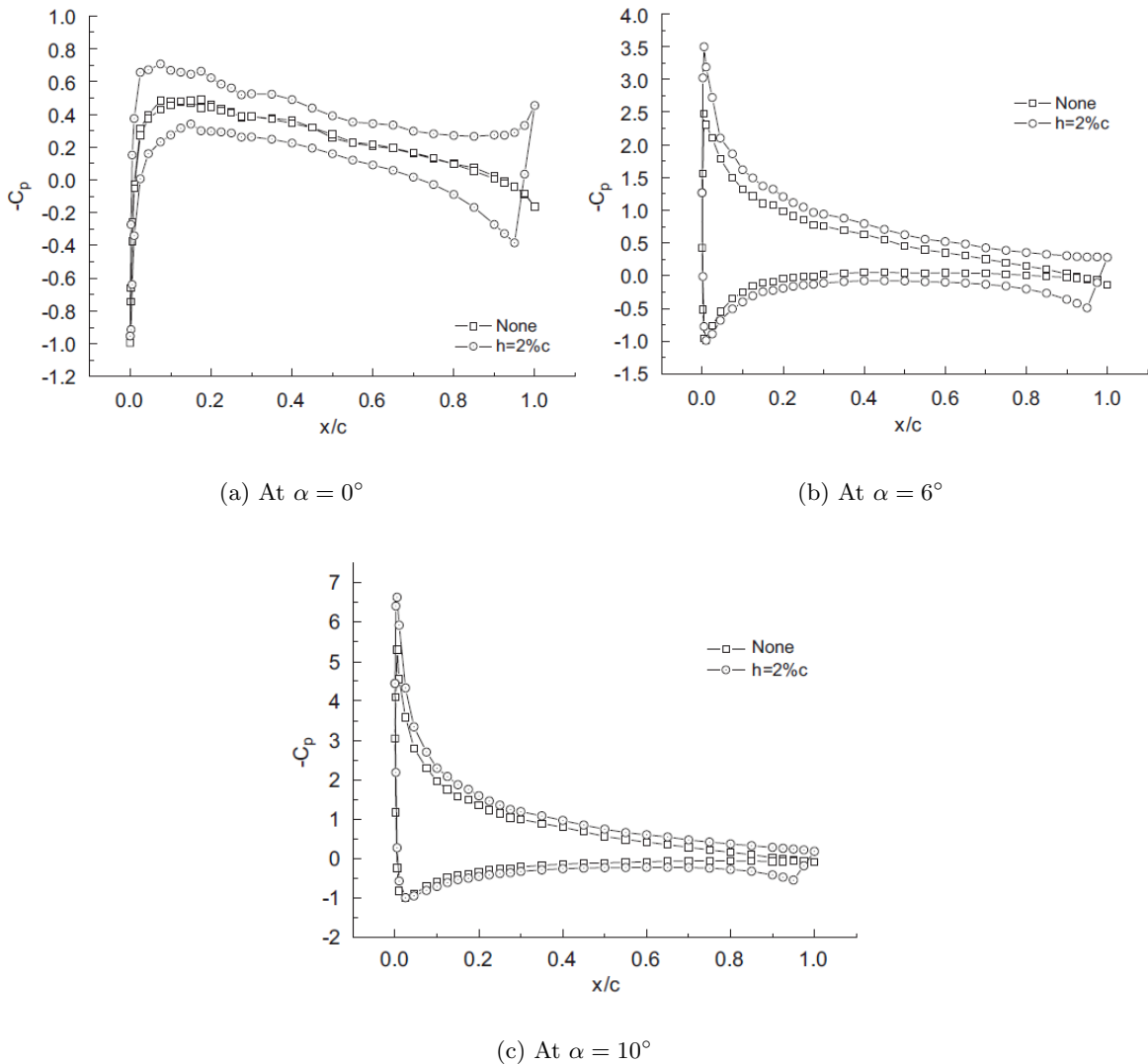


Figure 2.12: Pressure distributions over an airfoil with a Gurney flap [28]

Troolin *et al.* concluded that **the secondary mode of shedding** was responsible for the increased circulation which in turn was responsible for additional lift generated by the Gurney flap. Another explanation is due to the location of off-surface stagnation point caused by the vortex structure. This is equivalent to an airfoil with an **increase in chord** [28].

2.2 Aeroacoustics

Aeroacoustics is the study of sound generated aerodynamically by unsteady flows and/or fluctuating aerodynamic forces including the influence of any solid bodies in the flow. In an attempt to understand and predict the noise generated by a free jet, Sir James Lighthill [35] formulated an '*aeroacoustic analogy*' which gave a formal definition of an acoustic field in a flow. This laid the foundation for modern aeroacoustics. Several acoustic analogies have been formulated after Lighthill by Curle [36], Powell [37] and Ffowcs Williams [38]. Although these analogies are not directly used in the thesis, some important relations have been derived using them.

2.2.1 Properties of Sound

Sound is an isentropic pressure perturbation, p' , which propagates as a wave in a compressible medium at a speed given by:

$$\begin{aligned} c_0 &= \sqrt{\frac{\partial p}{\partial \rho}_{s=s_0}} \\ &= \sqrt{\gamma RT} \quad (\text{Ideal Gas}) \end{aligned} \quad (2.1)$$

where γ is the ratio of specific heat of an ideal gas (C_p/C_v), R is the gas constant and T is temperature in Kelvin. The speed of sound c_0 in standard air is 344 m/s (20°C)

Sound Pressure Level (SPL)

It is a logarithmic scale used to measure the effective sound pressure relative to a reference value (unit: decibels, dB). The logarithmic scale is used because of the large range of rms values perceived by the human ear. The reference value is set to the threshold of human hearing ($p_{\text{ref}}=2 \times 10^{-5} \text{Pa}$)

$$\text{SPL} = 20 \log_{10} \left(\frac{p_{\text{rms}}}{p_{\text{ref}}} \right) \quad (2.2)$$

It is important to note that these pressure perturbations are small (For 120dB, relative perturbations $p_{\text{rms}}/p_0 = 2 \times 10^{-4} \ll 1$, $p_0 = 1 \text{ atm} = 10^5 \text{ Pa}$) [39]. This is important in order to realize that:

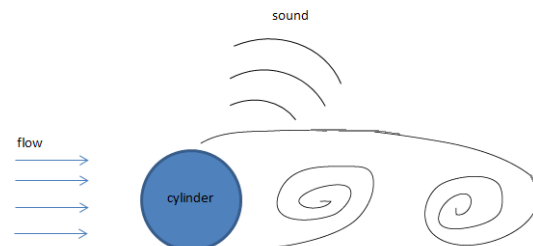
- In some cases, sound *propagation* can be studied by linearizing the Navier Stokes equations [39].
- Acoustic waves carry a tiny fraction of the total energy in the flow.

2.2.2 Mechanisms of noise generation

It is important to understand the mechanisms of flow induced noise generation in order to mitigate its production. The mechanisms of noise production depends on the associated flow field which in turn depends on flow parameters like Reynolds number, the type of boundary layer and the geometry of the object in the flow. Although a generalization cannot be made for all cases, three dominant mechanisms for flow induced noise generation in presence of solid bodies can be classified into:

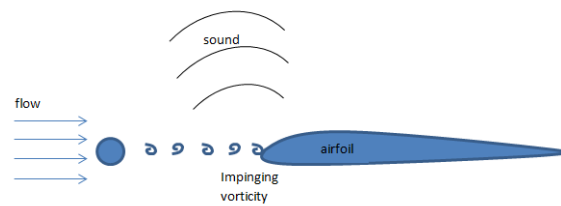
Vortex shedding noise:

Vorticity shed in a flow past a bluff body in the form of a von Kármán vortex street causes fluctuating pressure along the surface which radiates out as sound. The noise generated has a characteristic frequency (tonal).



Turbulence - Structure interaction:

Vortical structures shed by a bluff body present upstream radiates sound when they are impinged on a solid surface.



Trailing edge noise:

Vortical structures convecting in the turbulent boundary layer can cause similar pressure fluctuations on the surface radiating sound having a broadband character. Noise can also be generated due to the boundary layer instabilities which tend to have a tonal character.

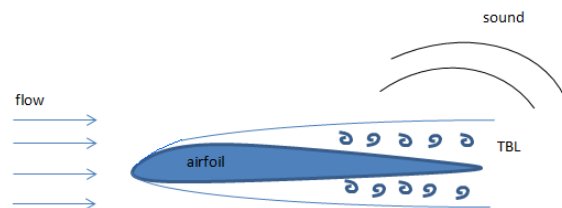


Figure 2.13: Different mechanisms of noise generation

In the case of a Gurney flap, the flow structure as discussed earlier suggests the vortex shedding noise and the trailing edge noise to be relevant mechanisms which need to be investigated. In general, the main aim of an aeroacoustic study is to:

- Understand the mechanisms of noise production.
- Identify the location and main sources of noise.
- Accurately compute far-field acoustic pressure fluctuations and directivity.

2.2.3 Approach

The challenge in investigating noise generating flows is that they are produced by non-linear, unsteady and turbulent interactions [40]. Moreover, for *low Mach* number flows (aircraft take off/landing conditions) that are considered in the thesis, there is a large scale separation between the fluid dynamic and acoustic disturbances. This imposes stringent requirements in accuracy while computing the flow field and the acoustic sources [41]. Flow induced noise can be studied using computational techniques or experimental methods (also analytically for few simple cases). The flow chart describes the broad categories in each.

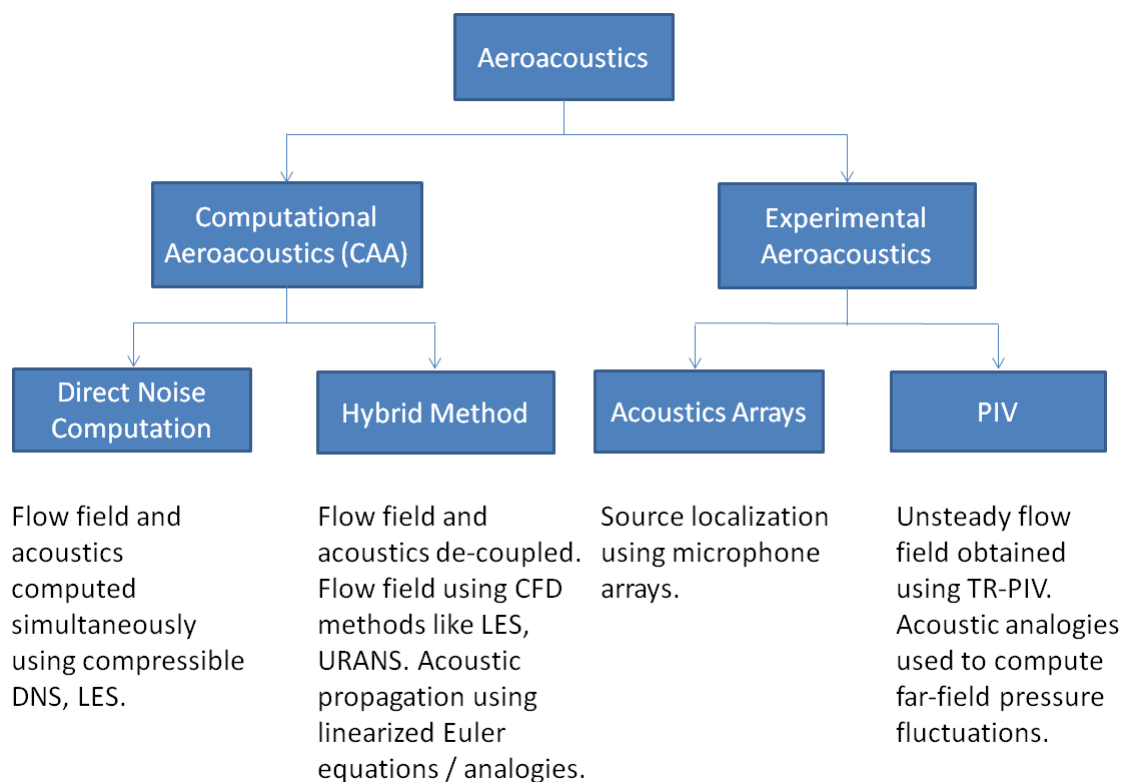


Figure 2.14: Aeroacoustics: Different approaches

Limitations of Computational Aeroacoustics:

- Direct Noise Computation (DNC):

High fidelity methods like compressible Direct Numerical Simulation (DNS) is restricted to low Reynolds number (~ 5000). DNS resolves all the scales by solving exact Navier-Stokes equations in a flow and hence requires high computational time and memory. These simulations are normally applied to simple geometries to be used as a benchmark for other methods rather than to solve a particular aeroacoustic problem. For example, the computational cost for a subsonic turbulent jet to resolve both the hydrodynamic and acoustic field is proportional to $Re^3 M^{-4}$ for DNS and $Re^2 M^{-4}$ for LES [40, 42]. In order to obtain good accuracy, these methods are feasible when applied to high subsonic

Mach numbers where compressible effects are dominant [42]. The flow field and noise radiation computed by Gloor [43] using DNC and LES for a heated coaxial jet flow at $M=0.88$, $Re=10^6$ is shown in the Figure 2.15,

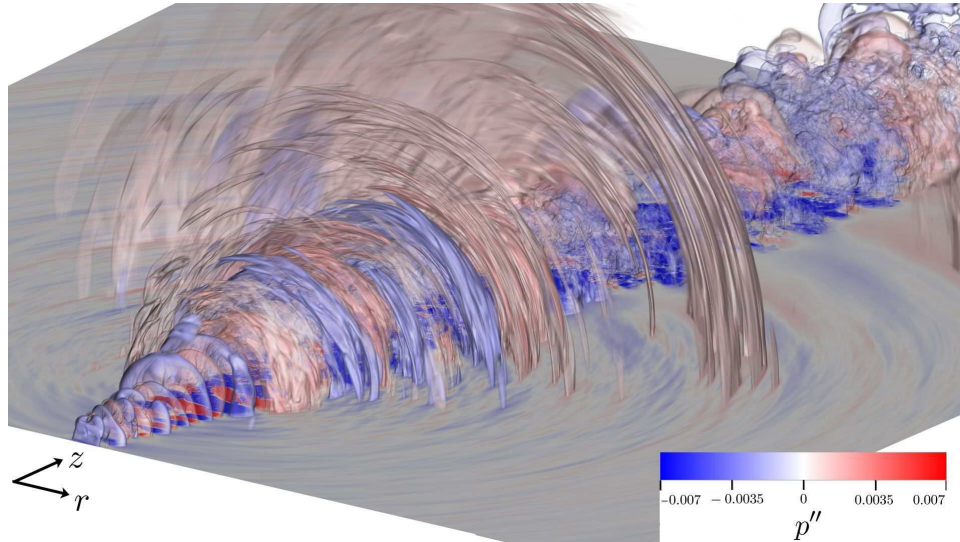


Figure 2.15: Instantaneous pressure perturbation for a heated coaxial jet [43]

- Hybrid Method:

Since the flow field and acoustics are decoupled, the numerical accuracy required for the computation of the acoustics in the hybrid method is less (only the source region has to be computed accurately). However, the required computational costs are still large when Linearized Euler equations are used for propagation of the acoustic far-field. Alternatively, the use of acoustic analogies to calculate the far-field acoustic field also leads to various uncertainties depending on the type of analogy, type of control surface/volume used [40, 43].

On the other hand, using experimental techniques can overcome the current limitations of computational power required for aeroacoustic applications which involve high Reynolds number (turbulent) and low Mach number flows. The state-of-the-art technique of Particle Image Velocimetry (PIV) is the flow measurement technique that is used in the thesis. It is explained in detail in the next chapter. The following section explains the relevant background in aeroacoustic analogies.

2.2.4 Aeroacoustic Analogies

Aeroacoustic analogies are formulated by rearranging the Navier-Stokes equations. They relate the wave like propagating pressure/density fluctuations to the hydrodynamic characteristics of the flow. The comprehensive article by Lele *et al.* [40] clearly explains the concept as follows:

Suppose \mathbf{q} is a state vector containing velocities and other thermodynamic variables satisfying compressible equations,

$$N(\mathbf{q}) = 0 \quad (2.3)$$

Rearranging the equation to,

$$L\mathbf{q} = S(\mathbf{q}) \quad (2.4)$$

forms an aeroacoustic analogy, where L is usually a linear wave operator $[\frac{1}{c_\infty^2} \frac{\partial^2}{\partial t^2} - \nabla^2]$ and S is the non-linear sound source. The part of the flow which produces the sound is called the source flow while the part in which a listener is typically present is called the reference flow. The difference between the source flow and the extrapolation of the reference flow into the source region is known as the ‘*source of sound*’. It is termed as an ‘analogy’ because $S(\mathbf{q})$ can also be assumed to act *analogously* as an externally applied source (forcing term) on a quiescent/reference flow. This formal definition of an acoustic field in a flow was presented by Lighthill in his landmark paper in 1952.

Lighthill’s Analogy

Lighthill transformed the Navier Stokes and continuity equations to form an exact, inhomogeneous wave equation as derived below,

Continuity equation:

$$\frac{\partial \rho}{\partial t} + \frac{\partial(\rho u_i)}{\partial x_i} = 0 \quad (2.5)$$

Momentum equation:

$$\frac{\partial(\rho u_i)}{\partial t} + \frac{\partial(\rho u_i u_j)}{\partial x_j} = -\frac{\partial p}{\partial x_i} + \frac{\partial \tau_{ij}}{\partial x_j} \quad (2.6)$$

where $\rho = \rho_0 + \rho'$, $p = p_0 + p'$, and p_0, ρ_0, c_0 are mean properties of fluid at rest.

By calculating $\frac{\partial}{\partial t}(1) - \frac{\partial}{\partial x_i}(2)$ and using $c_0^2 \nabla^2 \rho = c_0^2 \frac{\partial^2}{\partial x_i \partial x_j} (\rho \delta_{ij})$ the famous Lighthill’s equation is obtained,

$$\frac{\partial^2 \rho}{\partial t^2} - c_0^2 \nabla^2 \rho = \frac{\partial^2 T_{ij}}{\partial x_i \partial x_j} \quad (2.7)$$

where T_{ij} is the Lighthill’s stress tensor given by (δ_{ij} is *Kronecker delta*),

$$T_{ij} = \rho u_i u_j + (p - c_0^2 \rho) \delta_{ij} - \tau_{ij} \quad (2.8)$$

The above equation can be rewritten for an ideal, stationary acoustic medium subject to an externally applied stress T_{ij} . This is formally known as ‘Lighthill’s analogy’ which asserts that sound generated by turbulence in a real *unbounded* fluid is exactly equivalent to that produced in an ideal, stationary acoustic medium forced by stress distribution T_{ij} . In the definition of the Lighthill stress tensor T_{ij} ,

- The first term $\rho u_i u_j$ is called the Reynolds stress which is important when turbulent flows are considered.
- The second term $(p - c_\infty^2 \rho) \delta_{ij}$ is the excess of momentum transfer by the pressure (compared to that in an ideal fluid). It can be ignored for isothermal, incompressible flows as it is mainly produced by mean density variations in the source flow [39].
- The third term τ_{ij} is the viscous stress tensor whose contribution can be neglected for high Reynolds number flows.

Since *low* Mach (incompressible) and *high* Reynolds number flows are considered in the thesis,

$$T_{ij} \approx \rho u_i u_j \approx \rho_0 u_i u_j, \quad (2.9)$$

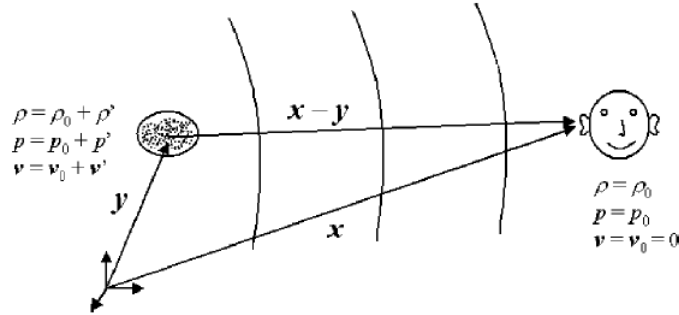


Figure 2.16: Source and Listener location in Lighthill's analogy [44]

The solution to Equation 3.7 is given by [39],

$$p'(x, t) = \frac{x_i x_j}{4\pi c_0^2 |\mathbf{x}|^3} \frac{\partial^2}{\partial t^2} \int_V \rho_0 u_i u_j \left(\mathbf{y} - \frac{|\mathbf{x}|}{c_0} \right) d^3 \mathbf{y} \quad (2.10)$$

where \mathbf{x} : position in far-field ($\mathbf{x} \gg \mathbf{y}$), \mathbf{y} : position in source region as shown in Figure 2.16.

It is important to realize from Lighthill's equation that:

- Equation 2.7 is exact as it is derived from the Navier Stokes equations.
- The free field turbulent source has 'quadrupole' type characteristic which is a weaker sound source than a 'dipole' or a 'monopole'. This implies that a tiny fraction of flow energy is converted to noise in low Mach number flows.
- Order of magnitude analysis for the quadrupole term shows: $p' \sim \frac{\ell}{|\mathbf{x}|} \rho_0 U^2 M^2$, acoustic power $\sim \ell^2 \rho_0 U^3 M^5$ for an eddy. This is also known as Lighthill's eighth power law.
- Influence of acoustics on the flow is not considered (acoustic feedback). This assumption is however valid in the present case of incompressible flow past a Gurney flap.

- It does not take into account the effect of any solid surfaces/moving boundaries present in the flow. The theory applies to an ‘unbounded’ fluid such as a free jet (without the presence of nozzle). Hence, it cannot be directly applied in the investigation of noise sources in a Gurney flap.

Curle’s analogy

Curle [36] extended the work of Lighthill by including the effect of a solid body in an unsteady flow. The presence of a solid body can influence the radiated sound field by refraction/diffraction of sound waves at the surface of the body and/or by generating a ‘dipole’ source at the surface. In order to arrive at a simplified expression of Curle’s analogy valid for the Gurney flap case, the concepts of acoustic far field and compact source are introduced.

Acoustic far field:

The condition of acoustic far field is met when the acoustic wavelength is much smaller compared with the distance d to the closest point in the source region ($d/\lambda \gg 1$ or $d/\ell \gg M^{-1}$). For a Gurney flap, the frequencies are of order 450 Hz as seen previously, $\lambda \approx 0.7m$ (in air), hence in order to achieve far field $d \gg 0.7m$.

Compact body:

The condition of acoustically compact source is met when the characteristic source length scale (Gurney flap length or size of large eddies) is much smaller compared to the wavelength of radiated sound ($\ell/\lambda \ll 1, L_s/\lambda \ll 1$) [40]. Thus the source behaves as a ‘point source’ as the difference in times for sound signals emitted from various source locations to arrive at a single point in the far field can be neglected. As $\lambda \propto cl/U \Rightarrow \ell/\lambda \propto M \ll 1$, low Mach number flows are acoustically compact and hence in the present investigation, the *compact body* assumption is valid.

Using the above far field and compact body assumptions, the simplified formulation of Curle’s equation can be obtained for incompressible, high Reynolds number flows in which the integration surface coincides with the physical body (to drop the normal and surface components of velocities at the surface)[39]:

$$p'(\mathbf{x}, t) = \frac{x_i x_j}{4\pi c_0^2 |\mathbf{x}|^2} \frac{\partial^2}{\partial t^2} \int_{V_y} \rho_0 u_i u_j \Big|_{t=t_e} dV - \frac{x_j}{4\pi c_0 |\mathbf{x}|^3} \frac{\partial}{\partial t} \int_{\partial V_y} P_{ij} \Big|_{t=t_e} n_i dS \quad (2.11)$$

where $P_{ij} = (p - p_0)\delta_{ij} - \tau_{ij} \approx (p - p_0)\delta_{ij}$

- The volumetric term is the ‘quadrupole’ contribution to the noise by the flow (same as

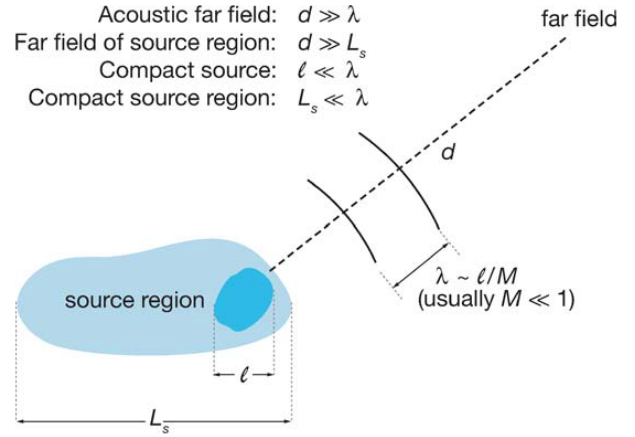


Figure 2.17: Source and sound scales [41]

in Lighthill's equation).

- The surface term is the 'dipole' term caused by unsteady pressure fluctuations on the surface of the body. Order of the magnitude analysis shows: acoustic power $\sim l^2 \rho_0 U^3 M^3$.

The order of the dipole term exceeds the quadrupole term by a factor of $\frac{1}{M^2} \gg 1$, hence the contribution of the quadrupole term can be neglected for low Mach number flows. The far field pressure fluctuations is given by [39],

$$p' = p_d \approx \frac{x_i}{4\pi c_0 |\mathbf{x}|^2} \frac{\partial}{\partial t} \int_S (p - p_0) \left(\mathbf{y}, t - \frac{|\mathbf{x}|}{c_0} \right) dS_i = \frac{x_i}{4\pi c_0 |\mathbf{x}|^2} \frac{dF_i}{dt} \left(t - \frac{|\mathbf{x}|}{c_0} \right) \quad (2.12)$$

where $F(t)$ is the unsteady lift force and p_d is the dipole sound pressure (Gutin's principle).

From Equation 2.12 it can be seen that there exists a *correlation* between the far-field pressure fluctuations to the unsteady lift (also termed as a Lift dipole).

Vortex sound theory

Powell [37], Howe [39] developed the important concept of vortex sound. They reformulated Lighthill's equation to emphasize the role of vorticity in the production of sound. For example, the mechanism of boundary layer separation and vortex release that takes place on the vocal chords is responsible for speech. This is especially important when considering homentropic low Mach number flows as vorticity $\boldsymbol{\omega} = \nabla \times \mathbf{v}$ is a convenient quantity to describe them. The vortex sound theory reduces the source term only to the region where vorticity is not negligible which is typically smaller than the source region described in Lighthill.

Using the incompressible equations,

$$\nabla \cdot \mathbf{v} = 0 \quad (2.13)$$

And the identity,

$$\nabla \cdot \nabla \cdot (\mathbf{v}\mathbf{v}) = \nabla \cdot (\boldsymbol{\omega} \times \mathbf{v}) + \nabla^2 \left(\frac{\mathbf{v}^2}{2} \right) \quad (2.14)$$

where $\mathbf{L} = \boldsymbol{\omega} \times \mathbf{v}$ is called the Lamb vector.

Powell's approximate equation of vortex sound theory for non-vibrating bodies, high Reynolds number (viscous effects negligible) and low Mach number flows (by neglecting the terms of the order of \mathbf{v}^2 in Equation 2.14) can be derived,

$$\frac{\partial^2 \rho}{\partial t^2} - c_0^2 \nabla^2 \rho \simeq \rho_0 \nabla \cdot (\boldsymbol{\omega} \times \mathbf{v}) \quad (2.15)$$

which shows the Powell-Howe source term $\rho_0 \nabla \cdot (\boldsymbol{\omega} \times \mathbf{v})$. Crowe showed that the principal source of sound at low Mach numbers is the divergence of Lamb vector [45]. The formal solution for Equation 2.15 using Green's functions can be written as,

$$p'(x, t) = -\rho_0 \int \int_V (\boldsymbol{\omega} \times \mathbf{v})_i \frac{\partial G}{\partial y_i} d^3 \mathbf{y} d\tau \quad (2.16)$$

This shows the important *correlation* between the far-field pressure fluctuations p' and the corresponding Lamb vector ($\boldsymbol{\omega} \times \mathbf{v}$). This equation forms the basis of the methodology used in the thesis to understand Gurney flap noise.

2.3 Research Objectives

The scope of the thesis is to perform a qualitative and quantitative description of the flow field and noise sources associated with a Gurney flap using high speed Particle Image Velocimetry as the diagnostic tool.

The main objectives are two-fold:

- Characterise the unsteady flow field associated with a Gurney flap using TR-PIV.
- Understand the mechanism of noise generation by identifying the structures that are highly correlated with far field pressure fluctuations.

Chapter 3

Experimental Techniques and their application in Aeroacoustics

An experiment is a question which science poses to Nature, and a measurement is the recording of Nature's answer.

Max Planck

Particle Image Velocimetry (PIV) has emerged to be a versatile flow visualization and quantification technique developed in the last few decades. This chapter briefly describes the basics of PIV, acoustic measurements and also discusses the use of PIV as a powerful diagnostic tool for aeroacoustics.

3.1 Flow Measurement: Particle Image Velocimetry

PIV is a non-intrusive measurement technique that allows measuring the instantaneous velocity field of the flow in a plane (planar PIV:2D-2C, stereoscopic PIV:2D-3C) or a volume (tomographic PIV:3D-3C). An overview of the development of the technique and its significance in fluid mechanics research is given by Raffel *et al.* [46], Westerweel and Adrian [47].

3.1.1 Working Principle

The flow is seeded with small tracer particles that accurately follow the fluid motion without altering its properties or flow characteristics. Fluid velocity can thus be quantified using Equation 3.1 by measuring the displacement of these small (μm) tracer particles within a very short time interval (μs). This is possible by illuminating the tracer particles *twice*

with a pulsed light source (typically a laser) and recording the light scattered by them onto subsequent image frames by a camera as shown in Figure 3.1.

$$\mathbf{V}(x, y, t) = \frac{\mathbf{x}_2(x, y, t + \Delta t) - \mathbf{x}_1(x, y, t)}{\Delta t} + \mathcal{O}(\Delta t^2) \quad (3.1)$$

where, V is the tracer particle velocity/flow velocity; \mathbf{x}_1 and \mathbf{x}_2 are the position vectors of a particle at t , $t+\Delta t$ respectively. A high spatial resolution is achieved by using a high seeding density (1-100 particles/mm³). Instead of tracking individual particles, the motion of an ensemble of particle images is evaluated via the statistical operation of *cross correlation*.

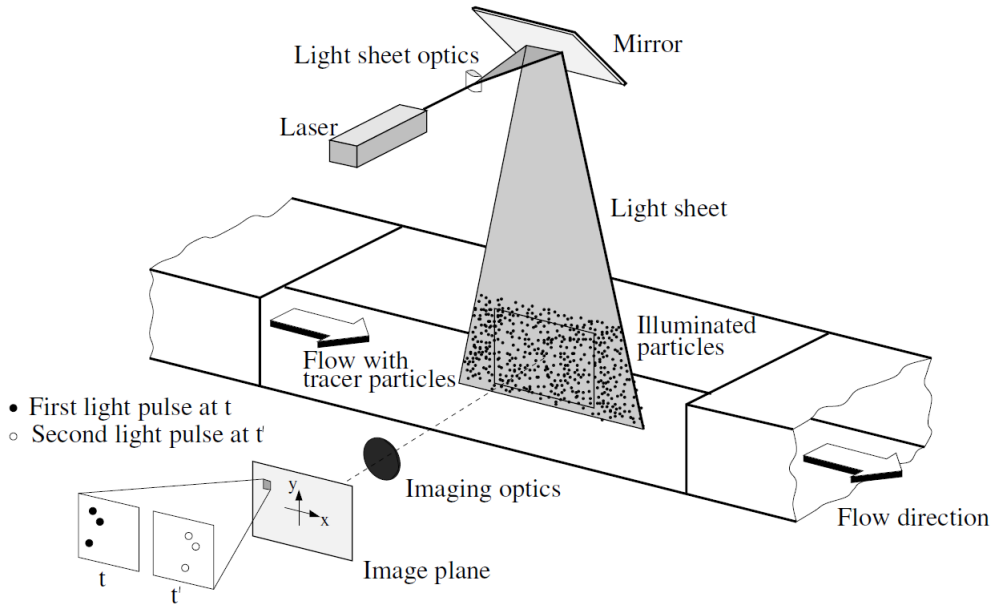


Figure 3.1: A typical PIV experimental set up and its working principle [46]

The main advantages of PIV are that it is *non-intrusive* (no probe inserted in the flow) and can obtain the velocity field on a *whole field* as compared to hot wire anemometry (HWA) and Laser doppler anemometry (LDA). However, potential disadvantages of PIV are that it is fairly complex to set up and requires optical access.

The following section describes the important factors that influence the results obtained from PIV [48].

3.1.2 Tracer fidelity

As discussed above, PIV quantifies the flow velocity indirectly by measuring the particle velocity. Therefore, the dynamics of tracer particles in the flow needs to be examined to avoid significant discrepancies between the fluid and particle motion.

- The slip velocity ($\mathbf{V}_p - \mathbf{V}_f$) of a particle in a viscous fluid at very low Reynolds number is given by Equation 3.2. The Stokes drag dominates the particle dynamics for very small particle tracers. In order to be able to faithfully follow the flow, the particle response time τ_p for a step variation given by Equation 3.3 is critical.

$$\mathbf{V}_p - \mathbf{V}_f = d_p^2 \frac{(\rho_p - \rho_f)}{18\mu} a \quad (3.2)$$

$$\tau_p = d_p^2 \frac{\rho_p}{18\mu} \quad (3.3)$$

Thus, smaller particles have lower response time and hence ensure good tracking of fluid motion. For turbulent flows, τ_p should be less than the time scale τ_f of the eddies to be resolved. The particle Stokes number (S_k) = $\frac{\tau_p}{\tau_f} < 0.1$ to obtain errors below 1%, where τ_f is the flow characteristic time.

- To achieve accurate measurement in the entire domain the seeding density should be homogeneous and typically about 10 particles/mm³.
- Light scattering directivity pattern for the particles is also an important consideration. The intensity of light scattered by particles is more in forward scatter as shown in Figure 3.2. Due to set up restrictions, most PIV applications have cameras placed in the side scatter (perpendicular for Planar). Particles should scatter enough light to be visible, and as expected larger particles scatter more light. A compromise between the maximum size of particles that follow the flow faithfully and the amount of light scattered has to be made.

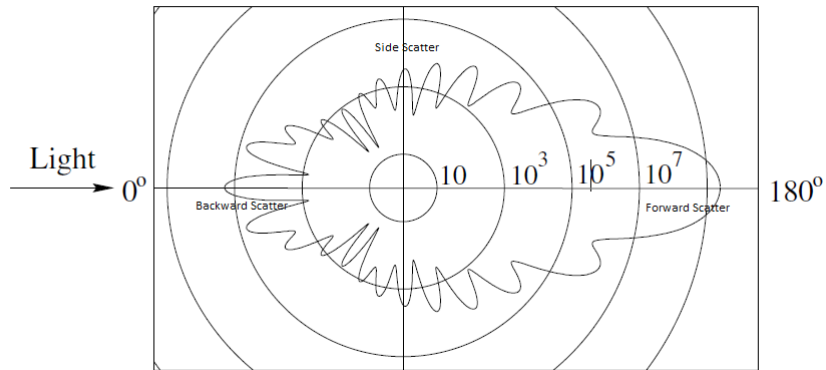


Figure 3.2: Intensity of scattered light ($1\mu\text{m}$ particle) [46]

3.1.3 Illumination

In most PIV applications laser light is used because it is monochromatic, collimated, coherent and can be easily shaped into a laser sheet by using lenses. The dual head Nd-YAG (for low

frequency acquisition, $\lambda=532\text{nm}$) and Nd-YLF (for high frequency acquisition, $\lambda=526\text{nm}$) are commonly used lasers. The monochromatic light emitted by lasers contain high energy density ($10\text{mJ} - 1\text{J}$, pulse duration δt : 5ns–10ns) and can be bundled into a thin laser sheet ($\Delta Z \approx 1\text{mm}$). The particles are illuminated twice by laser pulses emitted by two lasers firing independently with Δt as the separation time.

- The pulse duration δt should be such that the particles appear as circular dots and not as streaks. The condition to be satisfied is $\delta t < \frac{d_\tau}{VM}$, where d_τ is the particle image diameter, V is the velocity of the flow, M is the magnification factor
- For planar PIV, the laser sheet is kept perpendicular to the line of sight of the camera and its thickness is kept small to minimize errors due to averaging effects in the depth direction.
- Sufficient overlap between the two laser pulses is an important parameter to evaluate accurate particle displacement in the images.

3.1.4 Particle Imaging

The optical configuration is shown in Figure 3.3. An image of the illuminated particles in the laser sheet is formed using a digital camera.

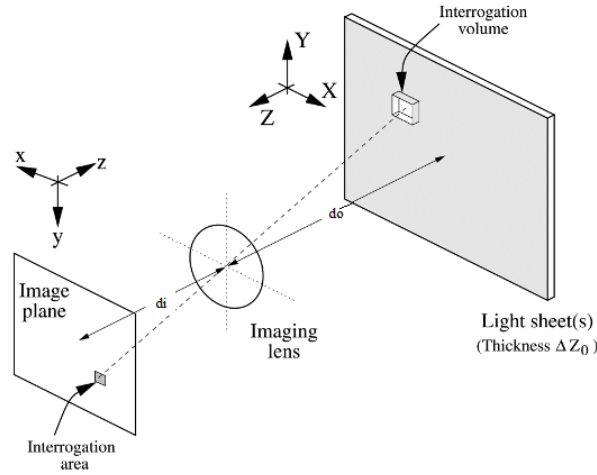


Figure 3.3: Particle imaging optics (modified from Raffel *et al.* [46])

The important parameters to consider are focal length f , f-stop ($f_\# = \frac{f}{D}$, D is the aperture diameter), and magnification factor ($M = \frac{d_i}{d_o}$, ratio of image distance d_i to object distance d_o). The thin lens approximation for optics is given by,

$$\frac{1}{f} = \frac{1}{d_i} + \frac{1}{d_o} \quad (3.4)$$

The particle image diameter according to geometric optics is,

$$d_{geom} = d_p M \quad (3.5)$$

The particle image diameter due to diffraction is estimated by,

$$d_{diff} = 2.44\lambda(1 + M)f_{\#} \quad (3.6)$$

The resulting particle image diameter is given by the Euclidean sum of the above terms,

$$d_{\tau} = \sqrt{d_{geom}^2 + d_{diff}^2} \quad (3.7)$$

In PIV, the diffraction limit d_{diff} generally dominates the geometric image diameter (d_{geom}) i.e. the resulting particle image diameter $d_{\tau} \approx d_{diff}$. It is important to keep d_{τ} to be 2–2.5 pixels (1 pixel size: $10\mu\text{m}$) so that the particle position can be detected with subpixel accuracy, avoiding *peak/pixel locking* (Westerweel [49]).

The focal depth of the camera δz given by Equation 3.8 shows the range in which the particles are in focus. It is important to keep the focal depth (δz) larger than the laser sheet thickness (ΔZ).

$$\delta z = 4.88\lambda f_{\#}^2 \left(\frac{M + 1}{M} \right)^2 \quad (3.8)$$

A higher $f_{\#}$ is necessary to have $\delta z > \Delta Z$ but leads to darker images due to a smaller aperture. Hence, an optimum $f_{\#}$ has to be selected based on d_{τ} , δz and brightness of the image.

3.1.5 Evaluation of particle image motion

The analysis (shown in Figure 3.4) of the acquired digital images to evaluate the motion of the particles is as follows,

- Image windowing:

The acquired image containing two frames is divided into small windows having significant number of particle tracers (at least 10). The local velocity vector is evaluated at each of these windows. Typical interrogation window sizes range from 16×16 pixels to 512×512 pixels. In order to optimize the window size, the maximum particle displacement should be smaller than $1/4$ of the window size and the in-plane variation of particle image displacements in the window should not exceed the particle image diameter.

- Cross correlation analysis:

The interrogation windows extracted from the two frames are statistically evaluated using the discrete cross correlation function as given by,

$$\phi(m, n) = \frac{\sum_{i=1}^I \sum_{j=1}^J I_A(i, j) \cdot I_B(i + m, j + n)}{\sqrt{\sum_{i=1}^I \sum_{j=1}^J I_A^2(i, j) \cdot \sum_{i=1}^I \sum_{j=1}^J I_B^2(i, j)}} \quad (3.9)$$

The peak position of $\phi(m, n)$ relative to origin indicates the average particle image displacement in that window.

- Correlation peak sub-pixel interpolation:
The particle image displacement is necessarily not an integer number of pixels obtained from the discrete cross correlation function, therefore the correlation peak is interpolated around the maximum to obtain sub-pixel precision displacement. This is typically done via a 3-point Gaussian fit [49].
- Divide by time and scaling:
The pixel shift obtained above is converted to velocity by dividing the time separation between the laser pulses, magnification factor and by multiplying with the pixel size.

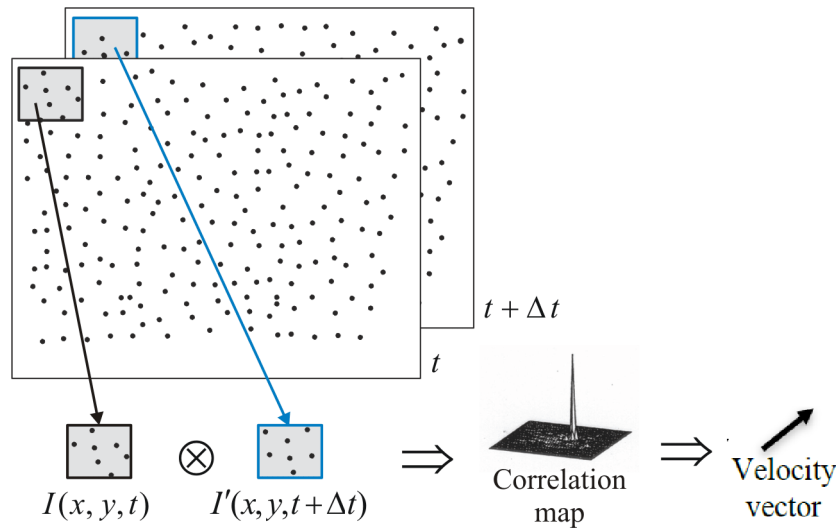


Figure 3.4: Particle image evaluation [48]

Currently, advanced techniques are available for pre-processing of images to remove reflections like image normalization, time minimum intensity subtraction and for more accurate processing/post-processing like iterative multi-grid, universal outlier detection etc. A detailed explanation is given in the PIV book authored by Raffel *et al.* [46].

3.1.6 Stereo - PIV

Unlike planar (2D) PIV described above, stereo-PIV is a 3C-2D PIV that also captures the out-of-plane component of the velocity field. Stereo PIV uses two cameras placed at different angles (60° - 90° between them) with respect to the planar light sheet as shown in Figure 3.5 (Prasad, [50]). Using two cameras helps in correcting perspective effects which can be a problem with one camera (planar PIV).

3.1.7 Time Resolved - PIV

The rapid advancement in high-speed lasers (Nd:YLF) and high-speed cameras based on CMOS sensor technology (that can acquire images at acquisition frequencies as high as 10kHz)

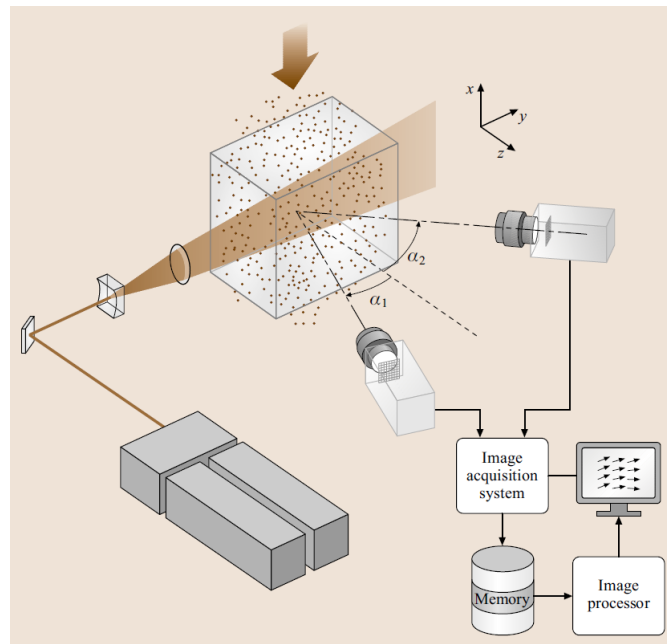


Figure 3.5: Typical setup of Stereo-PIV reproduced from Tropea *et al.*

has made it possible to capture the unsteady flow field of turbulent flows with high temporal and spatial resolution. Since aerodynamic noise is intrinsically associated with unsteady flows, the quantification of the time evolution of such a flow field is critical. Hence, TR-PIV has become a powerful and indispensable tool that is employed in the thesis to help in our understanding of Gurney flap aeroacoustics.

3.2 Acoustic Measurement: Microphones

Microphones are commonly used in everyday devices. They convert acoustic energy into electrical energy. The most common type are condenser microphones which use a capacitor as shown in Figure 3.6. The front plate acts as a diaphragm that vibrates due to sound waves thereby changing the distance between the plates and its capacitance. This causes a variation in voltage which is measured and can be converted in terms of pressure fluctuations by calibration.

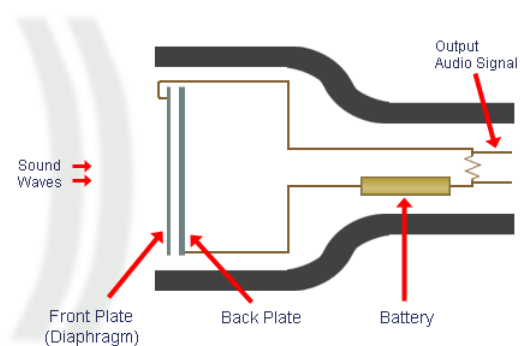


Figure 3.6: Condenser Microphone

3.2.1 Acoustic source localization

An array of microphones can be used to map the location of the main sources of noise. This can be done using beam forming algorithms [2]. The principle of beamforming is shown in Figure 3.8. The signal recorded by the microphones is time shifted (or phase shifted in frequency domain) and the unknown source location is moved all over the scan plane. When the position in the scan plane coincides with the actual source location the phase shift between the microphones is zero and corresponding output for the source strength is high. Otherwise the output is low because of random phase shift in the microphone signals. These algorithms can also be used to locate the source on moving objects like aircraft landing/take off, wind turbine blades (Figure 3.7) [2].

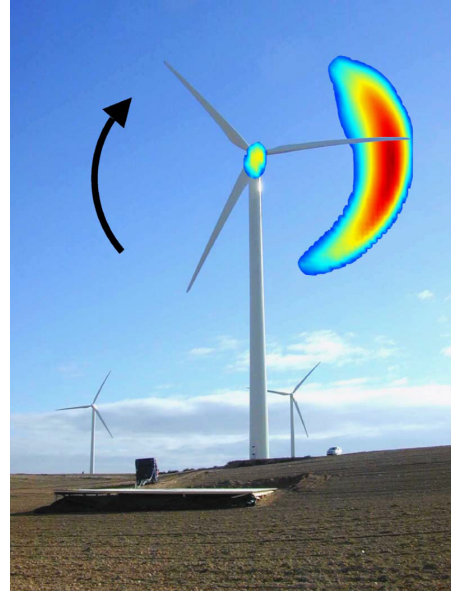


Figure 3.7: Wind turbine noise source [2]

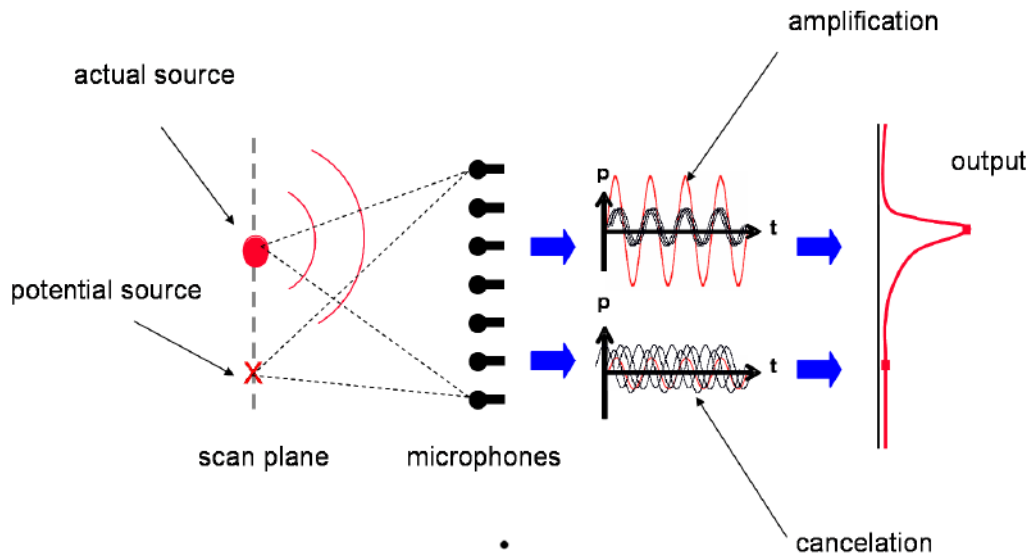


Figure 3.8: Principle of Array beamforming [51]

3.2.2 Array Resolution

Array resolution is an important criteria to be able to map the acoustics sources on the model with sufficient detail. It is defined as the width of the 'main lobe' (dark red region in Figure 3.7) 3dB below its peak. It depends on the frequency, size of the array, individual

microphone locations, distance from the source and the beamforming algorithm. A rule of thumb for the size of the main lobe is given by [52],

$$\Delta_{3dB} = \frac{425Y}{Df} \tag{3.10}$$

where D is the diameter of the array ($\approx 1m$), Y is the distance between the source and the array, f is the frequency of the source of noise. For better spatial resolution higher frequencies and larger array sizes are needed. In the Gurney flap case the noise source frequencies are low (250-450Hz) which makes $\Delta_{3dB} \approx Y$, and due to the model size (20cm), the acoustic array and the model needs to be too close to obtain the acoustic source locations using array beamforming. Hence, microphone array measurements are not carried out in the thesis.

3.3 PIV and Aeroacoustics

The application of PIV in aeroacoustics helps in establishing a direct connection between the acoustic pressure fluctuations and the flow dynamics at the origin of noise generation [53]. This is similar to the technique used in the direct noise computation method in which the acoustic source term is computed by solving full unsteady Navier Stokes equations as described in section. The main advantage of PIV, however, is that it can be used to study an aeroacoustic problem at high Reynolds number flows. In addition, TR-PIV as explained earlier helps in describing the unsteady flow phenomena responsible for noise generation in great detail.

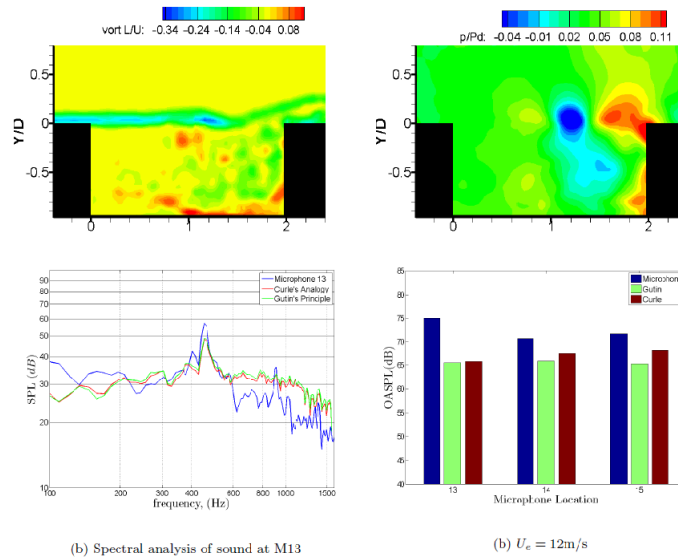


Figure 3.9: Aeroacoustics of cavity using TR-PIV [54]

A first and a more common approach is the combination of near-field data measured using PIV and the corresponding acoustic far-field computed using acoustic analogies. PIV is used

to measure the velocity fluctuations in the source region. Using these velocity fluctuations in the momentum equations, the hydrodynamic pressure fluctuations are derived and serve as an input in various acoustic analogies. The analogies are then used to predict far-field acoustic pressure fluctuations. Parkhi [54] used this approach for acoustic tones produced due to flow past an open cavity. Acoustic feedback loop was identified as the dominant mechanism. The location of the tonal peaks was captured well using Curle's analogy, however the sound pressure level was underestimated. This was attributed to the errors associated with computing the hydrodynamic pressure fluctuations from the velocity data obtained from TR-PIV. Other studies using TR-PIV on cavity aeroacoustics include Koschatzky [55], Haigermoser [56].

It was also applied to the case of an incompressible circular and chevron jet noise by Violato *et al.* [57]. Time resolved tomographic PIV (4D) was used to explore the relation between coherent structures and acoustic source (second temporal derivative of the Lamb vector) and predict far-field acoustic fluctuations, all based on Powell's analogy (no pressure reconstruction required). In case of circular jet, coherent axisymmetric flow structures are observed and the acoustic source activity is highest in case of vortex pairing and vortex ring disruption. These coherent flow structures are absent in the case of a chevron nozzle wherein the acoustic source is highest in the formation of C shaped structures and during the decay of streamwise instabilities. The study showed that the average of second derivative of Lamb vector shows a gradual increase in the axial direction for the circular nozzle but has a peak at $Z=2.8$ for the chevron nozzle as shown in Figure 3.11. In this study, however, it is important to point out the use of 4D PIV for aeroacoustics remains to be a challenging task due to the limited measurement domain, typically 50cm^3 (Scarano [58]).

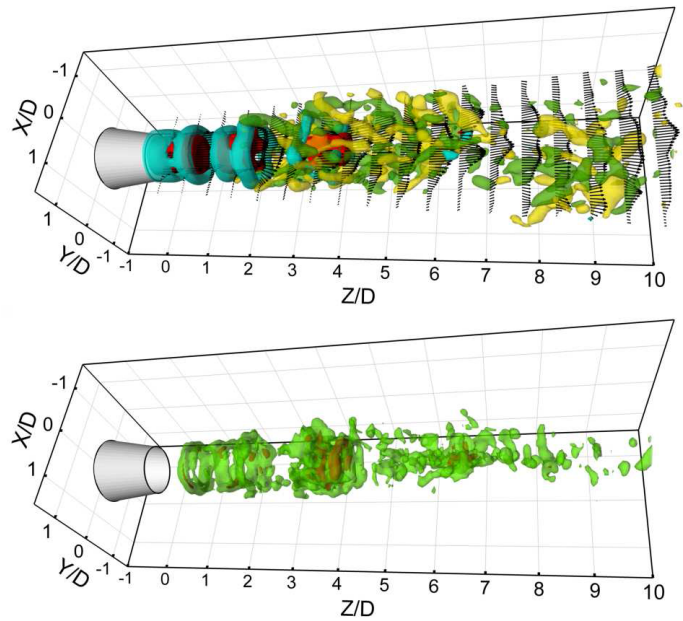


Figure 3.10: Jet aeroacoustics using 4D PIV [57]

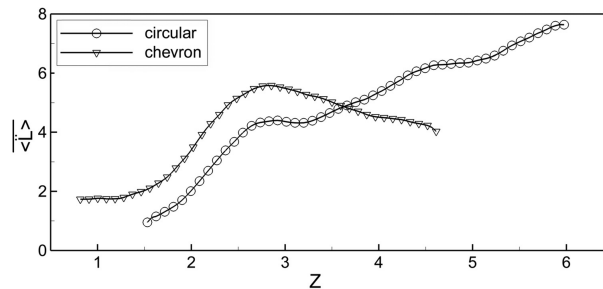


Figure 3.11: Second temporal derivative of Lamb Vector spatial distribution along jet axis [57]

For the case in which sound is produced by the flow interacting with an immersed body, Lorenzoni *et al.* [59] used TR-PIV to extract the body-surface pressure fluctuations (2D Poisson solver) for the rod-airfoil case as shown in Figure 3.12. These help to predict the acoustic far-field pressure fluctuations using Curle's analogy. The study showed that at the rod shedding frequency (tonal component), the computed SPL has an accuracy of over 90% (within 3dB) with respect to the microphone measurements. At higher frequencies, TR-PIV overestimates the amplitude due to the full spanwise coherence assumption. When the spanwise coherence of velocity is measured, then the scaled coherence model predicts the amplitude with an acceptable agreement as can be seen in the Figure 3.12.

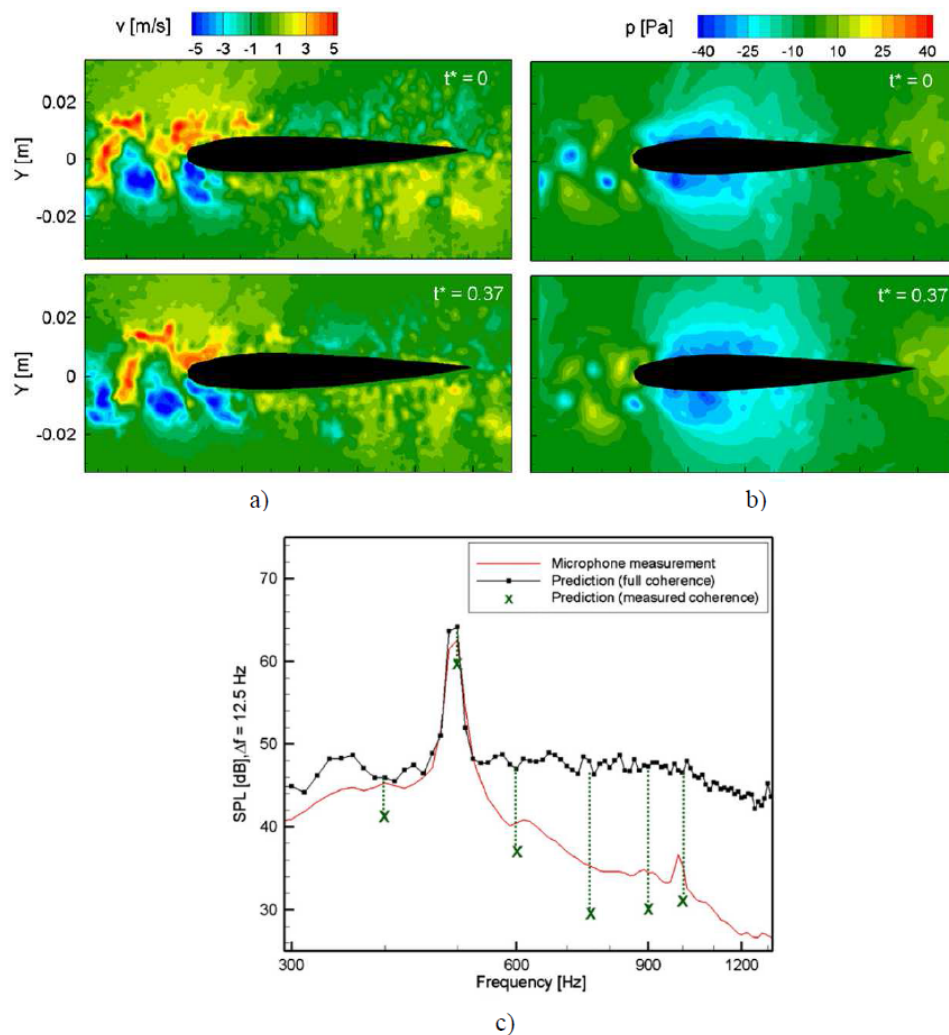


Figure 3.12: Velocity, reconstructed pressure and predicted far-field noise spectrum for a Rod-airfoil case [59]

It is clear from the above cases that this approach is able to predict noise with reasonable accuracy, thereby satisfying one of the objectives of an aeroacoustic study mentioned in section 2.2.

One drawback of the above approach, as pointed out by Henning *et al.* [60], is that the far-field noise prediction by measurements carried out in the near-field does not necessarily give a deep insight into the acoustic noise generation process. Moreover, only a small portion radiates to the far field due to the destructive interference of acoustic sources in the near-field. This destructive interference is hard to obtain since it requires computation of acoustic sources in the entire domain with high accuracy. Hence, a unanimously accepted answer to a simple question of which unsteady quantity in the near-field produces noise, for example in a jet flow, has so far not been found. A promising alternative approach which can help give an insight to the noise production process is by simultaneous measurement of acoustic pressure in the far-field together with a relevant near-field quantity. Subsequently, the far-field acoustic pressure can be *correlated* with a near-field quantity to help in the understanding of the flow structures that are involved in the sound generation process.

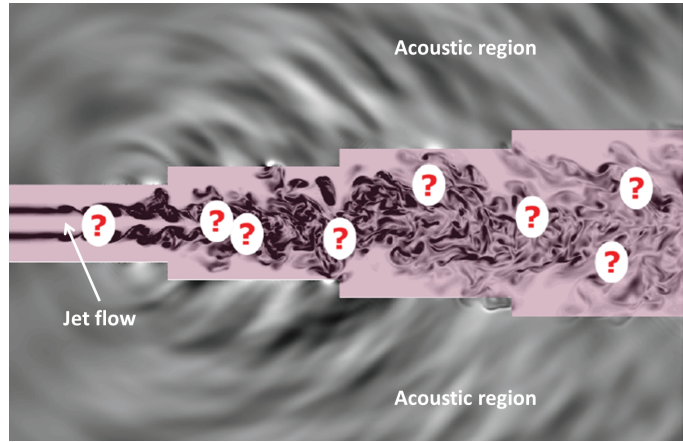


Figure 3.13: Understanding the main sources of noise

In the past, several researchers have used this approach and different near-field quantities were considered for the correlation. Siddon [61] correlated acoustic pressure with fluctuating surface pressure on a circular plate to obtain surface dipole sound sources. The term ‘causality correlation’ was coined by Siddon for this type of technique which relates the effect to the cause.

Previously, the sound pressure fluctuations measured by a fixed microphone in a jet were correlated with either velocity (Lee *et al.* [62], Schaffar [63]) or pressure (Hurdle *et al.* [64]) measured using *intrusive* turbulence measurement tools to understand jet noise. An improvement was made by Panda *et al.* [65], who used a *non-intrusive point* measurement technique based on molecular Rayleigh scattering to obtain two components of velocity and density fluctuations simultaneously that help to investigate noise sources (Lighthill’s stress tensor $\rho v_i v_j$) in high speed jets. The sound pressure fluctuations p' at the microphone angle of 30° showed the highest correlation with the turbulent fluctuations in the jet. The correlation function shows a relatively short event consisting of a single positive and negative deflection as in Figure 3.14. The peak correlation coefficients with different Reynolds decomposed terms for various microphone positions is shown in Figure 3.15. The authors showed that the fluctuations from large scale structures contributed mainly to the measured correlation while that from small-scale turbulent structures were below the noise floor. The main advantage of the correlation technique is when simultaneously measuring both the flow and acoustic field, the effects of scattering, absorption and refraction of sound in the source region, unlike in the first approach, are automatically included [65].

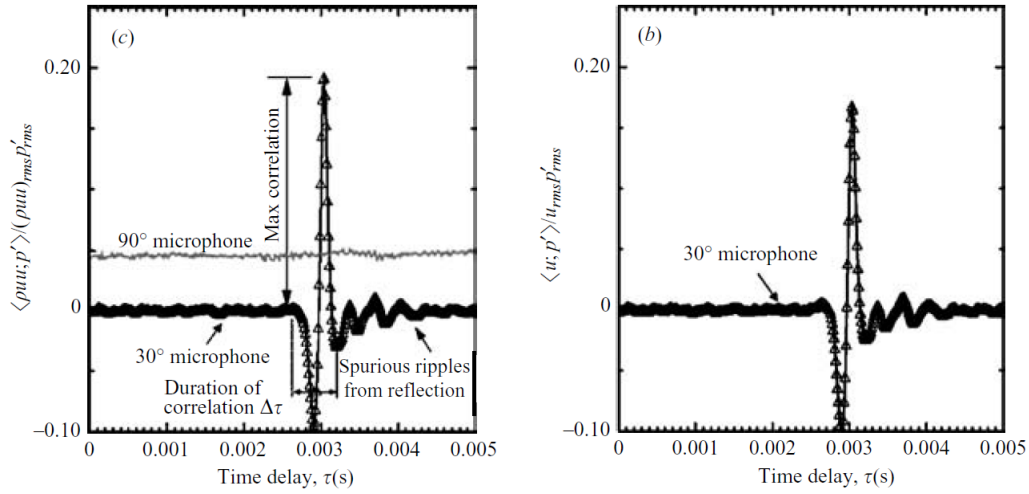


Figure 3.14: Normalized correlation coefficients for $u, \rho uu$ measured at $x/D=10$ and centerline of $M=1.4$ jet, [65]

Mach number	Probe x/D	Probe r/D	Microphone angle (deg.)	$\frac{\langle \rho uu; p' \rangle}{(\rho uu)_{rms} p'_{rms}}$	$\frac{\langle 2\bar{\rho} \bar{u} u'; p' \rangle}{(\rho uu)_{rms} p'_{rms}}$	$\frac{\langle 2\bar{\rho} \bar{u} u'; p' \rangle}{(2\bar{\rho} \bar{u} u')_{rms} p'_{rms}}$	$\frac{\langle \rho' \bar{u} \bar{u}; p' \rangle}{(\rho uu)_{rms} p'_{rms}}$	$\frac{\langle \rho' \bar{u} \bar{u}; p' \rangle}{(\rho' \bar{u} \bar{u})_{rms} p'_{rms}}$	$\frac{\langle 2\bar{u} \rho' u'; p' \rangle}{(\rho uu)_{rms} p'_{rms}}$
1.8	12	0	30	0.2207	0.1635	0.2094	0.0636	0.2129	-0.00214
1.8	6	0.45	30	0.0572	0.0406	0.0554	0.0201	0.0616	-0.0022
1.4	10	0	30	0.1919	0.1344	0.168	0.0624	0.17	-0.0021
0.95	10	0	30	0.0682	0.0592	0.064	0.01	0.028	0.0001
0.8	8	0	30	0.022	0.0198	0.019	0.0037	0.011	-0.0003
				$\frac{\langle 2\bar{u} \rho' u'; p' \rangle}{(2\bar{u} \rho' u')_{rms} p'_{rms}}$	$\frac{\langle \bar{\rho} u' u'; p' \rangle}{(\rho uu)_{rms} p'_{rms}}$	$\frac{\langle \bar{\rho} u' u'; p' \rangle}{(\bar{\rho} u' u')_{rms} p'_{rms}}$	$\frac{\langle \rho' u' u'; p' \rangle}{(\rho uu)_{rms} p'_{rms}}$	$\frac{\langle \rho' u' u'; p' \rangle}{(\rho' u' u')_{rms} p'_{rms}}$	
				-0.042	-0.0025	-0.066	0.003	0.1707	
				-0.017	-0.0023	-0.028	0.0011	0.055	
				-0.0173	-0.0041	-0.0787	0.0014	0.14	
				0.001	-0.0019	-0.0095	0.0007	0.015	
				-0.0022	-0.0012	-0.0044	0.0003	0.0062	

Peak correlation coefficients between far-field sound pressure fluctuations and various Reynolds decomposed terms of ρuu .

Figure 3.15: Peak correlation coefficients for high speed jet [65]

The correlation technique using a *non-intrusive whole field* measurement tool: PIV, was first applied to generic flows such as a cylinder wake (Henning *et al.*, [60]), rod-airfoil configuration (Henning *et al.* [66]) and a free jet (Henning *et al.* [67]). Synchronized PIV (for near-field) and microphone measurements (for acoustic far-field) were carried out. Since a *low speed* PIV system (2D-2C) was used, the flow structures subject to the same physical phenomena as the aeroacoustic sources were identified in a statistical manner.

The correlation between far-field pressure fluctuations and the Lamb vector, $\omega \times \mathbf{v}$ (Powell, Howe) as explained by in section 2.2(Vortex sound theory) is used to characterize the part of the source strength that contributes to the acoustic pressure in the far field. The vorticity

and velocity is split into its mean and fluctuating components,

$$\boldsymbol{\omega} = \bar{\boldsymbol{\omega}} + \boldsymbol{\omega}' \quad (3.11)$$

$$\mathbf{v} = \bar{\mathbf{v}} + \mathbf{v}' \quad (3.12)$$

The relationship for the cross correlation is then given by (Henning *et al.*, [60]),

$$\langle (\boldsymbol{\omega} \times \mathbf{v})_i p' \rangle = (\bar{\boldsymbol{\omega}} \times \bar{\mathbf{v}})_i \langle p' \rangle + (\bar{\boldsymbol{\omega}} \times \langle \mathbf{v}' p' \rangle)_i + (\langle \boldsymbol{\omega}' p' \rangle \times \bar{\mathbf{v}})_i + \langle (\boldsymbol{\omega}' \times \mathbf{v}')_i p' \rangle$$

- The first term $(\bar{\boldsymbol{\omega}} \times \bar{\mathbf{v}})_i \langle p' \rangle$ is zero, as the acoustic pressure has a zero mean value.
- The second term $(\bar{\boldsymbol{\omega}} \times \langle \mathbf{v}' p' \rangle)_i$ contains the fluctuating velocity \mathbf{v}' .
- The third term $(\langle \boldsymbol{\omega}' p' \rangle \times \bar{\mathbf{v}})_i$ contains the fluctuating vorticity $\boldsymbol{\omega}'$.
- The fourth term $\langle (\boldsymbol{\omega}' \times \mathbf{v}')_i p' \rangle$ contains both fluctuating velocity and vorticity.

Therefore, the correlations that have to be calculated are $\langle \mathbf{v}' p' \rangle$, $\langle \boldsymbol{\omega}' p' \rangle$ and $\langle \boldsymbol{\omega}' \times \mathbf{v}', p' \rangle$. 2D-2C PIV measures the velocity field in a plane from which only the out-of-plane component of vorticity (ω_z) and two in-plane component of velocity (u, v) can be determined. Although the complete vector $\boldsymbol{\omega} \times \mathbf{v}$ and consequently, the complete correlation of the source term $\langle (\boldsymbol{\omega} \times \mathbf{v})_i p' \rangle$ cannot be obtained from the experimental data, the out-of-plane components of the correlation $\langle \boldsymbol{\omega}' p' \rangle$, and in-plane component of the correlation $\langle \mathbf{v}' p' \rangle$ can be determined. The cross correlations of the acoustic field with \mathbf{v}' , $\boldsymbol{\omega}'$ will help determine the processes in the near-field that are responsible for the main part of the radiated sound.

3.3.1 Causality correlation applied to a Cylinder

This method was first applied in understanding flow induced noise in a cylinder at Reynolds number $Re=19000$. Simultaneous measurement of the velocity field using planar PIV and the radiated sound using microphones was carried out in a closed test section by Henning *et al.* [60]. A predominant aeolian tone (first observed by Strouhal in 1878) was found as seen clearly in the Figure 3.17. The aeolian tone having a frequency, $f=265\text{Hz}$ ($St=0.186$) has a dipole character radiating strongly in the direction perpendicular to the freestream (as theoretically explained by Etkin *et al.* 1957).

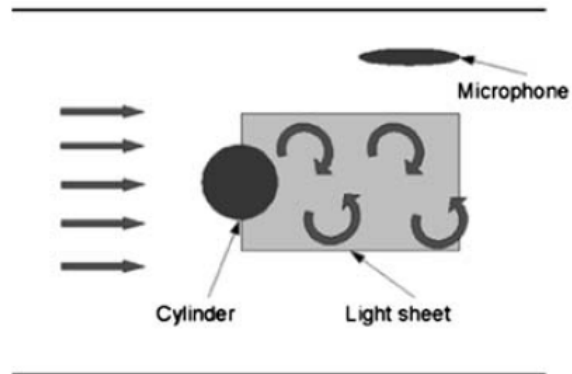


Figure 3.16: Schematic for experimental set-up in cylinder case [60]

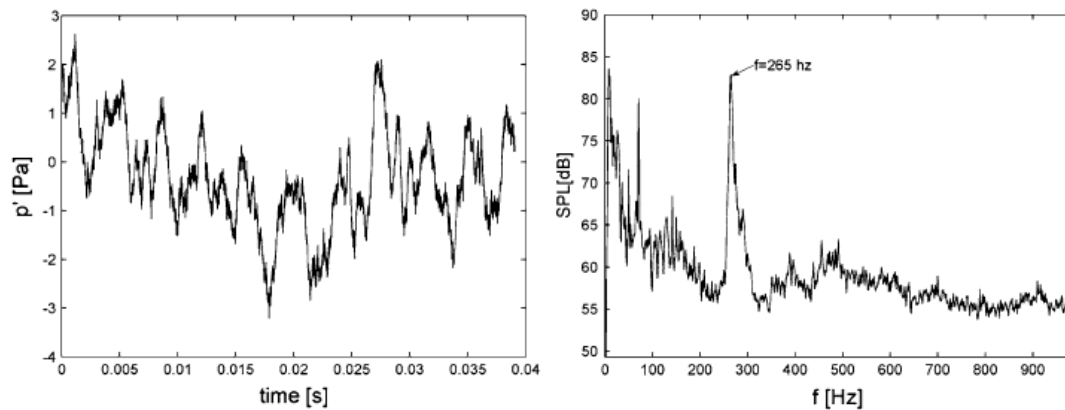


Figure 3.17: Time sequence of the recorded sound pressure and corresponding acoustic power spectrum (Henning *et al.*)

The instantaneous spatial distribution of correlations $R_{u'p'}$, $R_{v'p'}$, and $R_{\omega'_z p'}$ calculated for the cylinder case showed (see Figure 3.18):

- The sign of the correlation coefficient alternates between positive and negative values in the downstream of the cylinder wake. It is almost zero outside the wake.
- The distance between the two neighboring maxima increase in the downstream direction. This is attributed to the effect of accelerating vortices.
- The maximum correlation coefficient was found to be at a downstream distance of 1.6D where rapid acceleration of the released vortices takes place, after which it decreases in the downstream direction. This was explained by using Howe's theory which predicts that the majority of sound is generated in the initial period of acceleration.

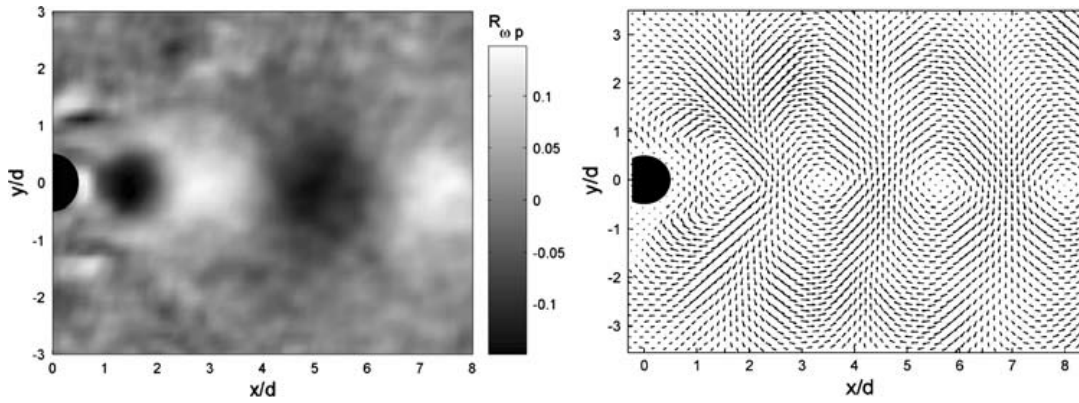


Figure 3.18: Instantaneous distribution of normalized cross correlation coefficient ($R_{\omega'_z p'}$) and $R_{u',p'} R_{v',p'}$ [60]

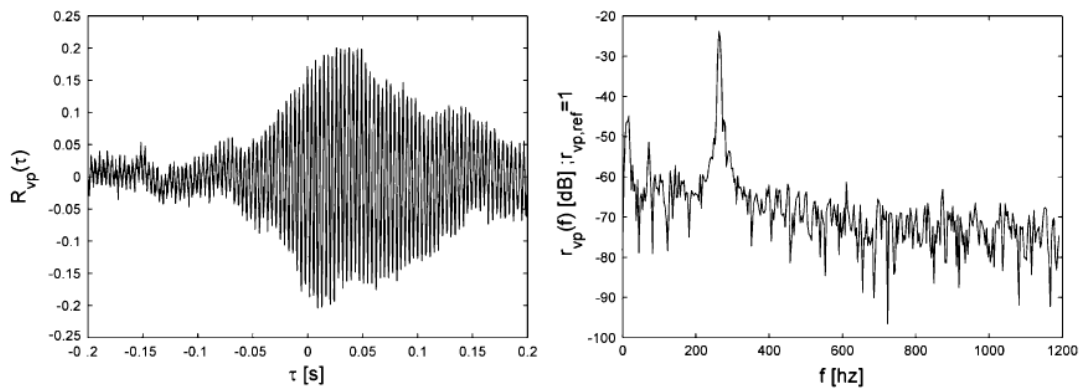


Figure 3.19: Temporal evolution of normalized cross correlation coefficient and corresponding cross spectrum [60]

The temporal evolution of the cross correlation coefficient showed a sine type of oscillation (similar to the input velocity and acoustic pressure signals) due to the coherent periodic

structures in the flow field, with a maximum value of $|R_{v'p'}|=0.2$ at $\tau = 0.025s$ (where, $\tau = \tau' - \frac{r}{c_0}$ is the retarded time shift). Figure 3.19 differs largely from the correlation function for the jet noise obtained by Panda *et al.* (Figure 3.14) which shows a relatively short event. The predominant oscillation is equal to the shedding frequency of the cylinder wake as can be seen from the cross power spectrum (See Figure 3.20). The coherent periodic structures generate a sound field with the same periodicity which is perceived as a tone. It was observed that due to the reflections in a closed test section the maximum amplitude of the correlation function is not at the value of τ_0 (which is the travel time directly from the cylinder to the microphone), but at larger positive delay time τ .

Proper orthogonal decomposition - POD (explained in the next section) was applied to the velocity field and cross correlation with acoustic pressure was carried out for different eigenmodes. The temporal evolution of $R_{ap'}$ using coefficients of different eigenmodes is shown in Figure 3.20. The temporal evolution of $R_{ap'}$ using the amplitude time-series of the first eigenmode coefficient had a similar time dependent behaviour as $R_{v'p'}$, showing that $R_{v'p'}$ acts like a filter for the most energy structures present in the flow that are responsible for sound generation. Also, $R_{ap'}$ showed no significant increase in the maximum value of the correlation coefficient as compared $R_{v'p'}$.

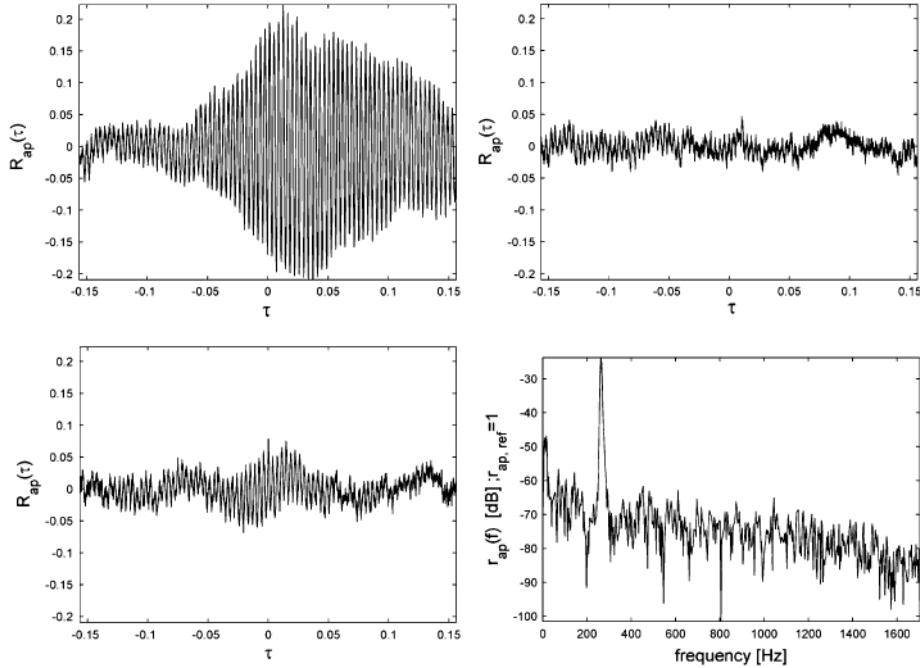
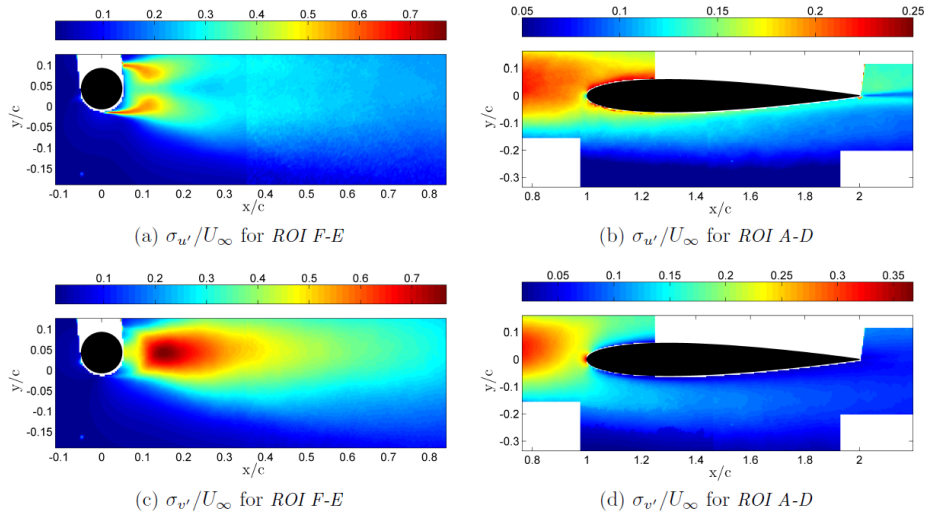


Figure 3.20: Instantaneous distribution of correlation coefficient using coefficients/amplitude time series of different eigenmodes (1-top left, 2-top right, 3-bottom left) $R_{v'p'}$ and spectra using amplitude time series of the 1st eigenmode [60]

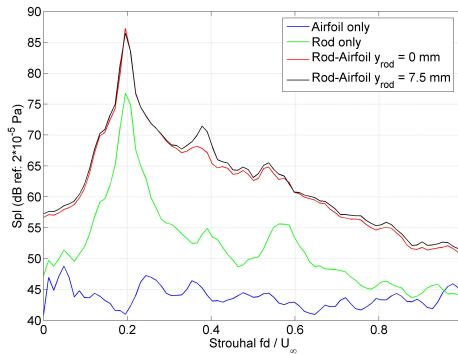
Henning *et al.* concluded that the vortices shed and the fluctuations in the wake are responsible for the strong tonal noise in the cylinder case. The tonal noise had a dipole character that is related to the varying lift forces acting on the cylinder radiating mostly in the direction perpendicular to freestream.

3.3.2 Causality correlation applied to a Rod - Airfoil

The correlation technique was subsequently applied to investigate the sound generation process for the rod-airfoil configuration using simultaneous planar PIV and acoustic measurements in an anechoic facility [66]. Higher values of $\sigma_{v'}$ are observed in the near wake region of the cylinder where rapid acceleration of the vortices takes place as shown in Figure 3.21. At the airfoil LE, values of $\sigma_{v'}$ are higher than $\sigma_{u'}$ indicating the energy transfer from u' to v' very close to the airfoil LE. The acoustic spectrum (see Figure 3.21) indicates the amplitude of noise generated by the vortices impinging on the airfoil LE is higher by about 10dB when compared to the noise generated by only the cylinder.



(a) Statistical flow quantities obtained from the PIV measurement (RMS) [66]



(b) Acoustic spectrum for different configurations [66]

Figure 3.21: Flow statistics and acoustic spectrum [66]

The instantaneous distribution of the correlation coefficient $R_{v',p'}$ computed by Henning *et al.* (see Figure 3.22) showed a similar trend with positive and negative values in the downstream of the cylinder. However, the magnitude of the correlation coefficient is higher in the cylinder wake and not at the ‘origin of source’, i.e. the airfoil leading edge (as explained in mechanisms of noise generation section 2.2). This is attributed to the flow structures becoming less periodic and more three dimensional with increasing downstream distance from the cylinder.

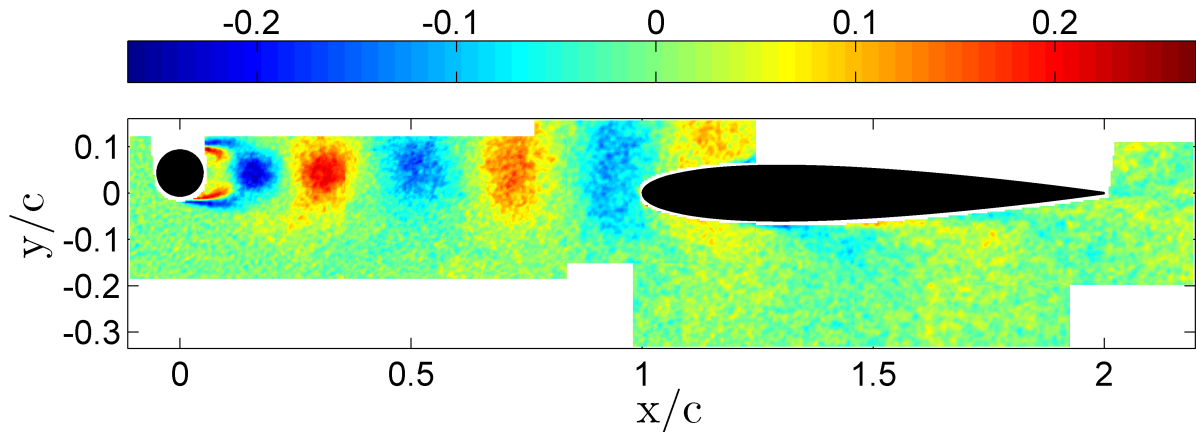


Figure 3.22: Maximum correlation coefficient $R_{v',p'}$ for Rod-Airfoil case [66]

The study pointed out that the maximum correlation coefficient alone cannot be interpreted as the origin of sound source. The true source region can be identified when the temporal evolution of $R_{v',p'}$ at the airfoil leading edge is compared with that in the cylinder wake. In absence of reflections from the wall (anechoic chamber) such as in this case, the difference in the maximum value of $R_{v',p'}$ for the airfoil leading edge is at $\tau \approx 0$ whereas in the cylinder wake it is at $\tau = 3ms$ indicating the airfoil leading edge to be the main source of noise. The study also shows the importance of coherent flow structures and its influence on the temporal and spatial distribution of the correlation coefficients.

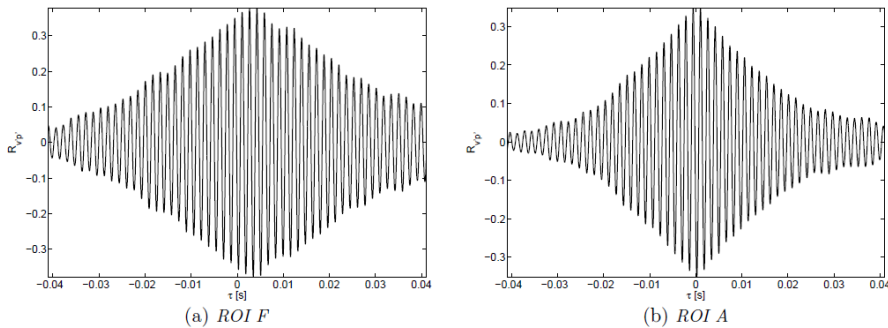


Figure 3.23: Temporal evolution of normalized cross correlation coefficient and corresponding cross spectrum [66]

3.3.3 Causality correlation applied to a Slat: High Lift Device

After applying the causality technique to generic flows that were described above, the noise sources at the leading edge slat in a high lift device configuration was studied by Henning *et al.* [68]. In the first attempt (Henning *et al.* [60]) the signal-to-noise ratio of the correlation values obtained for the slat-flow case in a closed test section were too low to identify noise sources. This was due to the low number of PIV recordings ($N=5000$), as a result averaging could not sufficiently suppress the uncorrelated parts of the measured quantities.

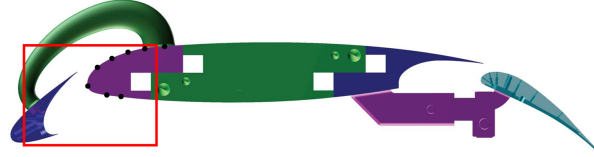


Figure 3.24: Cross section of the F16 wing model used to study slat noise [68]

The measurements were carried out again with sufficient PIV recordings ($N=16000$) in free field anechoic conditions. Figure 3.25 shows the mean velocity field obtained from PIV for different angles of attack. The important characteristics of slat flow consists of development of a shear layer due to separation from the slat-cusp, a recirculation region in the slat-cove and an acceleration of the flow in the slat gap. With an increase in angle of attack, the curvature of the shear layer increases resulting in a smaller circulation region and a reattachment point further upstream. This shear layer breaks up into discrete vortices which impinge on the slat-cove wall or get trapped inside the recirculation region.

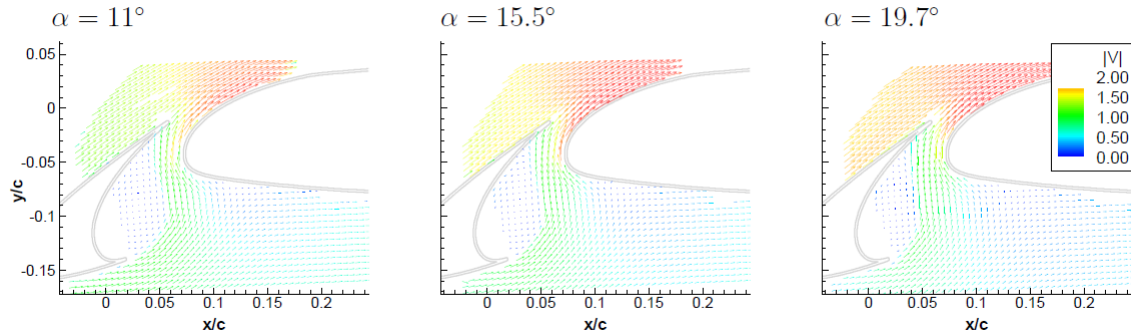


Figure 3.25: Mean velocity vector maps for different angles of attack [68]

The acoustic spectrum using microphones on the suction side (Figure 3.26 left), pressure side (Figure 3.26 right) shows strong tonal components (frequency: 1900, 2300, 3100 Hz) are present for $\alpha = 11^\circ$. Thereafter, the tonal peaks are reduced for $\alpha = 15.5^\circ$ and not present for $\alpha = 19.7^\circ$.

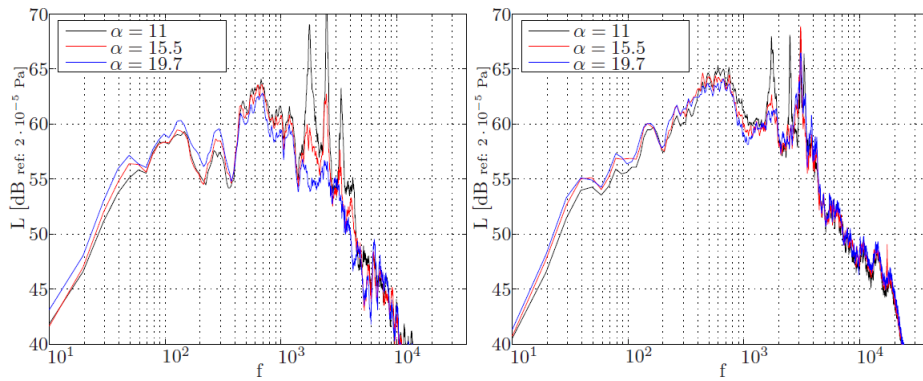


Figure 3.26: Acoustic spectrum for different angles of attack [68]

The spatial distribution of maximum values of cross correlation coefficient showed significant values ($\alpha = 11^\circ$, $\alpha = 19.7^\circ$) in the trajectory of the shear layer originating from the slat cusp. The results also showed a strong dependency on directivity i.e. calculating correlation using acoustic pressure measured from the microphones placed on the pressure side or the suction side.

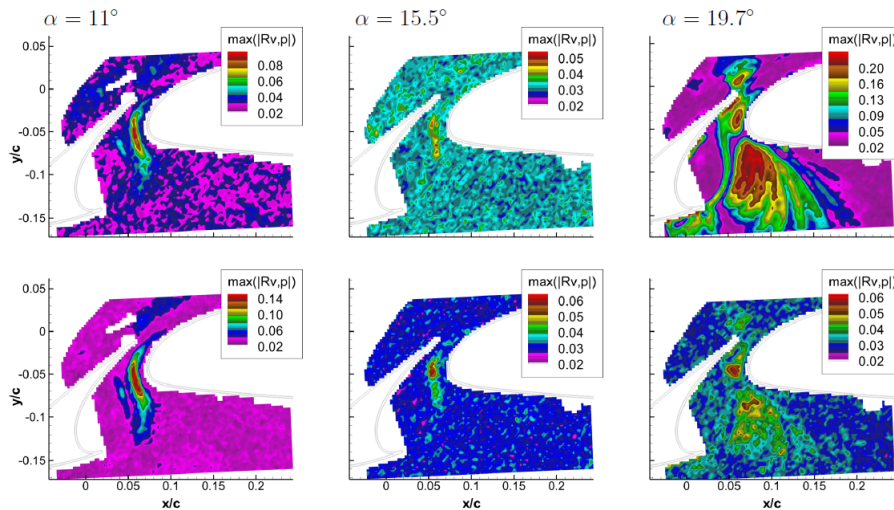


Figure 3.27: Spatial distribution of the maximum coefficient values $R_{vp}(x, \tau)$ [68]

The instantaneous distribution of the cross correlation coefficients at $\tau = 0$ for $\alpha = 11^\circ$ shows patterns of positive and negative values that, as seen in previous applications, correspond to discrete vortices originating from the slat-cusp. The vortices are accelerated and subsequently ejected through the slat-gap. These coherent structures are responsible for the tonal peaks present in this configuration. For $\alpha = 15.5^\circ$, a smaller region of significant correlation values are observed. For $\alpha = 19.7^\circ$, a single maximum peak with no periodicity indicates the acoustic source process to have a broadband characteristic, confirming the absence of tonal peaks in the acoustic spectrum.

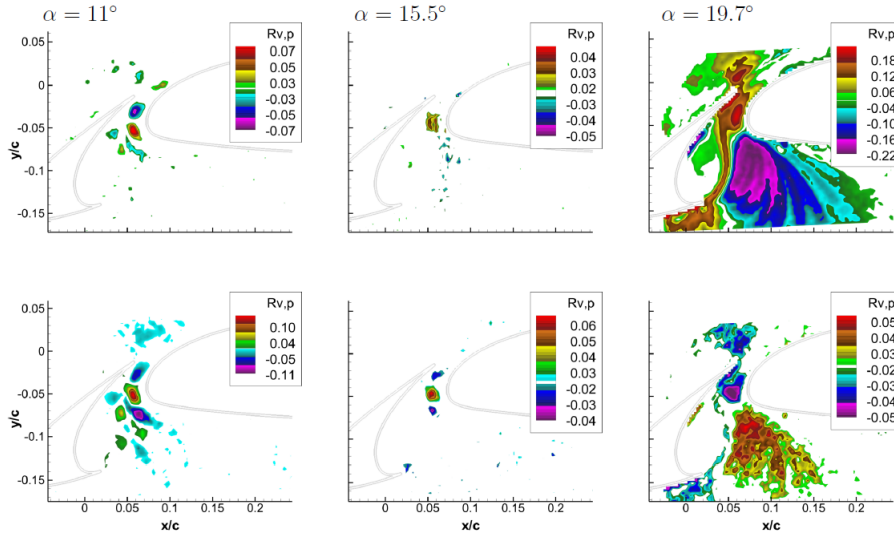


Figure 3.28: Instantaneous distribution of $R_{v,p}$, $\tau = 0$ [68]

This technique has also been applied to a free jet (Henning *et al.* [67]) and a fan-blade (Nashimoto *et al.* [69]). So far, flows both dominated by large scale coherent structures and/or having a more broadband noise characteristic have been investigated using the causality correlation technique. There is however an ambiguity in the interpretation of the correlation results (Henning *et al.* [70]). For example, in the rod airfoil case Henning *et al.* identified the peak signature present at the airfoil LE as the main source of noise as shown in Figure 3.3.3. Breakey *et al.* [71] used a numerical model involving analytical sound sources to show that peak signature doesn't necessarily have to be the main source and that the causality correlation technique is unable to uniquely locate the strongest source activity when the flow is dominated by a single frequency and correlated in a large spatial do-

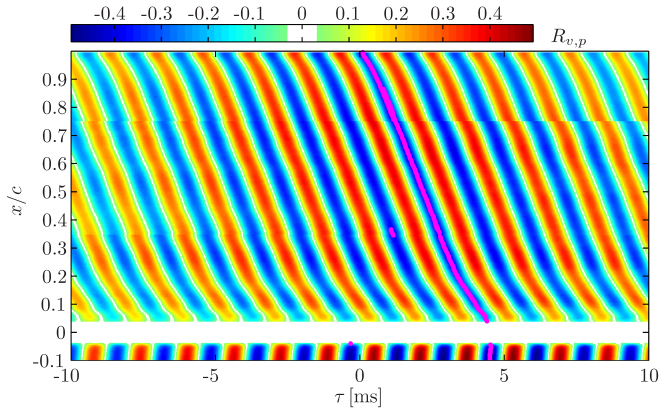


Figure 3.29: Space-time distribution of Correlation coefficient for Rod-airfoil case [66]

minated by a single frequency and correlated in a large spatial do-

main. Subsequently, Henning *et al.* discussed that the downstream peaks are present because the structures are correlated with the upstream source and are themselves not involved in the production of acoustic sources. The observed time lag in the correlation peaks are due to the convection of these coherent structures. Also, the truncation error caused by limited spatial domain of the numerical models is the reason for the peak correlation signature obtained by Breakey *et al.*

A possible improvement that can help pinpoint the main source of noise and the influence of coherent structures on correlation signatures can be made by using TR-PIV. In the present case of the Gurney flap, *time-resolved* velocity field obtained using TR-PIV is correlated with the far-field acoustic pressure.

3.4 Data Reduction

The techniques used in the thesis to extract relevant flow and acoustic variables from TR-PIV and microphone measurements that aid in understanding the acoustic sources in a Gurney flap are discussed below.

The Reynolds decomposition of the flow and acoustic quantities is carried out. For example for the u velocity component,

$$u(t) = \bar{u} + u'(t) \quad (3.13)$$

where \bar{u} is the mean given by,

$$\bar{u} = \sum_{i=1}^N \frac{u_i}{N} \quad (3.14)$$

and u' is the fluctuations. The RMS of the near-field or acoustic fluctuations usually used for normalization is calculated by,

$$\sigma_u = \sqrt{\frac{1}{N} \sum_{i=1}^N u_i'^2} \quad (3.15)$$

The time-resolved data acquired in the thesis reduces the number of uncorrelated or independent samples that are necessary to achieve statistical convergence. The effective number of independent samples in case of TR-PIV is given by,

$$N_{eff} = \frac{N}{2T_I} \quad (3.16)$$

where T_I is the integral time scale of the flow is given by the integral of the autocorrelation of $u(t)$ or $v(t)$,

$$T_I = \int_0^{\infty} \rho(\tau) d\tau \quad (3.17)$$

Hence, a higher number ($\approx 10k$) of samples is acquired in most cases.

3.4.1 Spectral Analysis

Correlation

The Pearson product moment correlation coefficient or cross correlation or simply correlation is a statistical operation that is a measure of dependence between two sets of data that are a function of time and/or space. For example, 2D (spatial) cross correlation is used to obtain the particle displacement from PIV images as explained in section 3.1.

In the aeroacoustic investigation using the causality correlation approach, the normalized cross correlation coefficient $R_{\phi,p'}(\mathbf{x}, \mathbf{y}, \tau)$ is defined as (Henning *et al.*[60]),

$$R_{\phi,p'}(\mathbf{x}, \mathbf{y}, \tau) = \frac{S_{\phi,p'}(\mathbf{x}, \mathbf{y}, \tau)}{\sigma_{\phi}(\mathbf{y})\sigma_{p'}(\mathbf{x})} \quad (3.18)$$

$$= \frac{\langle \phi(\mathbf{y}, t)p'(\mathbf{x}, t + \tau) \rangle}{\sqrt{\langle \phi^2(\mathbf{y}, t) \rangle \langle p'^2(\mathbf{x}, t) \rangle}} \quad (3.19)$$

where, $\phi(\mathbf{y}, t)$ represents near-field fluctuations such as v' , ω' measured using TR-PIV at position \mathbf{y} and discrete time t . $p'(\mathbf{x}, t)$ represents the far-field acoustic pressure fluctuations measured by the microphones. The cross correlation coefficient is normalized by the root-mean-square values of ϕ , $\sigma_{\phi}(\mathbf{y})$ and p' , $\sigma_{p'}(\mathbf{x})$ so that the value lies between -1 and 1. The variable τ is the time shift between the pressure signal and the near-field quantity ϕ . The flow field is recorded by the high speed PIV system at discrete times t_n . The far-field acoustic pressure fluctuations is recorded at discrete times simultaneously with the PIV system but with a much higher acquisition frequency and number of samples. The cross correlation between the near-field quantity and the acoustic pressure signal is calculated in a discrete manner using,

$$S_{\phi,p'}(\mathbf{x}, \mathbf{y}, \tau) = \frac{1}{N} \sum_{n=1}^N [\phi(\mathbf{y}, t_n)p'(\mathbf{x}, t_n + \tau)] \quad (3.20)$$

where N is the number of PIV measurements which is a critical parameter for statistical convergence. Some important points on correlation are,

- Cross correlation coefficient value of +1 means the two signals have a perfect increasing linear relationship, while a value of -1 means the two signals have a perfect decreasing linear relationship i.e. one increasing while the other is decreasing. The values between -1 and +1 indicate the degree of linear dependence between the signals (0 indicates that they are uncorrelated). The coefficient indicates the strength of a linear relationship between the two signals.
- The operation of correlating a signal itself is termed as auto-correlation. Auto correlation helps detect a known *waveform* (repeated pattern) in a signal (Smith, 1998). The autocorrelation function gives the maximum value(=1) corresponding to a zero shift ($\tau = 0$). On the other hand, the cross correlation function does not necessarily have a maximum at $\tau=0$.

- Correlation is used to get typical length scales in turbulent flows. Spanwise correlation length is used in the thesis to see the size of coherent turbulent structures (in the spanwise direction) downstream of the Gurney flap.
- It is worthwhile to mention here that correlation applied to stationary or ergodic signals (whose mean or expected value does not vary with time) does not imply causation, however, in aeroacoustics it is rather clear the fluctuations in the flow are producing the acoustic noise sources and not the other way around.

Power Spectral Density

The auto-correlation operation applied to a ergodic/stationary signal identifies the periodicity present in it.

$$R_{p'p'}(\tau) = \langle p'(t)p'(t + \tau) \rangle \quad (3.21)$$

The Fourier transform of the auto-correlation function decomposes it into different frequencies giving the power spectral density (PSD).

$$S(\omega) = \frac{1}{2\pi} \int_{-\infty}^{\infty} R(\tau)e^{-i\omega\tau} d\tau \quad (3.22)$$

It represents the way energy is distributed as a function of frequency. In this way, the amplitude (for noise, after normalizing and taking the logarithm gives the SPL in dB as explained in section 2.2) as well as different frequencies of the acoustic far-field and flow fluctuations can be obtained. Due to the noise present in the signal, Welch's method is used to compute the PSD. The signal is divided into a number of overlapping segments. The periodograms are computed for each segment with a Hamming function by applying Fast Fourier Transform (FFT). These are averaged to get an estimate of the power spectrum.

Coherence

Coherence is a similar concept as correlation, except it is a measure of the dependence between two sets of data in the frequency domain. The complex coherence function is given by,

$$\gamma_{\phi,p'}(f) = \frac{G_{\phi,p'}(f)}{\sqrt{G_{\phi,\phi}(f)G_{p',p'}(f)}} \quad (3.23)$$

The magnitude squared coherence is obtained by,

$$\gamma_{\phi,p'}^2(f) = \frac{|G_{\phi,p'}(f)|^2}{G_{\phi,\phi}(f)G_{p',p'}(f)} \quad (3.24)$$

where $G_{\phi,p'}(f)$ is the cross spectral density between the near-field fluctuations and the far-field acoustic pressure fluctuations that is given by the Fourier transform of the cross correlation function between them. $G_{\phi,\phi}(f)$ and $G_{p',p'}(f)$ are the auto-spectral densities of the near and far-field fluctuations respectively. The phase difference between the near and far-field fluctuations is given by the argument of $\gamma_{\phi,p'}$.

3.4.2 Proper Orthogonal Decomposition

An important realization was that turbulent flows also consists of coherent structures and not only small random eddies. One of the techniques that help describe these coherent structures is the Proper Orthogonal Decomposition (POD, Berkooz *et al.* [72]). POD is a statistical technique that is applied to the PIV velocity data and helps in describing the most energetic coherent structures in terms of its eigenmodes. The total kinetic energy present in the statistical fluctuations is proportional to its eigenvalue (Meyer *et al* [73]). The order of eigenvalues are such that the most important modes in terms of energy are the first modes, which are usually associated with large scale flow structures. The mathematical background of POD using the method of snapshots can be found in Berkooz *et al.*

In the thesis, POD along with PSD is used to explore the possibility of a secondary mode of shedding in the Gurney flap (Troolin *et al.* [32]).

Chapter 4

Experimental Set-up

Measure what is measurable and make measurable what is not so.

Galileo Galilei

The previous chapter gave an insight into the experimental techniques that are used in the aeroacoustic investigation of a Gurney flap. This chapter aims at describing in detail the experimental set-up that is used. It includes a description of the wind tunnel facility, models and test section manufactured, details on Planar, Stereo PIV set-up as well as the microphone measurements. In the end a brief description of the various techniques used in processing the PIV images is also included.

4.1 Wind tunnel facility

All the experiments are carried out at the vertical low turbulence wind tunnel facility (V-tunnel) available at the low-speed laboratory of the Department of Aerospace Engineering, TU Delft. A schematic diagram of the V-tunnel is shown in Figure 4.1. The quality of airflow is high with the freestream turbulence intensity level below 1%. The operating velocity range of the tunnel is 5 - 45m/s. The tunnel has an open-section circular exit of diameter 0.6m. In the experiments a circular to square exit of 0.4m is used to accommodate the test section. In the absence of an anechoic wind tunnel facility, the V-tunnel is used for all aeroacoustic experiments at TU Delft due to a relatively low background noise level.

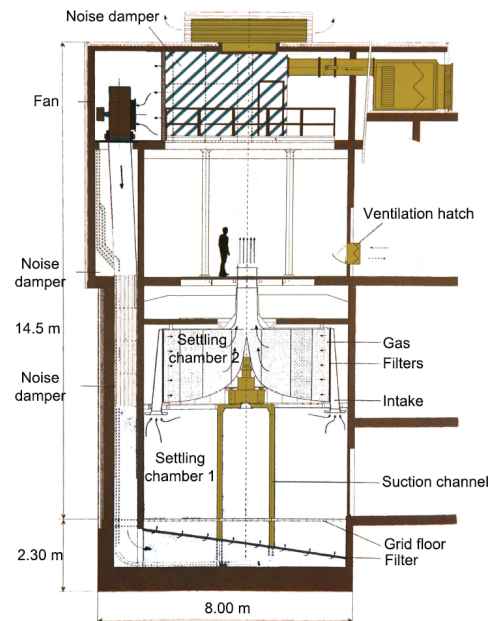


Figure 4.1: Schematic diagram: Vertical Wind Tunnel [74]

4.2 Models and Test section

The Gurney flap models are manufactured in-house at the main workshop of the Faculty of Aerospace Engineering using a CNC machine. The detachable Gurney flap models of size 2%, 4%, 6% on a NACA 0015 airfoil, similar to the models used by Troolin *et al.*, are shown in Figure 4.2. The models have a chord of 20cm and a span of 40cm. The flaps are made out of plexiglass to allow laser light in order to perform PIV measurements simultaneously on the pressure and the suction side, if needed. To ensure a fully turbulent boundary layer, roughness elements consisting of carborundum grains of height 0.841mm are used to trip the boundary layer at $0.25c$ on both the suction and the pressure side of the NACA 0015 airfoil. To ensure a turbulent boundary layer is present on both the sides, a microphone with a loudspeaker is used to check (a turbulent boundary layer produces random noise).

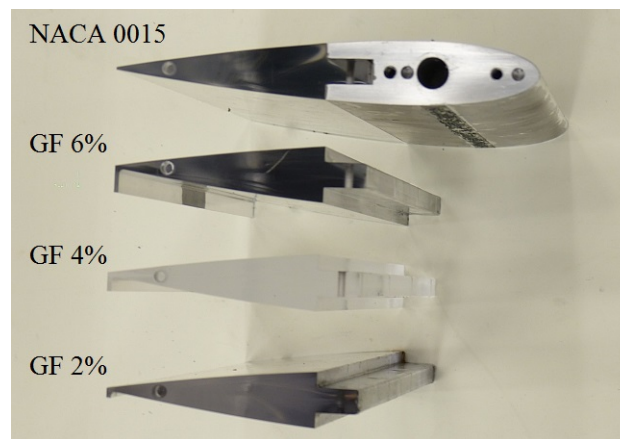


Figure 4.2: Gurney flap models manufactured at TU Delft

To avoid any uncertainty in the angle of attack, for the reason of comparison with previous literature of Troolin *et al.*, a closed test section made of plexiglass is built. Since a closed plexiglass test section is not ideal to carry out the aeroacoustic measurements, acoustically transparent test sections (Debrouwere [75]) using Kevlar material on two sides are used as shown in Figure 4.3.



Figure 4.3: Test Section for PIV (left), Acoustics (right)

4.3 Planar PIV set-up

A schematic diagram for the Planar PIV measurements is shown in Figure 4.4. A Quantronix Darwin-duo dual cavity/single head pulsed Nd:YLF laser ($\lambda = 527nm$, pulse repetition rate = $0.1 - 10kHz$) is used in all the experiments for illumination. The average power output of the laser is 80W at 3kHz. The laser sheet optics in most cases consists of a 200mm spherical lens, -150mm spherical lens and a -80mm cylindrical lens arranged in this order. The laser sheet thickness is measured to be approximately 1mm. Two photron FASTCAM SA1 CMOS cameras (1024×1024 pixels, 12-bit, $20\mu m$ pixel pitch) placed on either side of the test section are used for image acquisition. This is done to increase the spatial resolution. The sensor is cropped to 512×512 pixels to acquire images at a much higher frequency. The synchronization between the laser and camera(s) is performed using LaVision High speed controller and DAVIS 8.2 software. The flow is seeded by means of SAFEX smoke generator (non-toxic water-glycol based fog) with particles of size $d_p \approx 1\mu m$.

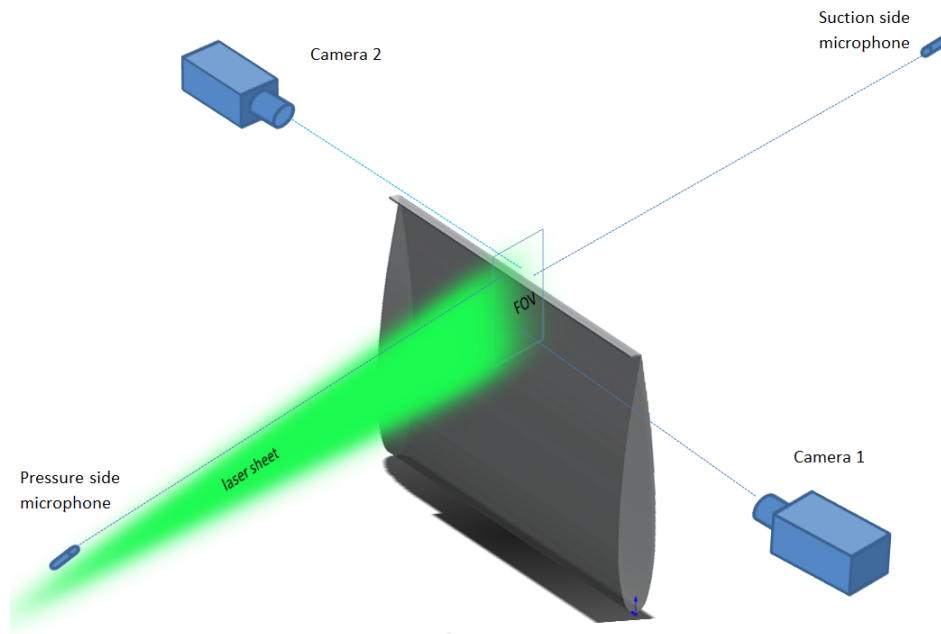


Figure 4.4: Schematic diagram for the Planar PIV set-up (shown without the test section for clarity)

Boundary layer measurements:

To evaluate the statistical properties of the boundary layer, measurements are carried out on the suction side of Gurney flap 4% and in the clean (without a Gurney flap) case using a single camera (camera 2, as shown in Figure 4.4). The flow and the PIV recording parameters are shown in Table 4.1. The pulse separation, dt , depends on the freestream velocity and is evaluated such that the pixel displacement is typically around 10-12 pixels in regions where the flow is almost equal to freestream velocity and 2-3 pixels in regions where flow is much

slower as compared to freestream velocity.

Flow Velocity, V	10, 15, 20, 25, 30 m/s
Angle of attack, α	$0^\circ, 4^\circ, 8^\circ$
Field of View, FOV	$40 \times 40mm^2$
Sensor size	1024×1024 pixels
Magnification, M	0.4
Focal length, f	180 mm
Numerical aperture, $f_\#$	5.6
PIV acquisition frequency, f_s	50 Hz
Pulse separation, dt	75, 45, 35, 30, 25 μs
Recording mode	Single frame
Number of images, N	2700

Table 4.1: Boundary layer: 2C-PIV recording and flow parameters

The vortex shedding in the Gurney flap is assumed to be periodic in nature as a result in the first campaign, *non-simultaneous* measurements of the flow and acoustics are carried out. This is done due to the restrictions kevlar had in passing the laser light and also to avoid the noise generated by the laser power/cooling system interfering the acoustic measurements. However, poor quality results of causality correlation are obtained from this campaign. Although the vortex shedding in the Gurney flap case is periodic, random phase changes are found that bring the overall values of correlation down. It was therefore necessary to acquire measurements simultaneously and in a synchronized manner.

An innovative approach for acquiring *simultaneous* measurements of the flow and acoustics is carried out in the second campaign. This is done by allowing the laser light through the kevlar using a slit as shown in Figure 4.5. The noise from the laser power system is removed in the second campaign by keeping it outside the wind tunnel measurement area.

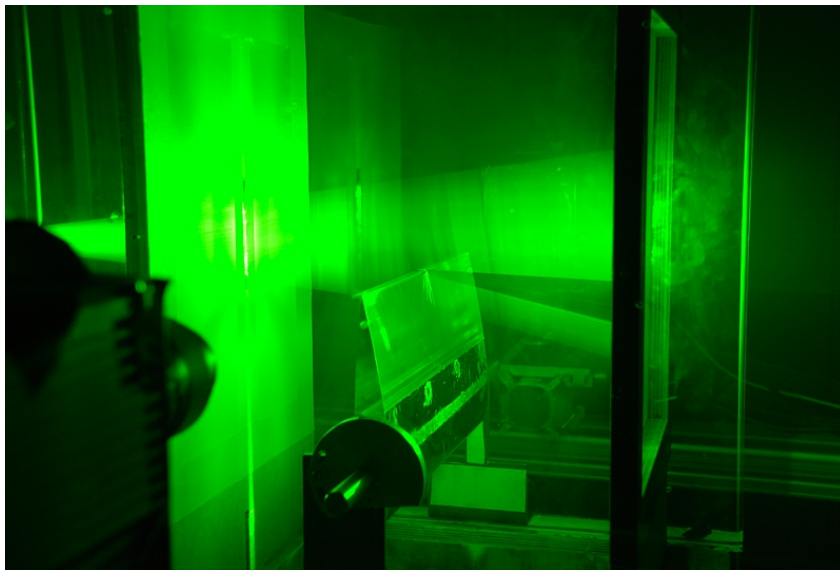


Figure 4.5: Photograph of the experimental set up to acquire simultaneous measurements

Simultaneous synchronised measurements of flow and acoustics are carried out for the GF 6% and GF 4% cases using two cameras (for a larger FOV) and four microphones (two each on suction and pressure side) with the set up shown in Figure 4.5, Figure 4.6. The flow and PIV recording parameters are shown in Table 4.2. The details of acoustic measurements are discussed in the next section. An overlap of 1cm in the field of view of both cameras is kept to effectively stitch the velocity fields obtained after processing of PIV images. Images are acquired in double frame mode at frequencies of 5kHz and 8kHz at freestream velocities 20 m/s and 30 m/s respectively. The time delay between the first and second frame is $40 \mu s$ (V20) and $25 \mu s$ (V30) depending on the freestream velocity. DAVIS 8.2 is used for processing of the PIV images, discussed in section 4.6.

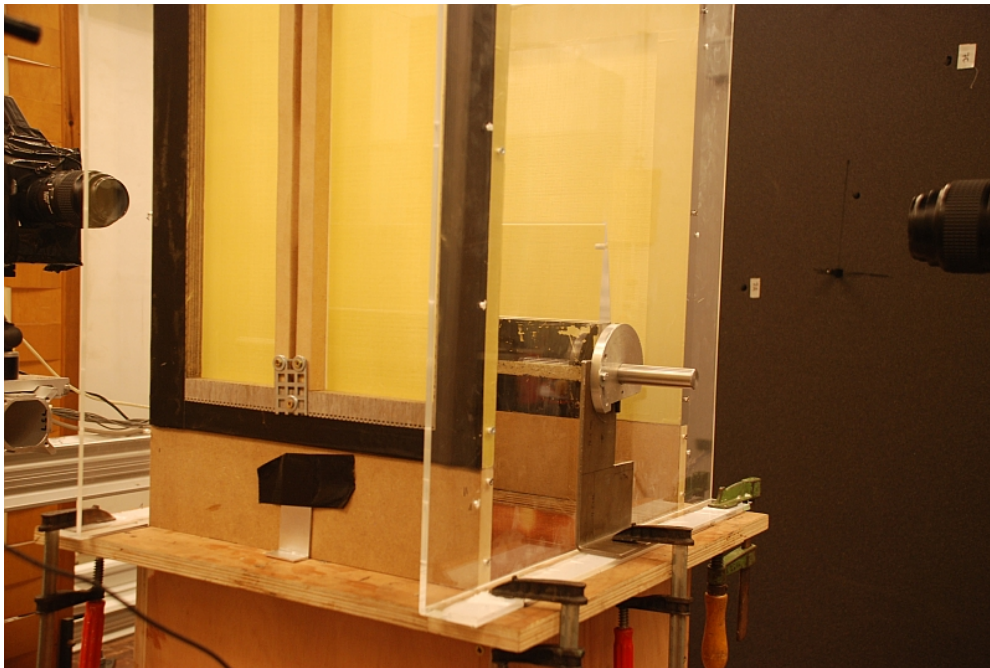


Figure 4.6: Photograph of the set-up showing the camera positions and the far-field microphones

Flow Velocity, V m/s	20 ($Re_c = 0.27$ million), 30 ($Re_c = 0.4$ million)
Angle of attack, α	$4^\circ, 8^\circ$
Field of View, FOV	$50 \times 50mm^2$ each camera
Sensor size	512×512 pixels
Magnification, M	0.21
Focal length, f	105 mm in both cameras
Numerical aperture, $f_\#$	2.8 in both cameras
PIV acquisition frequency, f_s	5 kHz, 8 kHz
Pulse separation, dt	40, 25 μs
Recording mode	Double frame
Number of images, N	10000

Table 4.2: Simultaneous, synchronized measurements: 2C-PIV recording and flow parameters

4.4 Stereo PIV set-up

In order to understand the spanwise correlation of the flow structures stereoscopic measurements are carried out on a plane perpendicular to freestream in the downstream direction for the GF 6% case. The measurement plane is at distance of $x/h=1$ downstream that is selected in the region of maximum v component rms value based on the Planar PIV results of the first campaign. The experimental set up is shown in Figure 4.8. Figure 4.8 shows the calibration done using Type 10 plate. Two cameras using 200mm lenses are placed at an angle of almost 90° . Scheimpflug adapters (to tilt the lenses) are used to align the focal with the object plane. Images are recorded in double frame mode with the same acquisition frequencies as in planar PIV. Table 4.3 shows the flow and PIV recording parameters.

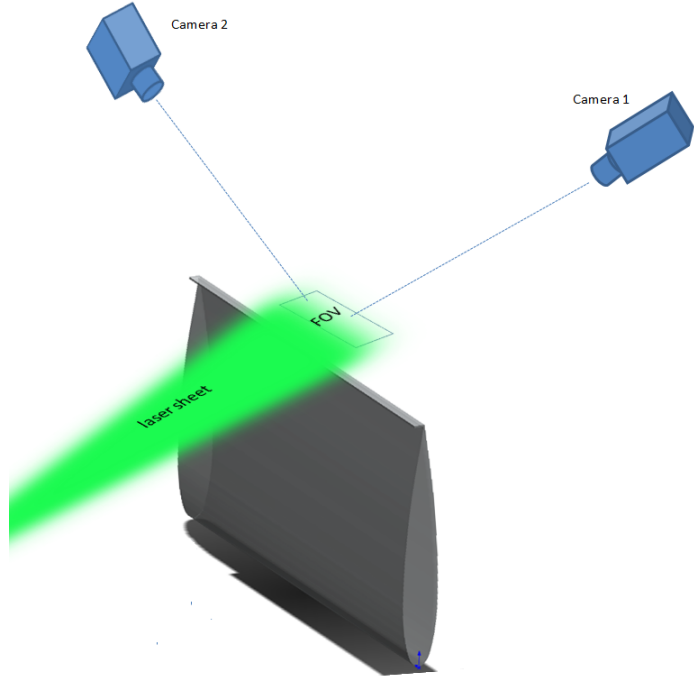
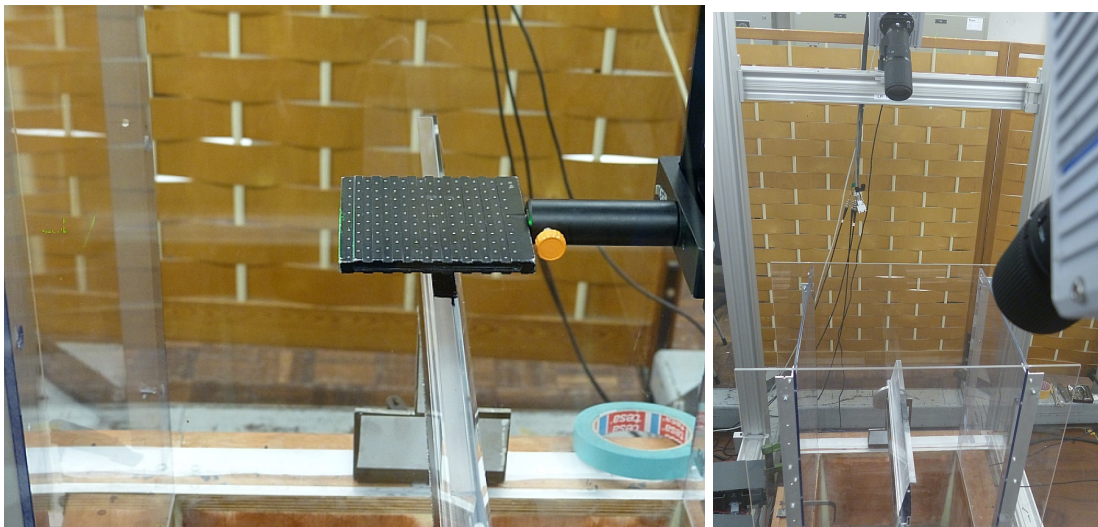


Figure 4.7: Schematic diagram for the Stereoscopic measurements



(a) Measurement plane shown by the calibration plate

(b) Camera Positions

Figure 4.8: Photograph of the stereoscopic PIV set-up

Flow Velocity, V m/s	20 ($Re_c = 0.27$ million), 30 ($Re_c = 0.4$ million)
Angle of attack, α	$4^\circ, 8^\circ$
Field of View, FOV	$75 \times 75 mm^2$
Sensor size	1024×1024 pixels
Magnification, M	0.16
Focal length, f	200 mm in both cameras
Numerical aperture, $f_\#$	4, 5.6
PIV acquisition frequency, f_s	5 kHz, 8 kHz
Pulse separation, dt	25, 15 μs
Recording mode	Double frame
Number of images, N	4157

Table 4.3: Stereoscopic Measurements: 3C-2D PIV recording and flow parameters

4.5 Microphone Measurements

The far-field acoustic fluctuations are measured using LinearX M51 microphones. The microphones are connected to a data acquisition module NI 9234 which in turn is connected to a PC running LabVIEW as a user interface. Measurements are acquired at 40 KHz. The number of samples collected are 200,000. The measurements are carried out simultaneously and synchronised with the planar PIV recordings. Two microphones are placed at a distance of 1.25m on the suction side and two on the pressure side at a distance of 1m. Calibration is performed using a 'piston phone' which emits waves of known frequency (250Hz) and amplitude. For the range of frequencies associated with the Gurney flap (250-450Hz) no correction for the response in amplitude is required as shown in Figure 4.9.



(a) LinearX M51 microphone

(b) Response of M51 microphone for different frequencies

Figure 4.9: Microphones used for far-field acoustic measurement

4.6 PIV image processing

Various pre/post-processing techniques available in DAVIS 8.2 are used to obtain the final velocity field shown in Figure 4.11. Pre-processing of images is carried out using the time minimum intensity subtraction to remove unwanted reflections. The vector field is evaluated by the cross correlation algorithm using multi-pass iterations with decreasing interrogation window sizes (128×128 to 16×16 , 75% overlap, 2-3 passes, round interrogation window form). Vector post-processing is carried out using the universal outlier detection algorithm. In the Planar case, the two vector fields (Figure 4.10) are then stitched together (averaging the values in the overlap region) keeping in mind the orientations of the cameras. The final vector field with FOV $85 \times 60 \text{ mm}^2$ with 10 pixels/mm resolution is shown in Figure 4.11. The processing method is similar for the stereoscopic PIV in addition to using the self-calibration option.

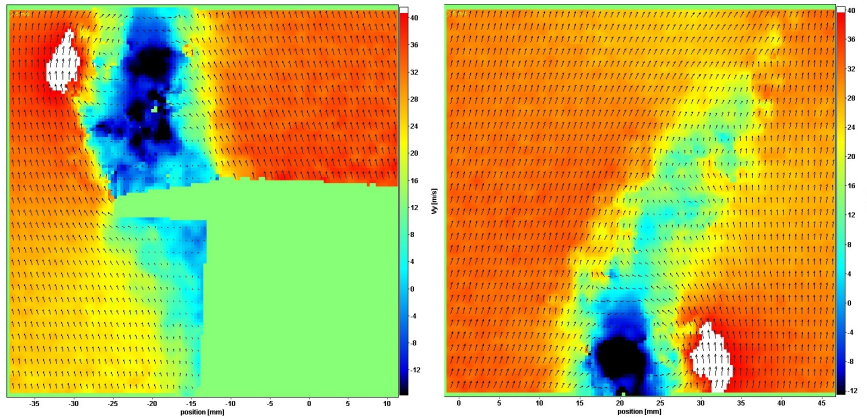


Figure 4.10: Velocity field obtained at camera 1 (left), camera 2 (right)

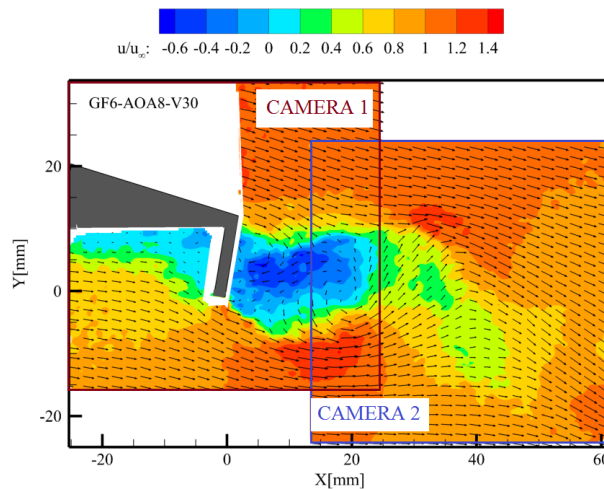


Figure 4.11: The stitched velocity field

Chapter 5

Results

Vortices are the voice of the flow.

Müller and Obermeier

This chapter presents the results of TR-PIV and acoustic experiments carried out on the Gurney flap models. Section 5.1 gives an overview of the characteristics of the boundary layer. Flow statistics of a Gurney flap in different configurations are presented in section 5.2, followed by time resolved velocity field in section 5.3. The acoustic and PIV spectra for various cases are discussed in section 5.4. Next, the results of the causality correlation, coherence applied to the Gurney flap case are presented. Finally, the spanwise correlation length of the structures are presented in section 5.8.

5.1 Characterization of the Boundary layer

As mentioned in the experimental set-up (section 4.2), a fully developed turbulent boundary layer is required to simulate the flight conditions. This is achieved by tripping the boundary layer using three dimensional roughness elements placed at $x/c = 0.25$. The statistical properties of the boundary layer help in deriving the scaling parameters and act as a reference for future experiments. The planar velocity field shown in Figure 5.1 for the 4% Gurney flap case at $\alpha = 4^\circ$, $V = 30m/s$ on the suction side is obtained after processing the PIV images as described in section 4.6. The increase in the boundary layer thickness towards the trailing edge can be observed. This is due to the presence of an adverse pressure gradient. Figure 5.2 shows the boundary layer velocity profile at $x/c = 0.97$. It can be seen that the velocity field measured decreases up to $u/u_e(x) \approx 0.55$ at $y/\delta \approx 0.1$ and not any further due to reflections at the wall (that are masked). Moreover, the presence of a high velocity gradient, very close to the wall, in a turbulent boundary layer makes measurement difficult due to the limitations on interrogation window sizes in PIV. However, few more velocity vectors near the wall can be obtained using advanced processing techniques like sum of correlation.

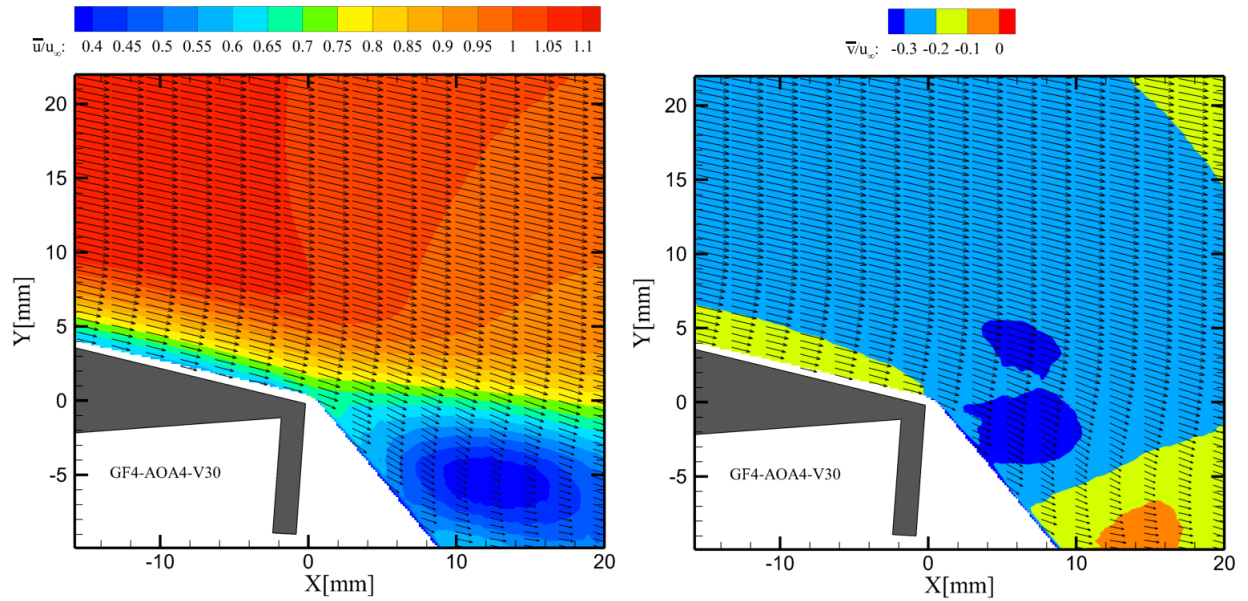


Figure 5.1: Measured Boundary layer on the suction side of GF4-AOA4-V30 (left) u component (right) v component

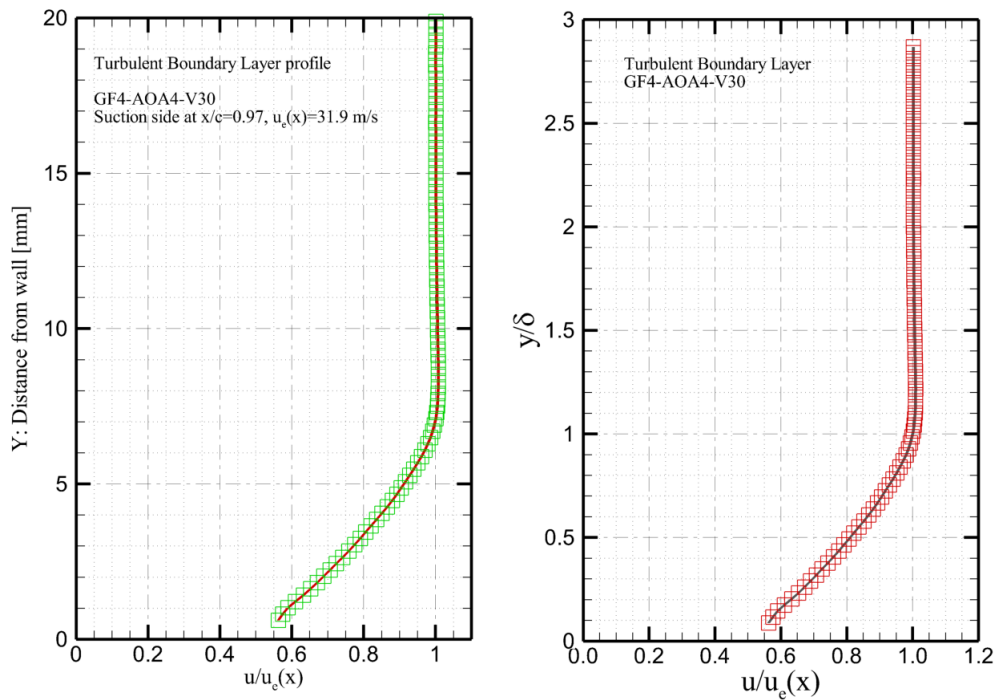


Figure 5.2: Boundary layer velocity profile at $x/c=0.97$, (left) dimensional wall distance (right) normalized with boundary layer thickness, y/δ

The boundary layer properties such as boundary layer thickness δ_{99} , boundary layer displacement thickness δ^* , momentum thickness θ and shape factor $H = \frac{\delta^*}{\theta}$ are determined from the velocity profile and shown in Table 5.1. The shape factor $H \approx 1.5$ confirms the presence of a turbulent boundary layer [76].

δ_{99} (mm)	δ_{95} (mm)	δ^* (mm)	θ (mm)	H
≈ 7	6	0.936	0.621	1.51

Table 5.1: Boundary layer properties at $x/c=0.97$

The different regions in a turbulent boundary layer have certain universal limits in terms of non-dimensional coordinates in wall-normal direction as shown in Table 5.2. The scaling parameters are defined by, $y^+ = \frac{y}{\delta_v}$, $u^+ = \frac{u}{u_\tau}$ where δ_v is the viscous wall unit ($= \frac{\nu}{u_\tau}$) and u_τ is the wall shear velocity.

Inner Layer	$\frac{y}{\delta} < 0.1$	Scaling with u_τ and y^+
Viscous sublayer	$y^+ < 5$	Reynolds stress negligible compared to viscous stress
Buffer layer	$5 < y^+ < 30$	Overlap between viscous sublayer and log-law region
Viscous wall region	$y^+ < 50$	Viscous contribution to shear stress important
Outer layer	$y^+ > 50$	Direct effects of viscosity negligible
Overlap region	$y^+ > 50$ $\frac{y}{\delta} < 0.1$	Overlap between wall and outer region
Log-law region	$y^+ > 30$ $\frac{y}{\delta} < 0.3$	Log-law

Table 5.2: Boundary layer division (Pope [77])

The Clauser plot technique is used to determine the skin friction coefficient C_f . The scaling parameters u_τ and δ_v are determined to be $1.19m/s$ and 0.0126 mm respectively. The scaled boundary layer profile is shown in Figure 5.3. Figure 5.3 shows the outer layer of the turbulent boundary layer that is measured $y^+ > 50$ (shown in red) and the possible regions where different scaling laws can be applied. The boundary layer obtained cannot be directly compared to a flat plate because of the adverse pressure gradient present at location $x/c=0.97$. The log law deviates in the outer layer to the law of the wake which has corrections like wake parameter (π) and wake function (W) that accounts for the adverse pressure gradient present at the trailing edge of the airfoil. The inner layer shown in blue is drawn for completeness and is not accurate.

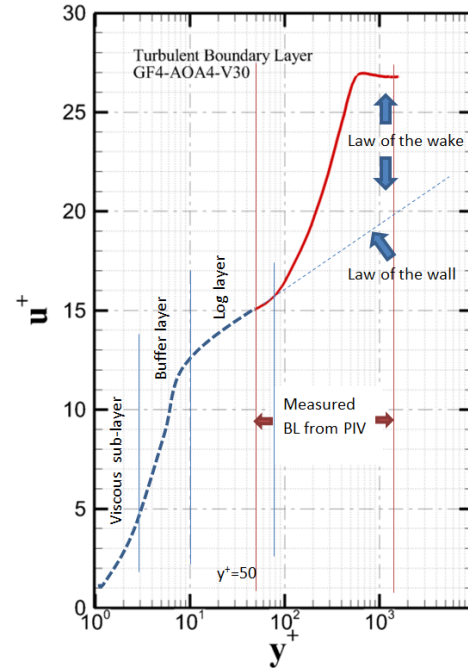


Figure 5.3: A typical turbulent boundary layer profile (blue-not measured), (red-measured using PIV)

5.2 Flow Statistics

The GF6-AOA8-V30 (Gurney flap size: 6%, $\alpha : 8^\circ$, $U_\infty : 30m/s$) is a case that is at the focal point throughout the thesis to understand the noise sources in Gurney flaps using the causality correlation approach. The contours of time averaged velocity component \bar{u} , \bar{v} along with the root-mean-square of the fluctuations u'_{rms} , v'_{rms} for this case is shown in Figure 5.4 (normalized with U_∞). The contour plot of v'_{rms} (values larger than u'_{rms}) is of particular interest as the radiated sound associated with the unsteady lift can be directly linked to the unsteady vertical velocity component in the wake section 2.2(Acoustic Analogies). It should be noted that v'_{rms} is used as a normalizing factor while correlating v' with far-field pressure fluctuation p' measured using a microphone.

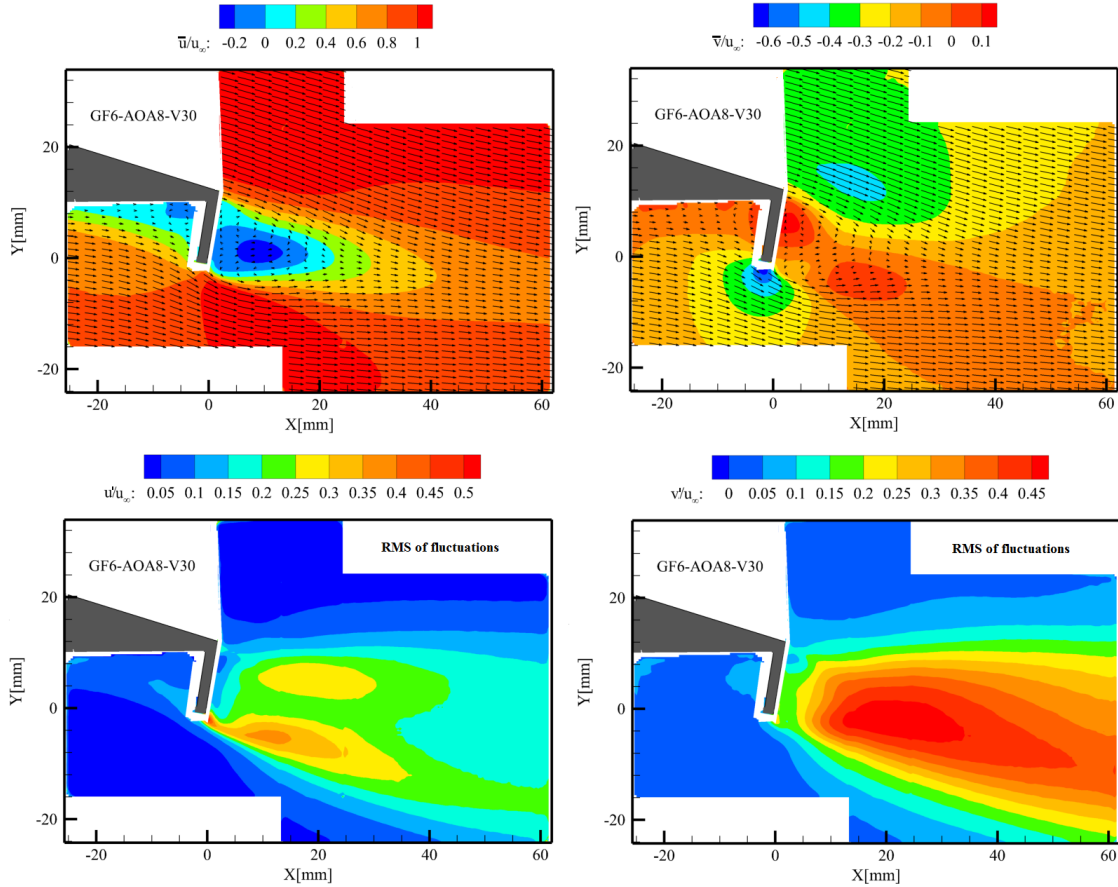


Figure 5.4: Flow statistics for GF6-AOA8-V30, \bar{u} (top left), \bar{v} (top right), u'_{rms} (bottom left) v'_{rms} (bottom right) at $Re_c = 0.4$ million

The \bar{u} contour plot shows, as expected, the stream wise velocity component on the suction side to be higher compared to the pressure side. The contour plot also distinguishes the three main regions in the flow as found in previous literature explained in section 2.1 (Flow Structure). First, an upstream separation of the flow on the pressure side (due to the flap geometry) creating a separation bubble/recirculation region (light blue) is found at (X:-5,Y:8). Second, the upper and the lower separating shear layers can also be clearly seen. Finally, the main recirculation region (dark blue),

downstream of the flap is found from X: 0 to 20, Y: -4 to 12. This recirculation region is approximately the size of the flap. The movement of the stagnation point downstream, the upstream separation bubble and a pair of counter rotating vortices found by Liebeck [29] and others can be clearly seen when streamlines are drawn on the mean velocity field as shown in Figure 5.5. The presence of the flap also causes a large downward motion of the lower shear layer, compared to the upper shear layer as shown in the \bar{v} contour plot. The von Kármán vortex shedding causes large fluctuations in the wake as seen clearly from v'_{rms} . The maximum value in the contour map of v'_{rms} is located in the vicinity of X:20 ($x/c=0.1$), this corresponds to the region where the upper and lower shear layers interact, shedding opposite vortices that are rapidly accelerated (also found by Henning *et al.* in the cylinder wake case). Due to the flapping motion of the von Kármán wake (in detail in section 5.3) that includes the lower and upper shear layers, a non-zero value of RMS is found (in light blue) close to the flap in v'_{rms} and u'_{rms} contour plots.

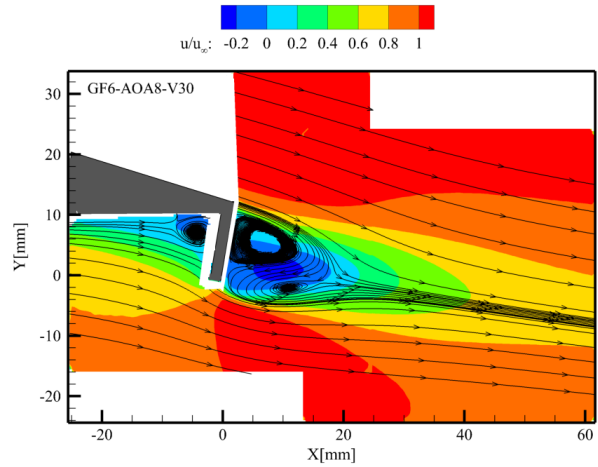


Figure 5.5: GF6-AOA8-V30: Streamlines

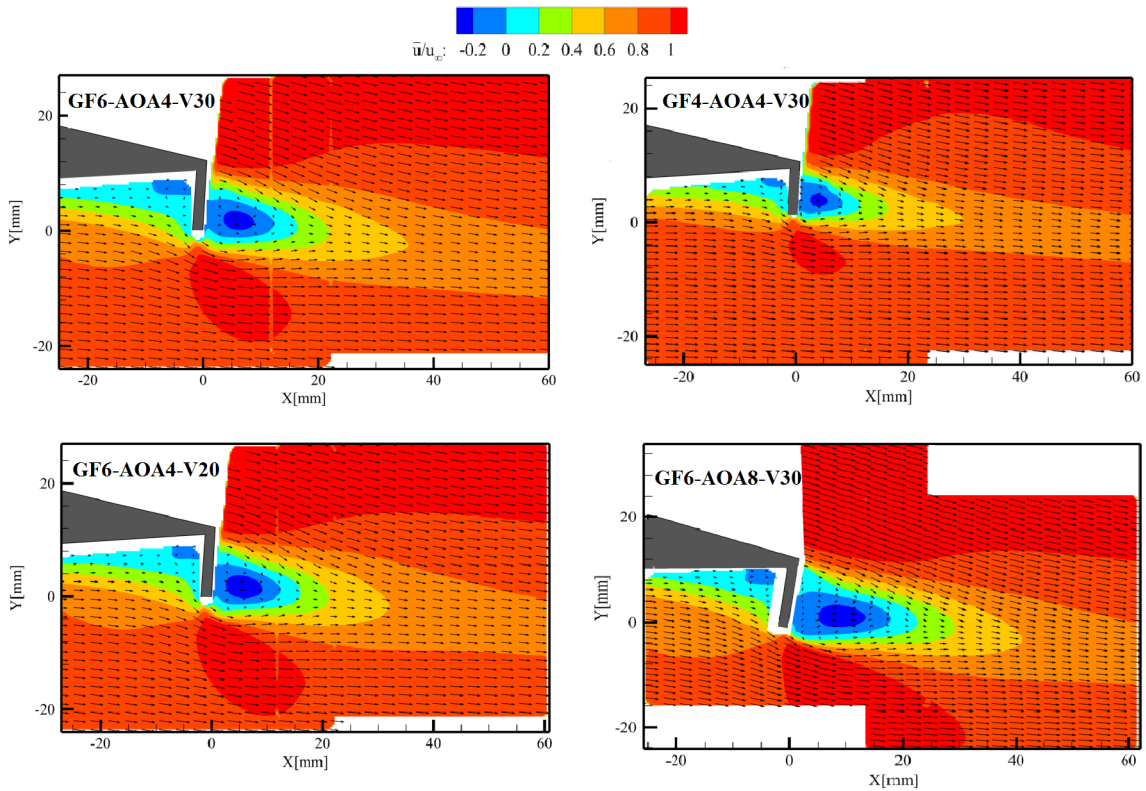


Figure 5.6: Time averaged velocity field: \bar{u} for different cases (top left, top right: GF% decrease; top left, bottom left: Re decrease; top left, bottom right: α increase)

The effect of change in Re , α and GF % size on \bar{u} is shown in Figure 5.6. The contour plots (top left, bottom left) show that a change in Reynolds number has almost no effect on the upstream separation bubble and the downstream recirculation region. However, decreasing the Gurney flap size (top left, top right) causes, as expected, the recirculation region to decrease in size confirming that it scales with the flap size. The upstream separation point in the lower shear layer also moves aft. Increasing the angle of attack (top left, bottom right) increases the size of the downstream recirculation region. This can be attributed to the increase in the vertical distance between the separating shear layers due to a higher angle of attack.

Similar contour plots for v'_{rms} and u'_{rms} are shown in Figure 5.7 and Figure 5.8 respectively. The regions of higher v'_{rms} and u'_{rms} in the wake are slightly smaller when Re is decreased. Increasing the angle of attack leads to a decrease in v'_{rms} and u'_{rms} in the wake. This is related to a reduction in symmetry between the suction and pressure side at higher α reduces the strength of vortex shedding thereby decreasing the v' fluctuations in the wake.

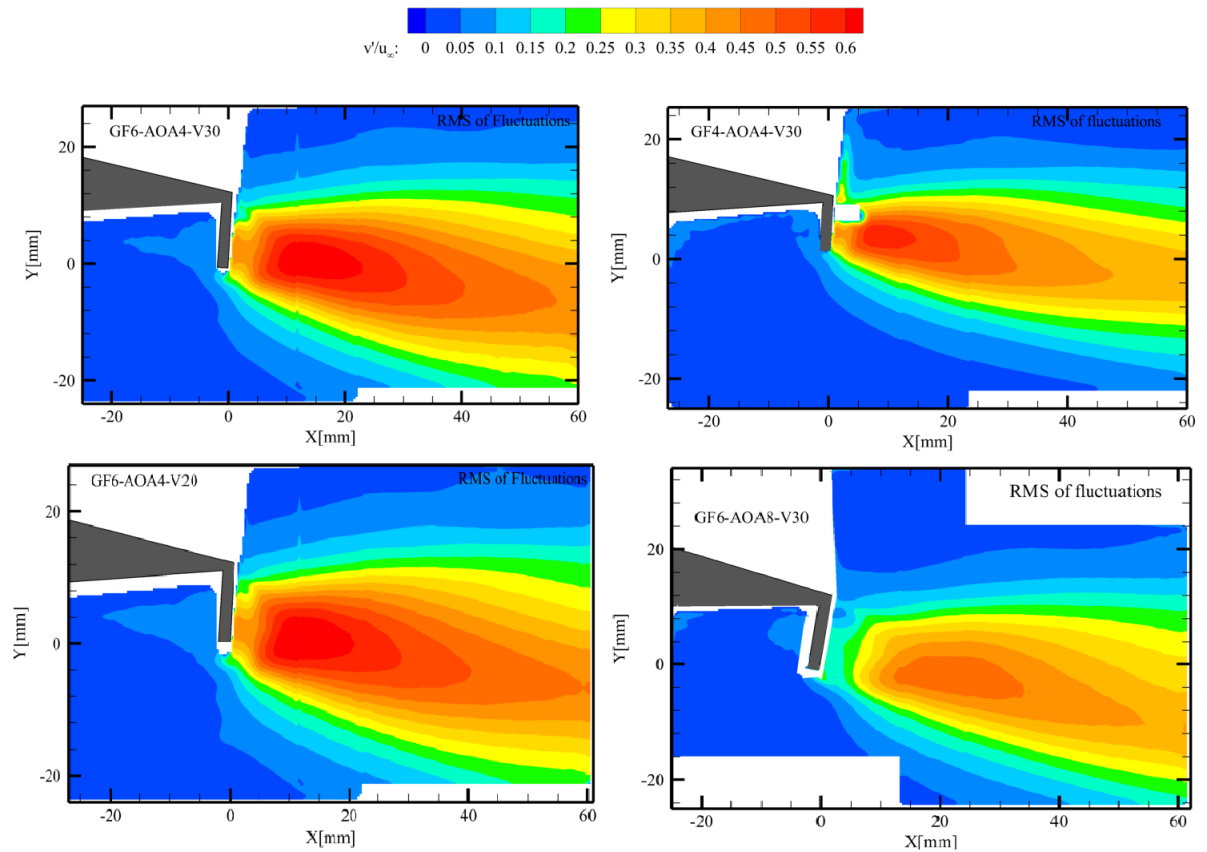


Figure 5.7: RMS velocity field: v'_{rms} for different cases (top left, top right: GF% decrease; top left, bottom left: Re decrease; top left, bottom right: α increase)

High values of u'_{rms} for various cases (Figure 5.8) can be seen in the two separating shear layers. These values are higher in the lower shear layer as compared to the upper shear layer.

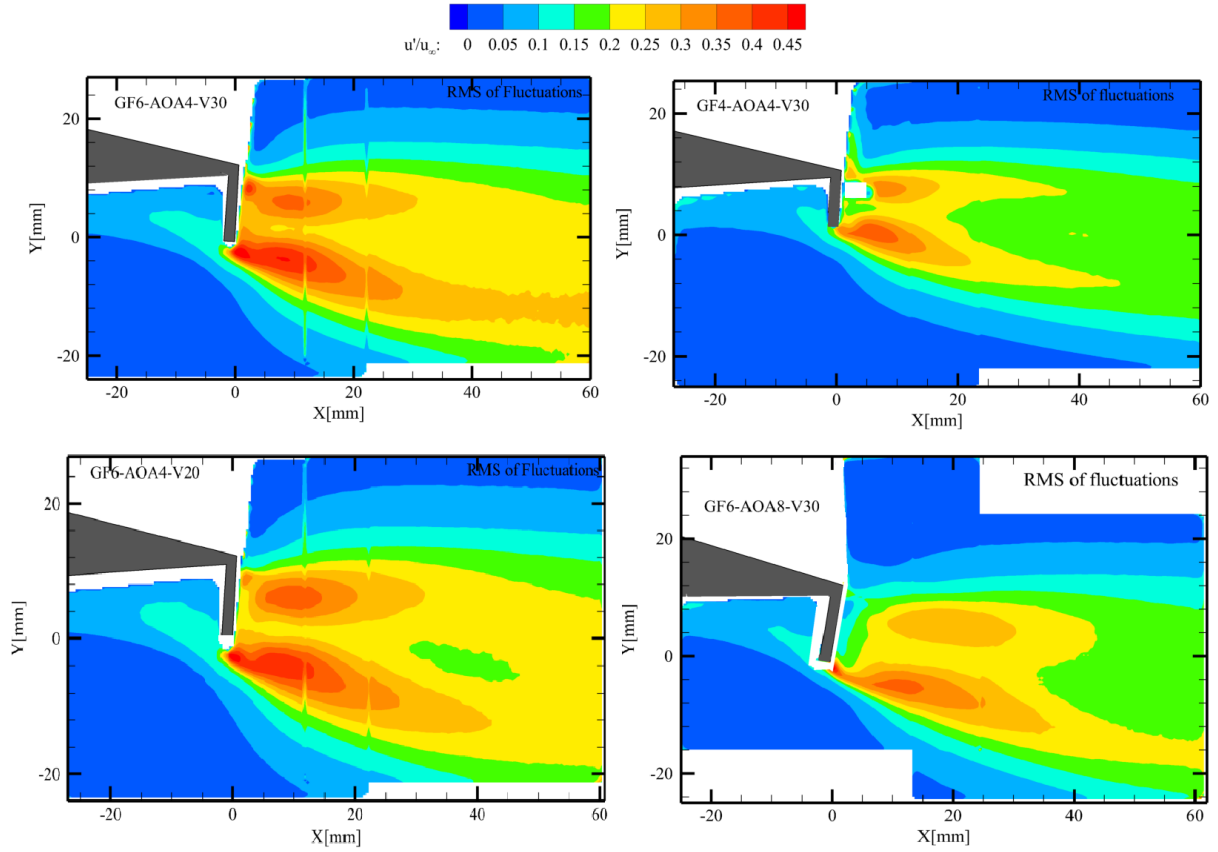


Figure 5.8: RMS velocity field: u'_{rms} for different cases (top left, top right: GF% decrease; top left, bottom left: Re decrease; top left, bottom right: α increase)

5.3 Flow dynamics: Time Resolved

The time resolved velocity field for the GF6-AOA8-V30 case is shown in Figure 5.9 (u) and Figure 5.10 (v). The data for this case is obtained with a PIV acquisition frequency of 8 kHz. As the maximum frequency of shedding for GF 6% is around 500 Hz ($St=0.2$ based on Gurney flap height) we have 16 velocity fields per period, thereby resolving the temporal features of the flow field rather well. One in five snapshots are shown in the figures. The contours of instantaneous streamwise velocity component u shows the flapping motion of the von Kármán wake. The large scale structures seen from the contours of instantaneous vertical velocity component v represent the kármán vortex shedding process. The letters A and B indicate the downstream convection of these large scale structures. As explained in section 2.1(Flow Structure), the von Kármán vortex street occurs when two separating shear layers interact. The upper and lower boundary layers having opposite vorticity

form two separating shear layers. When one of the shear layers rolls up and forms a vortex, the other shear layer cuts off the vorticity supply thereby shedding a vortex in the process.

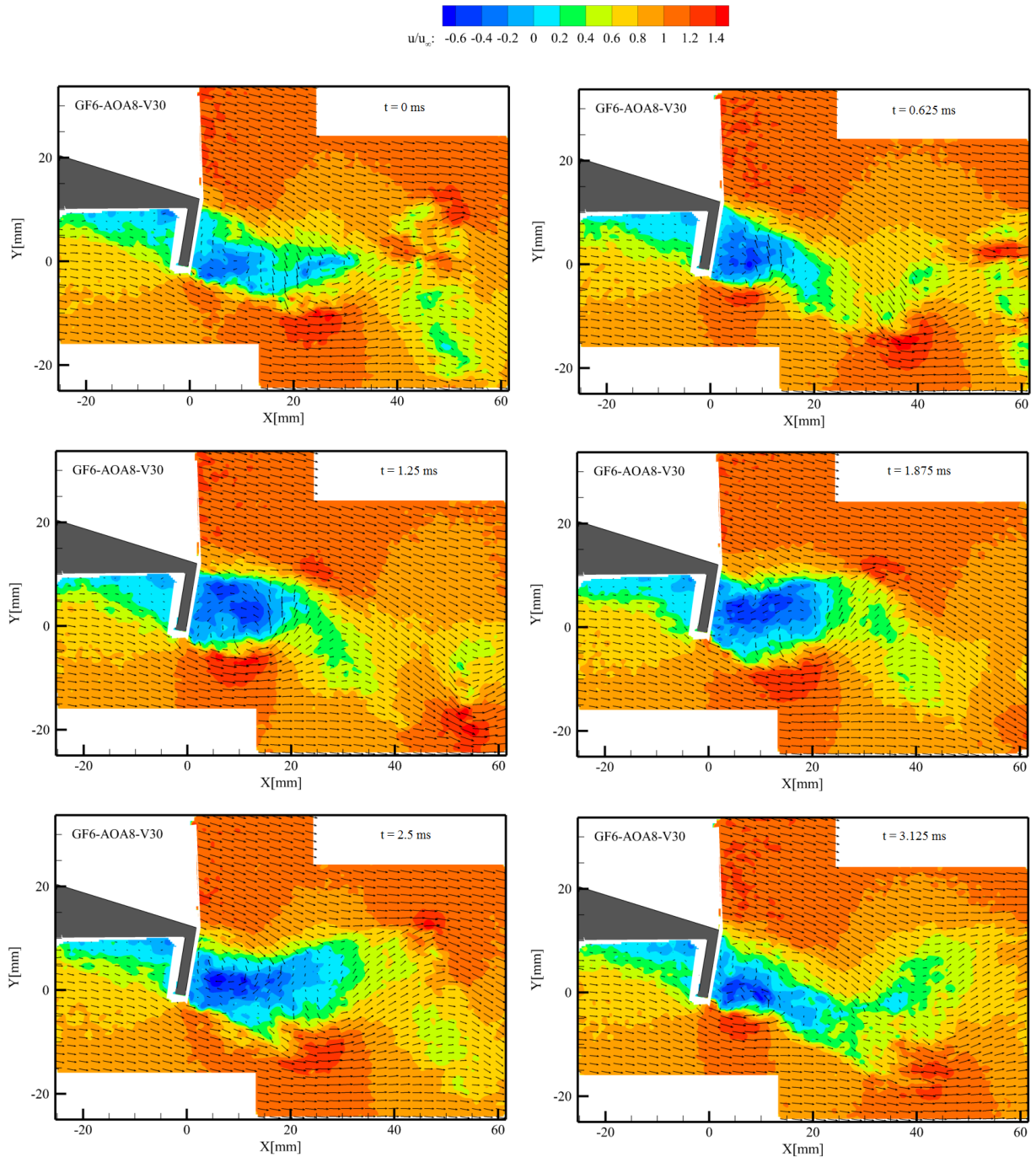


Figure 5.9: Instantaneous u component at different time instants: GF6-AOA8-V30 at $Re_c = 0.4$ million

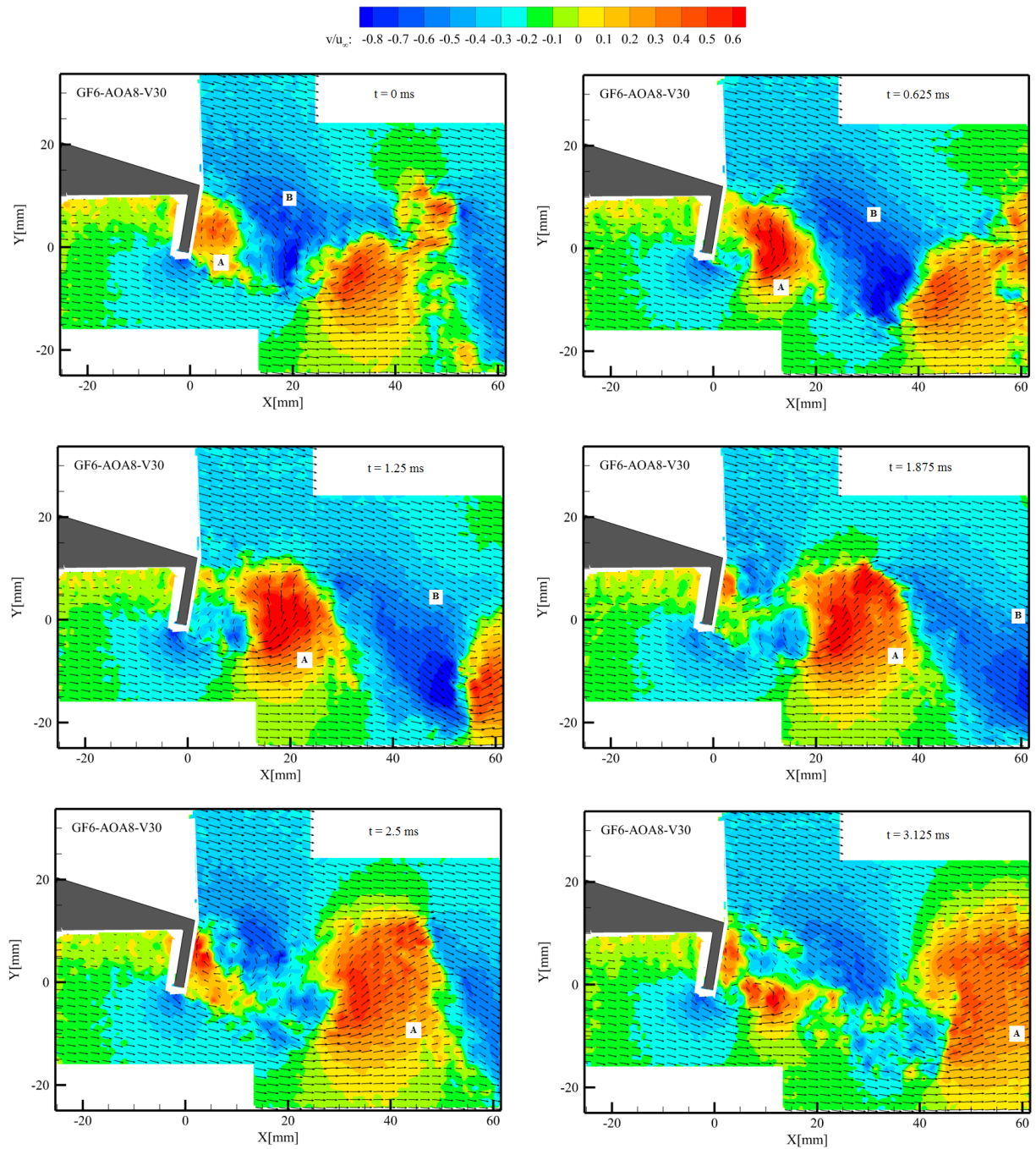


Figure 5.10: Instantaneous v component at different time instants: GF6-AOA8-V30 at $Re_c = 0.4$ million

The instantaneous vorticity obtained from time-resolved velocity fields is computed and shown in Figure 5.11. The *vortex roll up process* can be seen as vorticity is shed by both the upper and

lower boundary layers due to the disappearing normal velocity boundary condition. Positive vorticity (counterclockwise direction of the fluid) shed from the lower and negative vorticity shed by the upper boundary layer is seen interacting in the downstream of the flap leading to periodic vortex shedding.

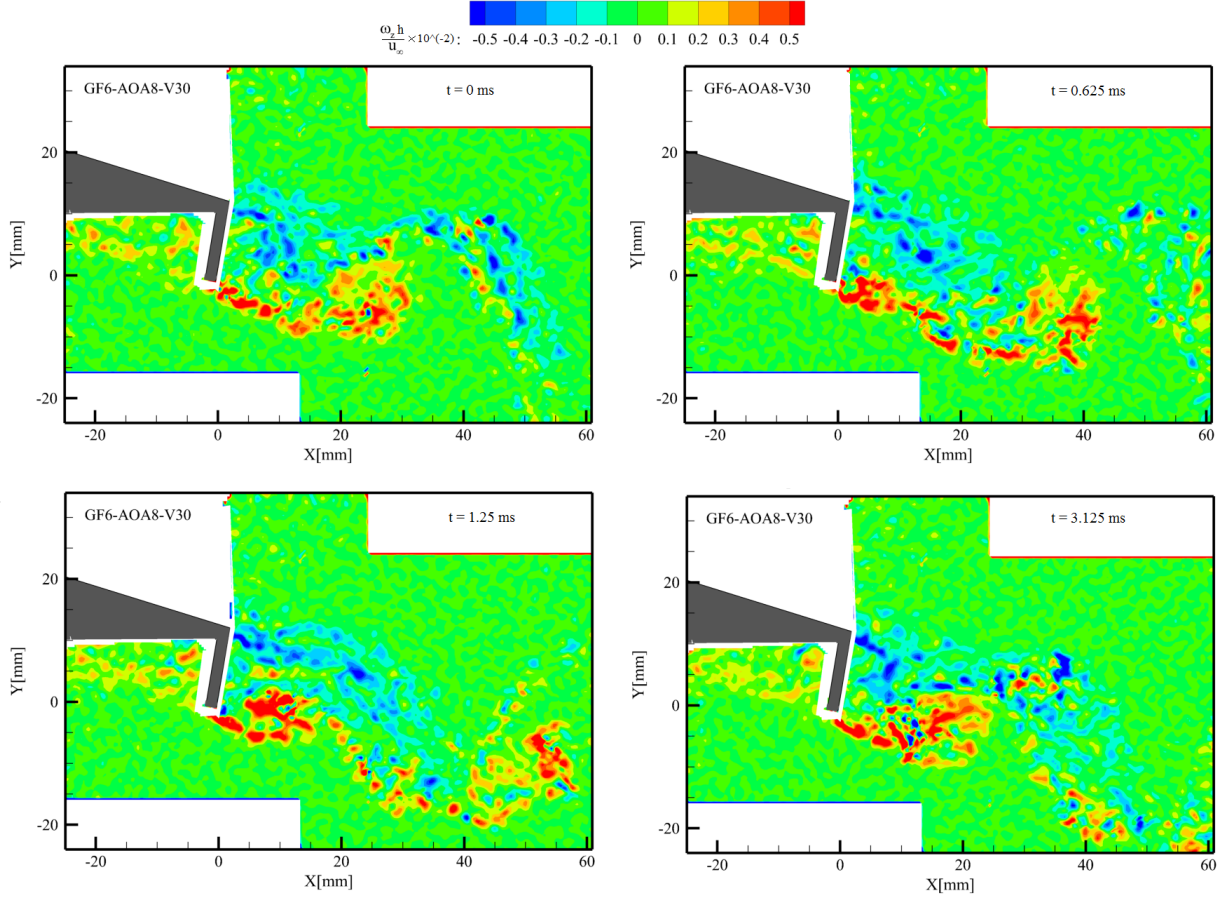


Figure 5.11: Instantaneous ω_z component at different time instants: GF6-AOA8-V30 at $Re_c = 0.4$ million

The instantaneous component of the Lamb vector $\boldsymbol{\omega} \times \mathbf{v}$ (as explained in vortex sound theory) is calculated for the Planar PIV case ($\omega_x, \omega_y, \omega = 0$). As v' fluctuations are larger (than u') and responsible for the unsteady lift, the x-component of the Lamb vector $L_x = -\omega_z v$ is more relevant as shown in Figure 5.12.

$$\boldsymbol{\omega} \times \mathbf{v} = \begin{vmatrix} i & j & k \\ 0 & 0 & \omega_z \\ u & v & 0 \end{vmatrix} = -i(\omega_z v) + j(\omega_z u) \quad (5.1)$$

The frequency of the vortex shedding depends on the vertical separation of these shear layers

as well as on the thickness of the incoming turbulent boundary layer, which in turn depend on Re , $GF\%$ and angle of attack. This is discussed in the next section.

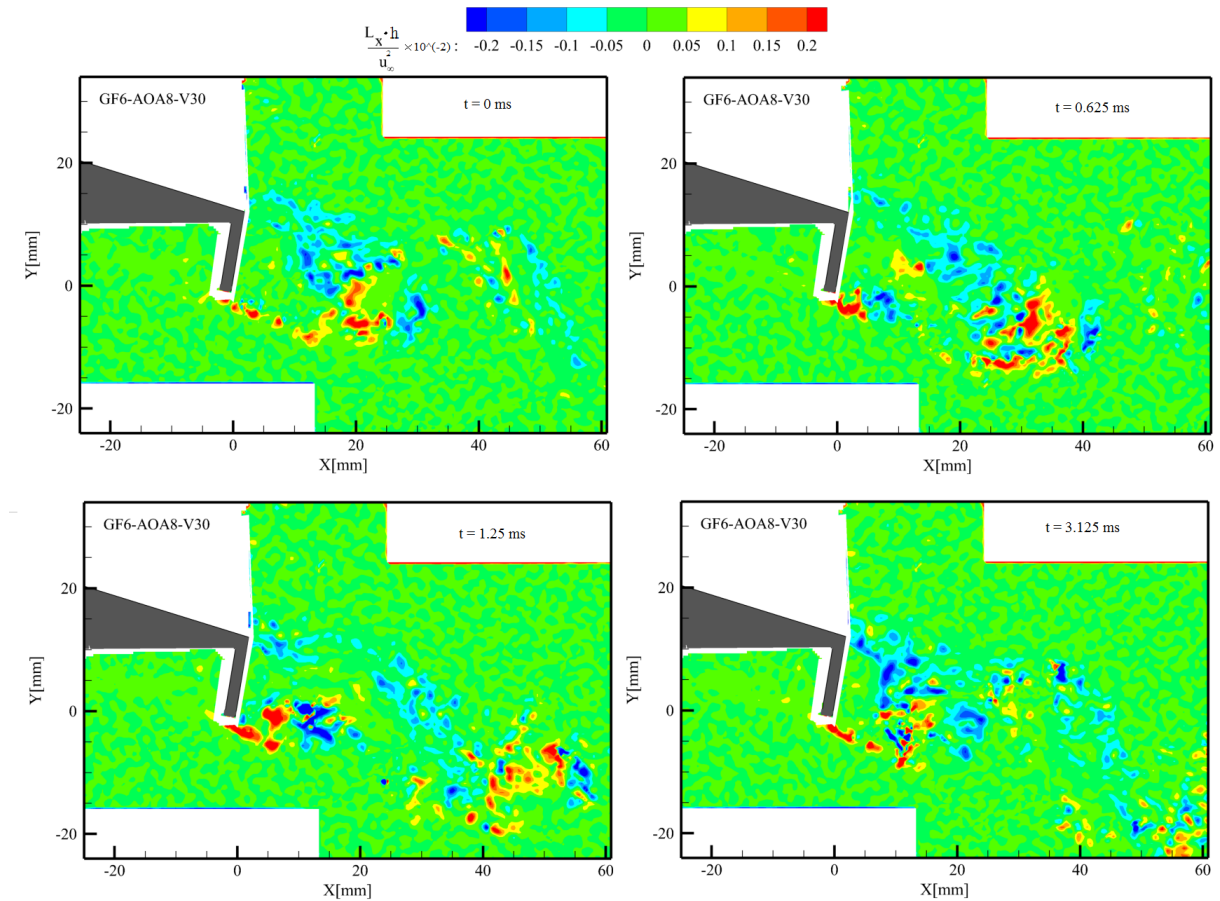


Figure 5.12: Instantaneous L_x component at different time instants: GF6-AOA8-V30 at $Re_c 0.4$ million

The next page contains videos of all the time-resolved quantities discussed above and can be played in the pdf version available online (<http://repository.tudelft.nl/>).

5.4 Power Spectral Density

Flow: TR-PIV

The PSD of a time varying signal represents the way energy is distributed in the frequency domain. The power spectrum for the v component (after taking $20\log_{10}$) at (X,Y) locations A, B and C as shown in Figure 5.13 is calculated with a frequency resolution of 10 Hz by the method described in section 3.4. Figure 5.14 shows the primary vortex shedding frequency $f_s = 450\text{Hz}$ ($St=0.18$ based on flap height) and its harmonics. The presence of a secondary mode of shedding of lower frequency (at location A) due to fluid recirculating the upstream separation bubble and subsequently ejecting downstream as observed previously by Troolin *et al.*[32], section 2.1 is however not present. The GF6-AOA8-V30 case is chosen as previously the second mode of shedding became more coherent as the angle of attack increases (Figure 2.10). The absence of a second mode for this case may be attributed to a higher Reynolds number and/or the presence of a turbulent boundary layer.

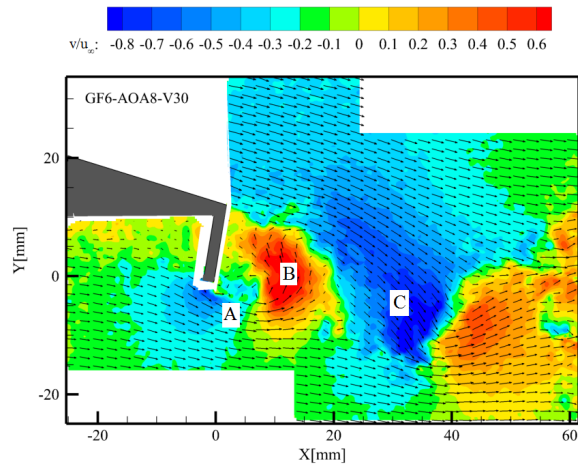


Figure 5.13: GF6-AOA8-V30: v component, A, B and C are locations where PSD is calculated

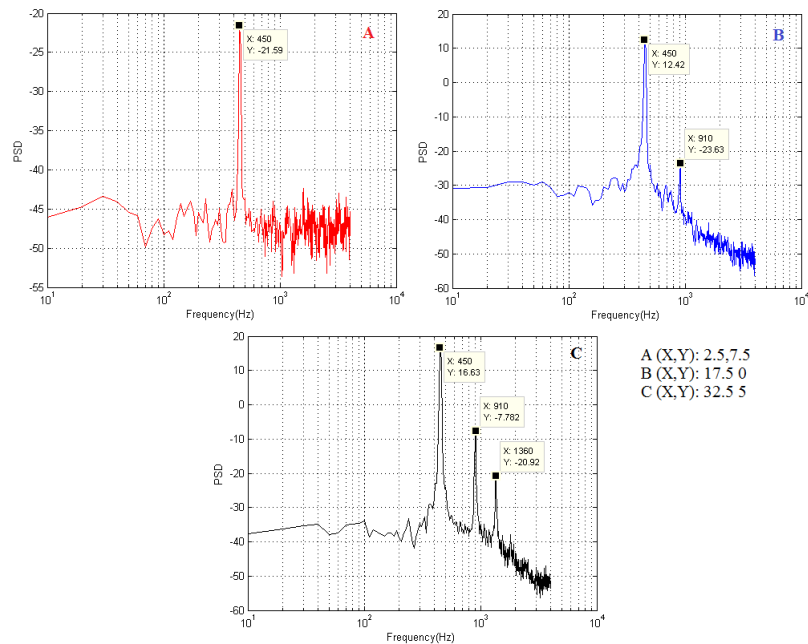


Figure 5.14: PSD v component: GF6-AOA8-V30; The amplitude of the power spectrum calculated here is not scaled, the plots are mainly to show different frequencies

Acoustics: Microphone

The power spectrum computed as explained in section 3.4 from the far-field pressure fluctuations of the microphone (on the suction side) is computed for different angles of attack, Reynolds number and Gurney flap sizes (Figure 5.15, frequency resolution 10Hz). The blue and red spectra are obtained with acquisition frequency set to 40kHz, using a data acquisition module NI 9215. While the green spectrum had a newer data acquisition module NI 9234 with acquisition frequency of 51.2kHz (which can be set to only multiples of 51.2). The newer NI 9234 module has a higher signal-to-noise ratio while the older NI 9215 has a constant noise level at higher frequencies (blue and red spectra). The tonal peaks in the Figure 5.15 were clearly audible during the experiments and correspond to the coherent periodic shedding observed in the flow. The SPL amplitudes as expected increases with velocity and GF % size but are almost equal for different α . The frequency of the tone match to that of the vortex shedding frequency (more in the next section).

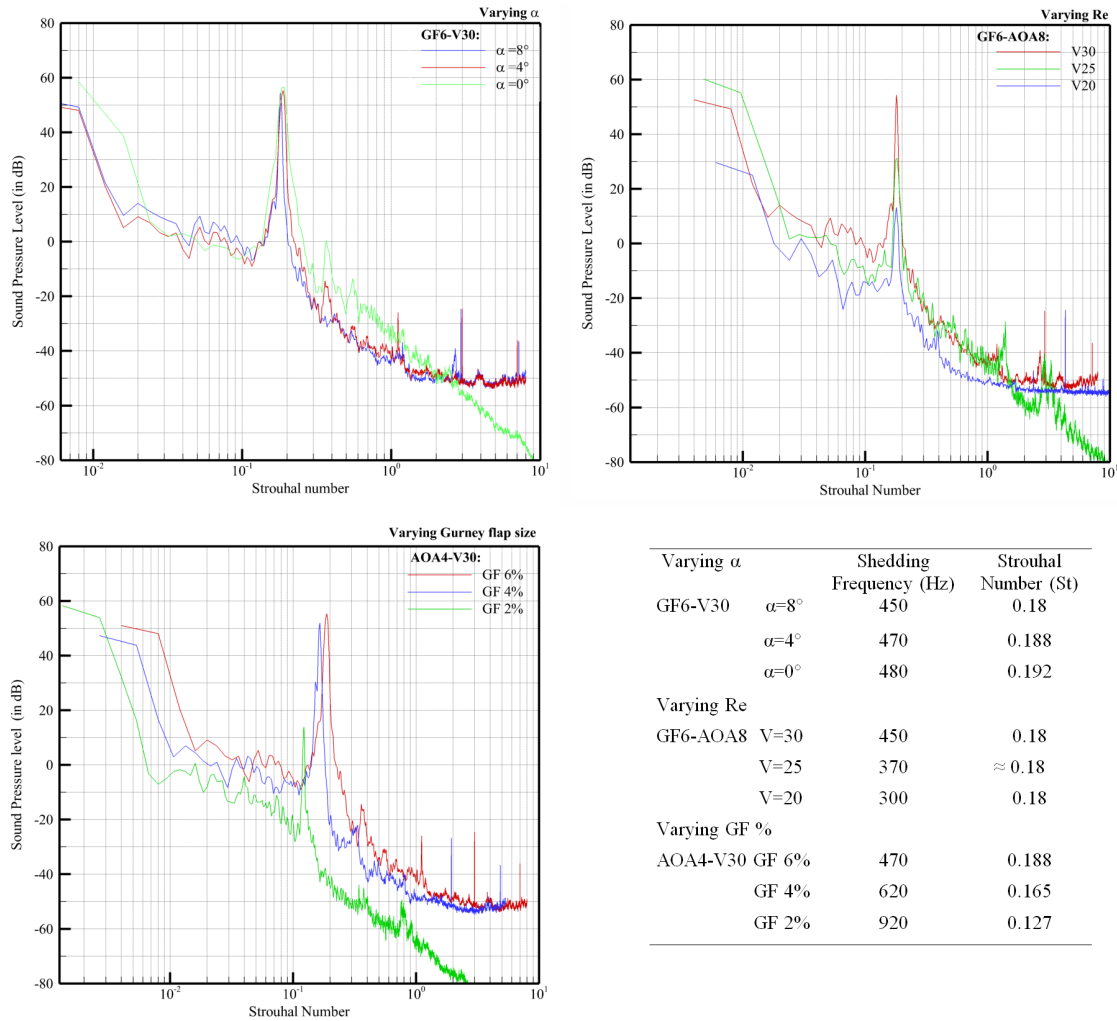


Figure 5.15: Power spectrum of far-field pressure fluctuations measured on the suction side microphone: Varying α , Varying Re , Varying GF % Size and Sheddng frequency/St values

Figure 5.15 also shows the trend in shedding frequencies and corresponding Strouhal numbers. Strouhal number remains almost constant for different Re. It decreases with an increase in angle of attack due to an increase in boundary layer thickness (Jeffery *et al.* Troolin *et al.*). With decreasing flap sizes the frequency increases and Strouhal number decreases due to the decreasing vertical distance between the two separating shear layers. The Strouhal numbers calculated with respect to the distance between the shear layers (from Figure 5.8, the distance between maximum u_{rms} in shear layers) are found to be closer as shown in Table 5.3.

Case	f (Hz)	St	Separation distance (m)	St_{shear}
GF4-AOA4-V30	620	0.165	0.011	0.227
GF6-AOA4-V30	470	0.188	0.015	0.235

Table 5.3: Strouhal numbers calculated using the distance between the shear layers

In order to further investigate the two modes of shedding observed by Troolin *et al.* an exhaustive list of power spectra are calculated for various Reynolds numbers ($V=20$ m/s and $V=10$ m/s represent cases with almost similar Re as Troolin *et al.*) and the peaks corresponding to their shedding frequency are shown in Figure 5.16. No second peak apart from harmonics of the von Kármán shedding frequency were observed in the acoustic spectra.

			Shedding Frequency (Hz)	Strouhal Number (St)			Shedding Frequency (Hz)	Strouhal Number (St)	
GF6	$\alpha=8^\circ$	V=30	450	0.18	GF4	$\alpha=8^\circ$	V=30	570	0.154
		V=20	300	0.18			V=20	380	0.152
		V=10	130	0.156			V=10	330	0.264
GF6	$\alpha=4^\circ$	V=30	470	0.188	GF4	$\alpha=4^\circ$	V=30	620	0.165
		V=20	310	0.186			V=20	410	0.164
		V=10	150	0.18			V=10	200	0.16
GF6	$\alpha=0^\circ$	V=30	480	0.192	GF4	$\alpha=0^\circ$	V=30	620	0.165
		V=20	310	0.186			V=20	400	0.16
		V=10	160	0.192			V=10	200	0.16

			Shedding Frequency (Hz)	Strouhal Number (St)
GF2	$\alpha=8^\circ$	V=30	300	0.12
		V=20	---	---
		V=10	---	---
GF2	$\alpha=4^\circ$	V=30	920	0.122
		V=20	610	0.122
		V=10	300	0.12
GF2	$\alpha=0^\circ$	V=30	920	0.122
		V=20	620	0.124
		V=10	300	0.12

Figure 5.16: Values of primary von Kármán shedding frequency and corresponding Strouhal number of far-field pressure fluctuations measured on the suction side microphone

TR-PIV and Acoustics spectra

A comparison of the PSD obtained from the v' fluctuations and the far-field microphone (SPL in dB) shows the same shedding peak $f=450$ Hz as seen in Figure 5.17. Hence, the acoustic tone produced can be attributed to the coherent vortex shedding process. In the thesis mainly *the tonal component* of the spectra is considered and not the broadband component which is the more noisy part.

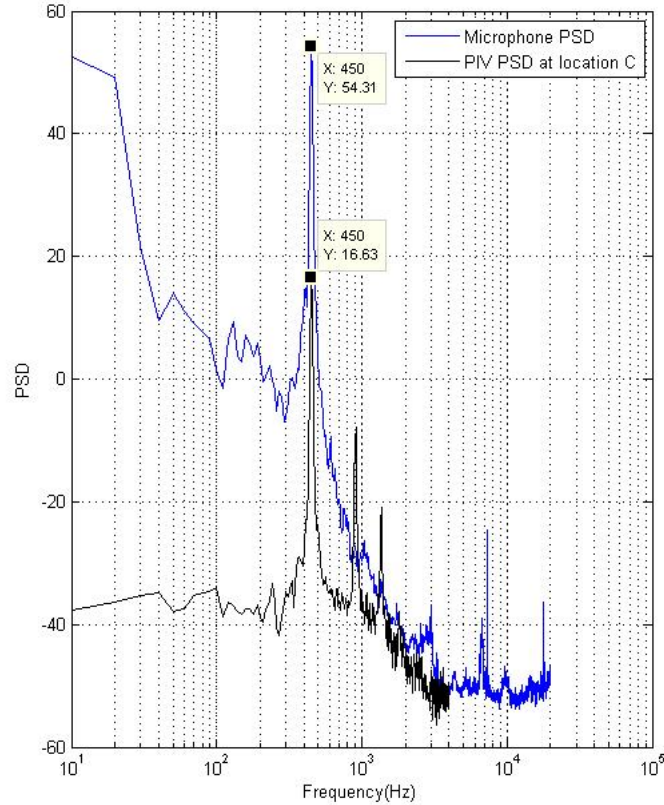


Figure 5.17: Frequency peak of PIV and microphone for the GF6-AOA8-V30 case at position C

The Strouhal numbers obtained in Gurney flap cases ($St:0.18-0.22$) are similar to that obtained for a bluff body. For example, a cylinder in a flow ($St=0.186$, Henning *et al.* [60]) or trailing edge bluntness noise when the bluntness parameter $T/\delta^* > 3.3$ (Pröbsting [78]) also leads to a tonal noise with $St \approx 0.21$. The large scale vortex shedding over the region of recirculating flow is seen in all the cases.

The PSD results in this section indicate that no second peak due to the ejecting of fluid in the upstream recirculation region is present in case of a fully developed turbulent boundary layer on both the suction and the pressure side. The second mode obtained by Troolin *et al.* is most likely due to the presence of a laminar boundary layer especially on the pressure side where the Gurney flap is located. The difference can also be due to slightly lower Reynolds number in the case of Troolin *et al.* ($Re_c:0.2$ million, $Re_c:0.1$ million) compared to the thesis ($Re_c:0.4$ million V30 case, $Re_c:0.26$ million V20). Next, proper orthogonal decomposition is used on the time-resolved velocity field to be sure that no second mode of shedding exists.

5.5 Proper Orthogonal Decomposition

The basic principle of POD was explained in section 3.4. In the thesis the results for the POD are obtained using POD decomposition algorithm available in DAVIS 8.2. POD is calculated on the time resolved velocity field for the GF6-AOA8-V30 case using all $N=10000$ images for better statistical convergence.

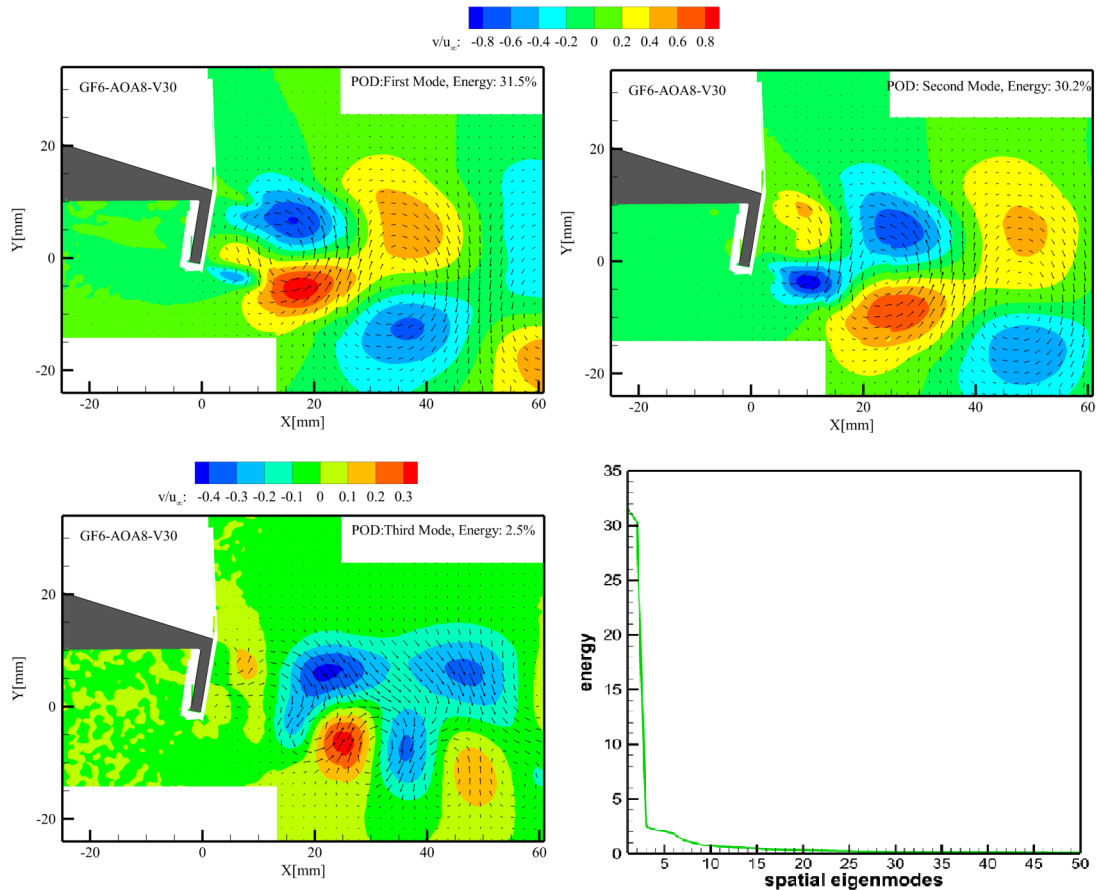


Figure 5.18: Shape of the first, second and third POD modes along with the distribution energy, (A scaling for the velocity fields is applied), $Re_c = 0.4$ million

Figure 5.18 shows the first three modes of POD of the downwash component v . The first and the second POD mode indicate a large scale vortex structures and their convection. The total energy of the first two modes is as high as 62% indicating the shedding to be periodic. The third mode with energy of 2.5% indicates the flapping motion of the wake. The total energy of the first three modes is about 65%. A second mode of shedding is also absent in the POD.

Therefore, it can be safely concluded that two modes of shedding is not the mechanism for a Gurney flap to increase lift. Other mechanisms namely increased suction on the upper side and increased pressure on the lower surface along with a “more” downward turning of the flow (increase in camber) are more likely the reasons for additional lift a Gurney flap produces.

5.6 Causality Correlation

This section describes the results obtained using the causality correlation technique which relates the basic source mechanisms ‘cause’ to the radiated sound in the far-field ‘effect’. The motivation for computing the correlation between near field fluctuations and the far-field fluctuations was explained in section 3.3. Section 3.4 discussed mathematical definition of correlation. The results discussed in this section are mainly from the *simultaneous* synchronised measurement of the flow and acoustics carried out during the second experimental campaign. The cross correlation is calculated by the FFT method (taking the inverse Fourier transform of the product of FFT of one signal and the conjugate of the FFT of the other signal). Computing the cross correlation of two signals needs the signals to be acquired at the same frequency. The acquisition frequencies and the number of samples for PIV (for example, V30 is at 8kHz, Number of images N=10000) and for acoustics (microphone 40kHz, N=800000) are different, however fortunately the acquisition frequency of the microphone signal is kept as a multiple of the PIV acquisition frequency, and is thus sampled at the frequency of PIV. Therefore, no interpolation of the microphone signal at the time instants of PIV is needed. Since the two signals are of different lengths, the normalizations needed for the cross correlation function is obtained by zero padding the fluctuations obtained from PIV. This is done so as to use all the samples obtained from the microphone and have higher number of points in the FFT. The time shift between the two signals i.e. τ is determined by the PIV frequency (for V30: 1/8000 s).

The contour plot of maximum values of the **normalized cross correlation function** $R_{v'p'}(X, Y, \tau)$ at all locations for all τ shift in the GF6-AOA8-V30 case is shown in Figure 5.19. The maximum value in the entire domain is $R_{v'p'}=0.53$. Such a high correlation

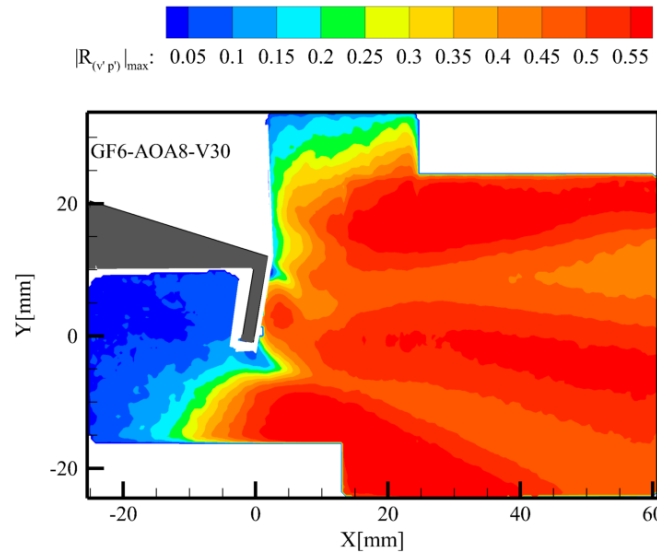


Figure 5.19: Maximum value of $R_{v'p'}(X, Y, \tau)$ for the GF6-AOA8-V30 (pressure side microphone)

value suggests there is a definite correlation between the velocity fluctuations in the downstream of the flap and the far-field noise. $R_{v'p'}(x, y, \tau)$ has almost zero value in the upstream separation bubble indicating this region is not the source region for the tonal noise. The same result is obtained for both the pressure side and the suction side microphone is used. Additionally, the contour plot also shows some high values slightly upstream below the flap. $R_{v'p'}$ also shows three distinct regions (peaks) where correlation value is high in the domain. The wake region has a high correlation because most of v' fluctuations are present in the wake. The reason for the other two peaks is not clear. They are most likely due to the flapping motion of the shear layers or due to the normalization by $v'_r m_s$.

Next, the partial correlation functions of $\langle \omega' p' \rangle$ with the out-of-plane component ω_z represented by $R_{\omega'p'}(x, y, \tau)$ and $\langle \omega' \times \mathbf{v}' \rangle \langle p' \rangle$, the x-component represented by $R_{\omega'v',p'}(x, y, \tau)$ is computed and the maximum values for all τ is shown in Figure 5.20. These correlation values are lower than $R_{v'p'}$. This is expected as the radiated sound is directly linked to the unsteady lift in the model which in turn is related to the unsteady vertical velocity in the wake. Interestingly, the higher values of correlation (two peaks) are also present in $R_{\omega'p'}$ and $R_{\omega'v',p'}$, with $R_{\omega'v',p'}$ showing slightly lower values also in the wake region.

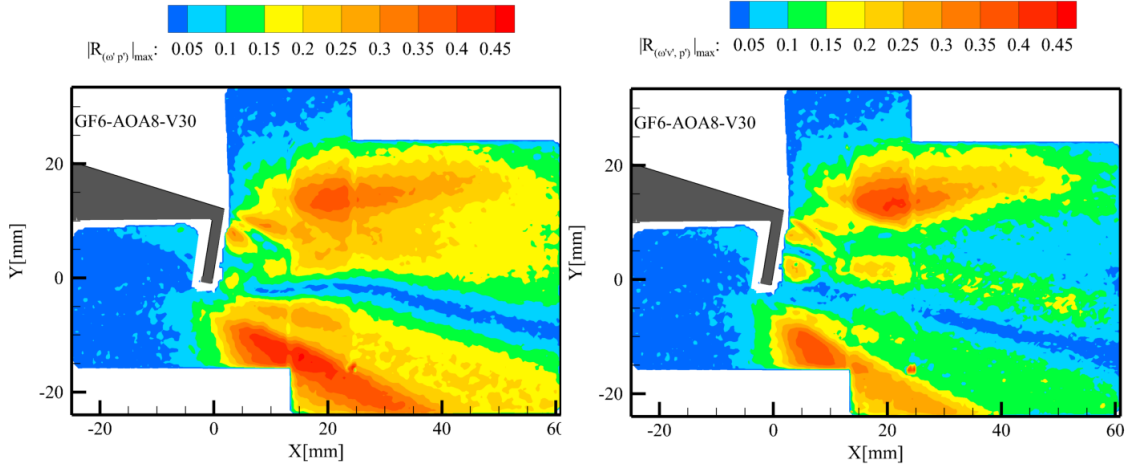


Figure 5.20: Maximum value of $R_{\omega'v',p'}(x, y, \tau)$, $R_{\omega'p'}(x, y, \tau)$ for GF6-AOA8-V30

Similar to the section on flow statistics, it is interesting to see the effect of Re , α and GF% size on maximum values of $R_{v'p'}$ in the domain. The three distinct regions of higher $R_{v'p'}$ appear in each of the cases as shown in Figure 5.21. Figure 5.21 also shows the influence of Re is quite small (top left, bottom left). While reducing the GF% size, the $R_{v'p'}$ values for the 4% flap are slightly higher. Increasing the angle of attack to $\alpha = 8^\circ$ results in a much higher value of $R_{v'p'}$ and the contour plot has three distinct peaks. Since $R_{v'p'}$ is normalised using v'_{rms} , p'_{rms} , referring back to Figure 5.7, lower v'_{rms} values for GF6-AOA8-V30 case can be the reason for higher values of $R_{v'p'}$ for this case.

As recently pointed by Henning et al (2014). there can be some ambiguity on the location of the ‘actual source’ based on the maximum values of $R_{v'p'}$ (Section). One has to be careful while concluding that higher values of correlation represent the ‘true source of sound’ since there can be significant correlation in structures downstream of the upstream ‘source of

sound'. Therefore the high values of correlation in the three peaks in Figure 5.21 does not necessary mean they are the 'sources', but they can also be due to an upstream source (in this case it is shown to be the flap). This is made clear when the correlation function as a function of τ shift, $R_{v'p'}(\tau)$, is calculated.

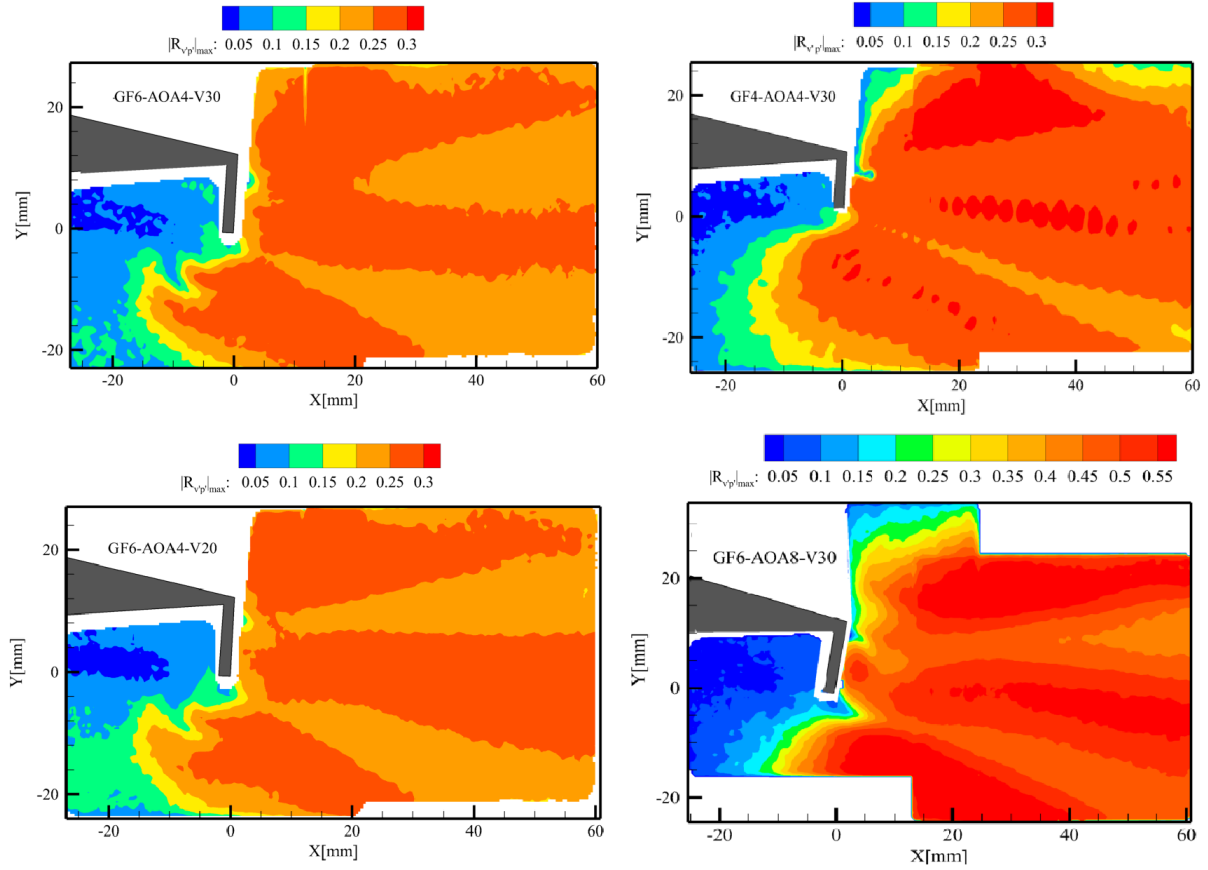


Figure 5.21: Maximum value of $R_{v'p'}(X, Y, \tau)$ by varying Re , α and GF %

In order to calculate $R_{v'p'}$ as a function of τ shift, it is important to first take into account the propagation time of acoustic waves to the microphone. First τ_0 i.e. the point where there is a zero lag between the two signals is calculated using correlation. The maximum value of correlation between the two signals is taken to be the 'starting point' of the two signals. This is done to take into account the propagation time as well as the delays caused due to human errors in acquiring the measurements in a synchronised manner. Figure 5.22 and Figure 5.23 shows $R_{v'p'}(\tau)$ calculated at a point C ($X, Y: 32.5, 5$) in the wake. The time shift τ is calculated in discrete steps with $\Delta\tau$ determined by the acquisition frequency of PIV (in the GF6-AOA8-V30 case: $1/8000 = 0.125\text{ms}$). The contour plot of $R_{v'p'}(\tau)$ at different τ shift is shown in Figure 5.24. Figure 5.24 shows shifting the pressure signal with respect to the v' fluctuations of the flow in the negative direction causes the correlation function to move in the downstream direction as indicated by letters A and B. $R_{v'p'}(\tau)$ also shows three distinct peaks with almost constant magnitude moving downstream.

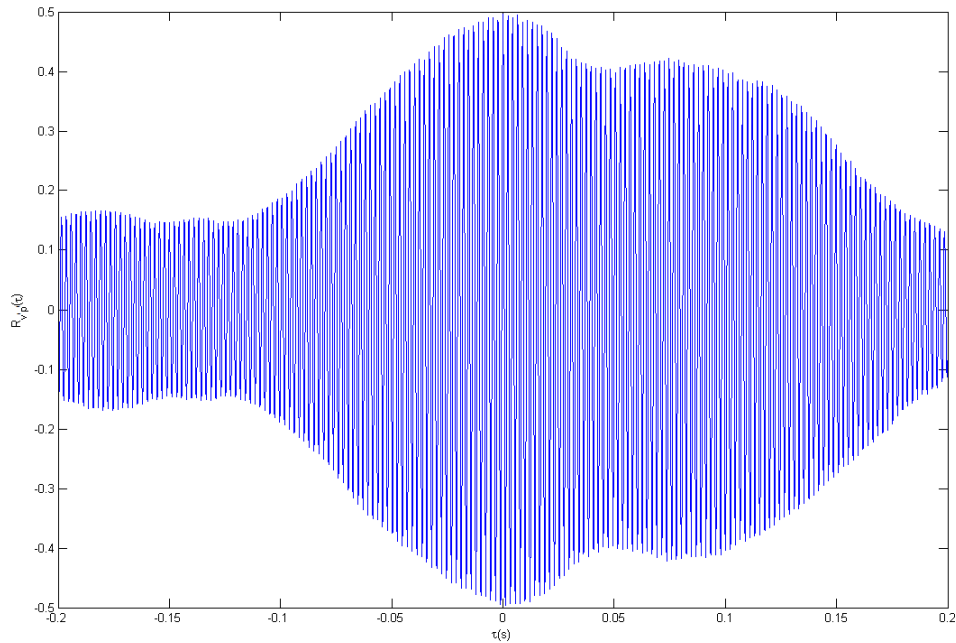


Figure 5.22: $R_{v'p'}(\tau)$ as a function of τ at Point C(X,Y:32.5,5) in the wake

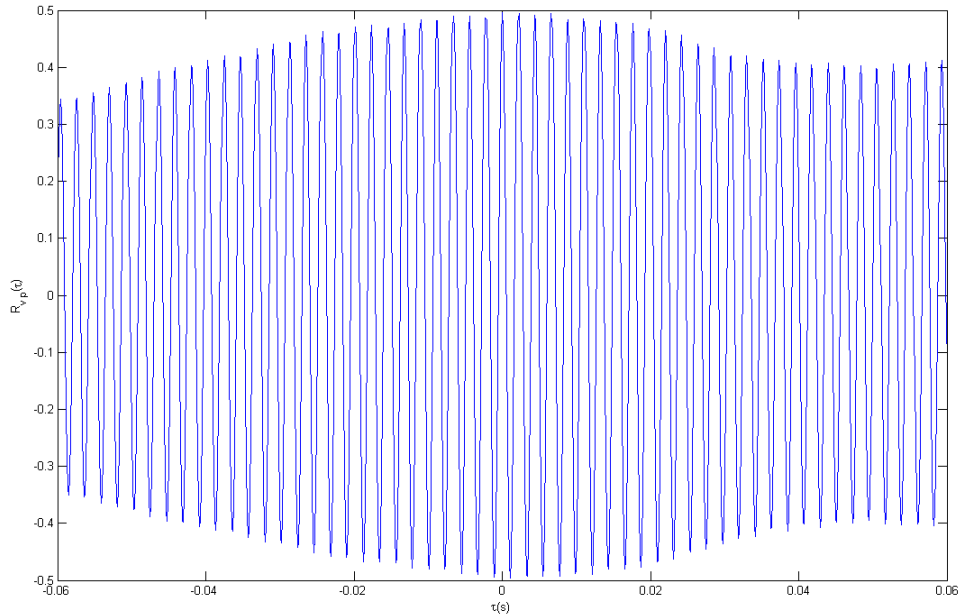


Figure 5.23: $R_{v'p'}(\tau)$ at Point C (zoomed in)

Due to the high temporal resolution of the measurements, on observing closely, Figure 5.24 shows that significant correlation seems to be originating from the flap which is expected to be the main source of sound. As mentioned in section 2.2 on aeroacoustics, at low Mach number

flows studied in the thesis the dipole term caused by unsteady pressure (or lift) fluctuations is the main dominant source. The high values of correlation in the downstream are therefore due to the presence of an upstream source and are not sources of sound themselves.

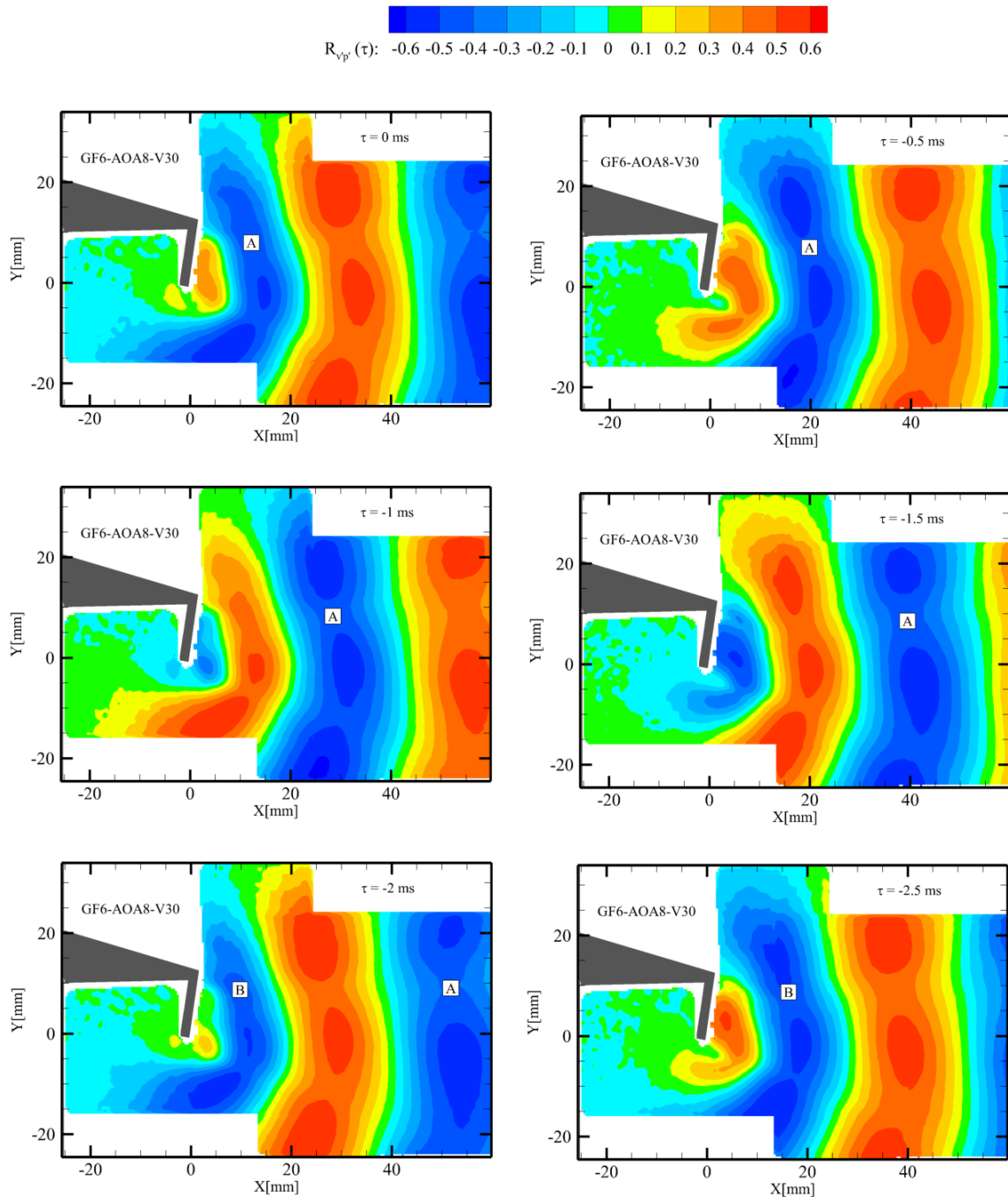


Figure 5.24: Contour plot of $R_{v'p'}(\tau)$ at different τ shift

On calculating correlation as a function of τ shift using vorticity (out-of-plane component ω_z), $R_{\omega'p'}(\tau)$, Figure 5.25 shows correlation values to be slightly lower than the one obtained from $R_{v'p'}(\tau)$ moving downstream indicated by A, B. The two peaks are opposite in sign due to the opposite vorticity shed from the lower and the upper shear layers. $R_{\omega'p'}(\tau)$ has a maximum value around $X=20\text{mm}$ ($x/c: 0.1$) from the flap and decreases further downstream. This is attributed to the rapid acceleration of vortices which takes place in this region.

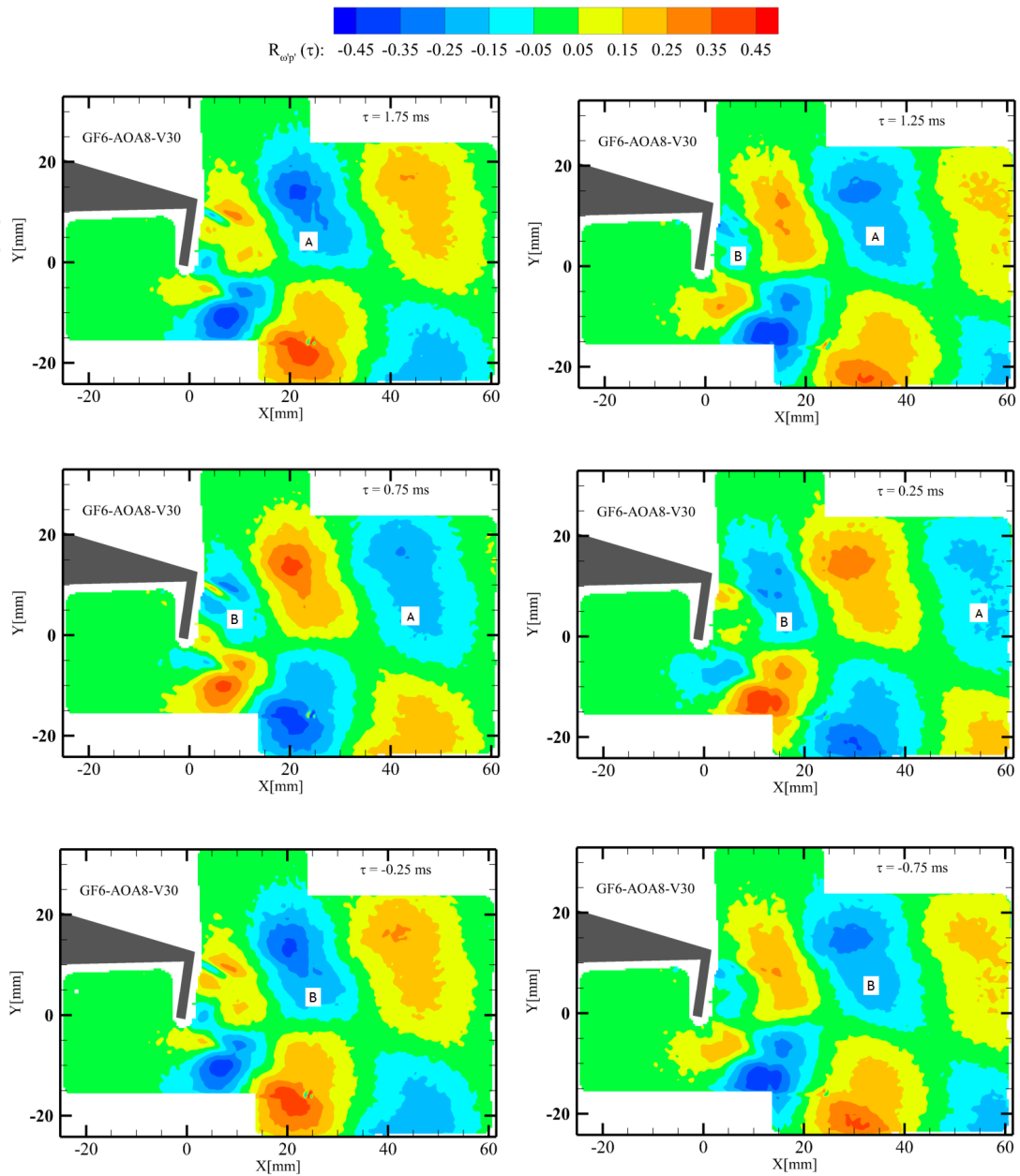


Figure 5.25: Contour plot of $R_{\omega'p'}(\tau)$ at different τ shift

The part of the Lamb vector $L = \boldsymbol{\omega} \times \boldsymbol{v}$ used to calculate the correlation is the x-component: $\omega_z v$. Figure 5.26 shows the correlation with far-field pressure fluctuations $R_{\omega'v',p'}(\tau)$. The correlation values are similar to $R_{\omega'v'}(\tau)$, some significant values are present in the wake. Here again, the correlation has a maximum at $x/c=0.1$ from the flap and decreases downstream. A pulsating motion originating from the flap can be observed. It is difficult to interpret the results correctly since only a small component of the Lamb vector is evaluated.

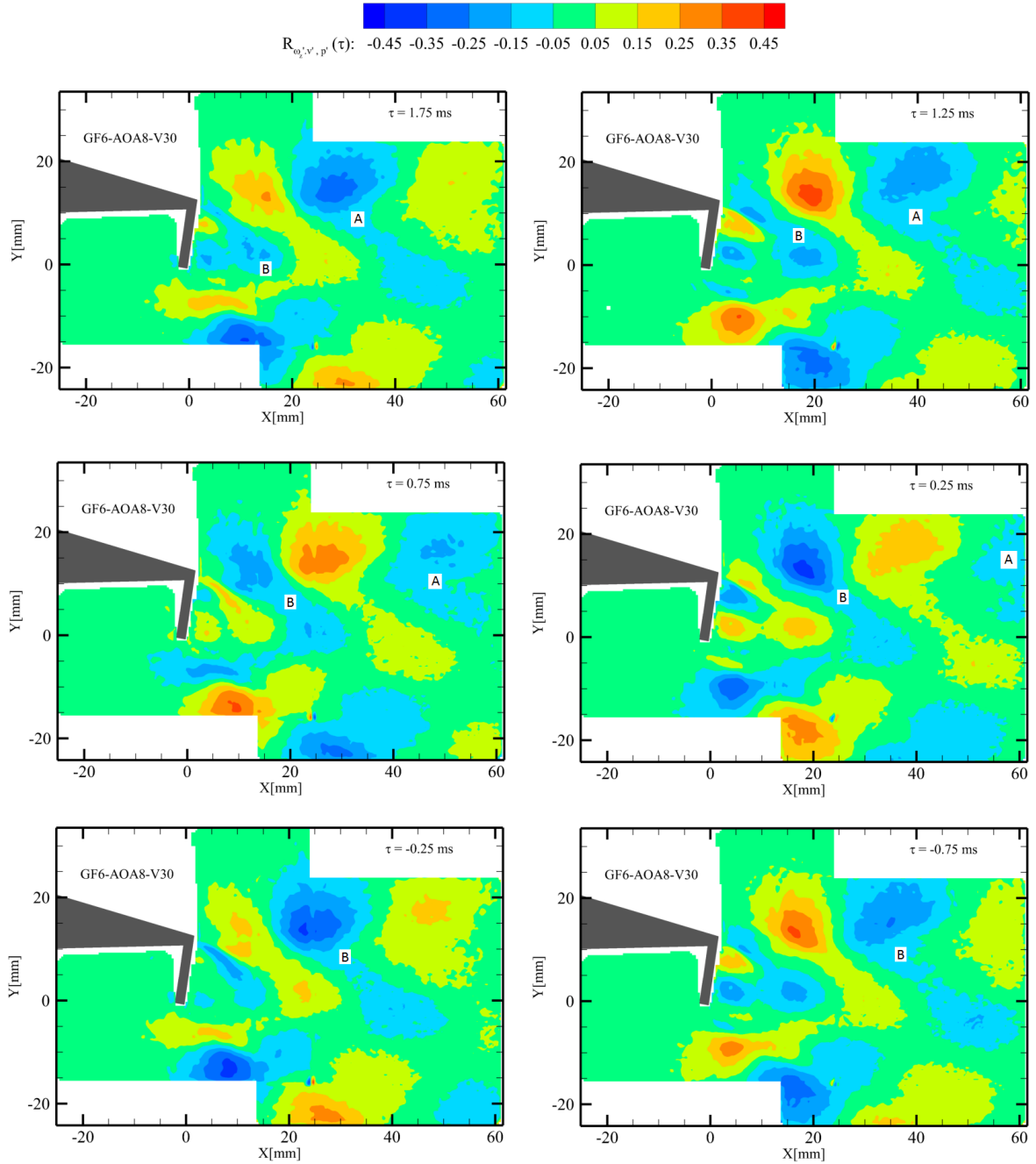


Figure 5.26: Contour plot of $R_{\omega'v',p'}(\tau)$ at different τ shift

Here videos of the correlations can be seen in the pdf version available online (<http://repository.tudelft.nl/>).

The correlations calculated above indicate that a strong causal relationship exists between the unsteady lift forces on the surface to the far-field pressure fluctuations in the case of a Gurney flap. In the end it turns out that aerocoustics of a Gurney flap is similar to the aeolian tone produced by a cylinder in a flow.

However, when one asks if it is the surface of the flap or the vortex shedding that is the actual source that produces the tone? The explanation given by Hirschberg [79] is apt,

“Although convected vorticity is silent (it exists without pressure fluctuations) its presence may still be acoustically important. Near a solid surface (typically the surface from which the vorticity is shed) the velocity corresponding to the free vorticity cannot exist, as the field has to satisfy the vanishing normal velocity condition. This induces a fluctuating pressure along the surface which radiates out as sound, apparently from the surface but of course really the vorticity is the source. Examples are the whistling sound produced by a thin pipe or wire in the wind (aeolian sound), and the trailing edge noise-as far as it is due to shed-vorticity -from

a blunt-edged airfoil.”

The role of surfaces in scattering the acoustics, however, is very important and cannot be ignored. This brings us to a major limitation of the causality correlation technique which does not account for the surfaces. A possible improvement will be incorporating the surfaces via Green’s function in the causality correlation approach.

5.7 Coherence

A drawback in correlating two signals in the time domain to see their linear dependence is that correlation does not distinguish the signals in terms of different frequencies. So uncorrelated parts of the signals can bring down the overall magnitude of the correlation coefficient. On the other hand, coherence/normalised cross-power spectral density can be used to see the frequency dependence of the signals. So only the part of the signal of the same frequency can essentially be used in computing their dependence which can result in a higher value than the normalised cross-correlation coefficient. Section 3.4 explained the method in which spectral coherence is calculated. Figure 5.27 shows the magnitude square-coherence $\gamma_{v',p'}^2$ calculated for the shedding frequency for the GF6-AOA8-V30 case. The values obtained are slightly higher than the $R_{v',p'}$. The contour plot $\gamma_{v',p'}$ also shows very low values in the upstream recirculation region. While downstream of the Gurney flap, $\gamma_{v',p'}^2$ is almost equal everywhere in the domain.

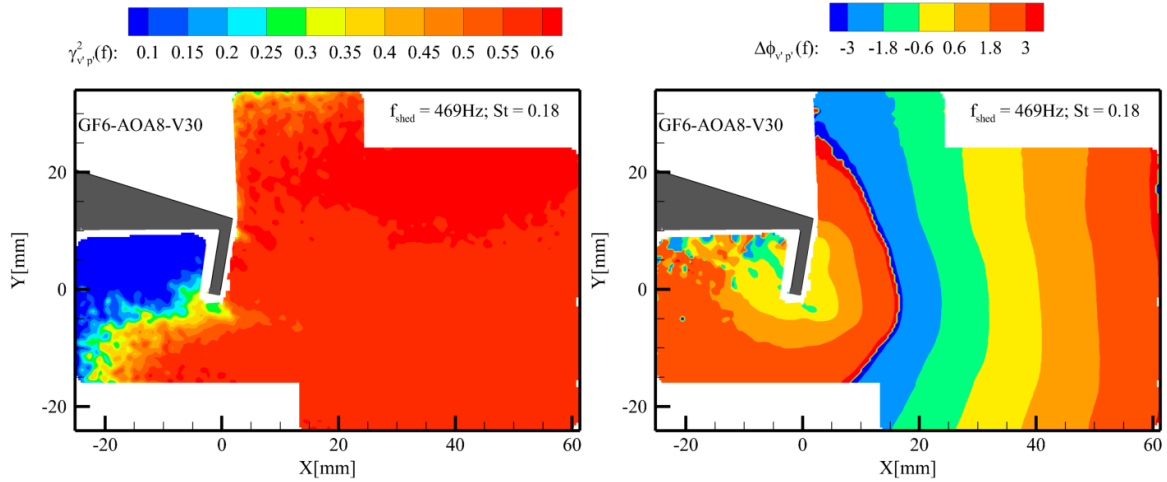


Figure 5.27: Contour plot of the magnitude square-coherence $\gamma_{v',p'}^2$ at shedding frequency and the corresponding phase difference plot

The phase difference between the v' , p' fluctuations is calculated using the argument of $\gamma_{v',p'}$. Figure 5.27 shows the phase difference obtained for the shedding frequency which varies from $-\pi$ to π . The convective velocity of the large scale coherent flow structures is evaluated by

calculating the wavelength from the phase difference plot, and the known shedding frequency. The values obtained are $\lambda \approx 0.045m$ giving $U_c = 21.1m/s$ or $U_c/U_\infty = 0.7$.

5.8 Spanwise correlation length: Stereoscopic PIV

Since it is clear that the tonal noise restricted to a narrow band of frequency produced by the Gurney flap is due to the vortex shedding. Such large scale vortex shedding consist of coherent structures along the spanwise direction and thus have a large spanwise correlation length as found in flows which involve trailing edge bluntness noise [78]. A good definition which helps in understanding the meaning of a coherent motion is the one defined by Robinson (1991), a coherent motion is:

”A three dimensional region of the flow over which at least one fundamental flow variable (velocity component, density, temperature etc.) exhibits significant correlation with itself or with another variable over a range of space and/or time that is significantly larger than the smallest local scales of the flow.”

To evaluate this spanwise correlation length, stereoscopic PIV in a downstream plane parallel to the Gurney flap is carried out (Figure 5.29). This correlation length (actually the spanwise coherence length for different frequencies) can be used for accurate prediction of noise as shown by Lorenzoni *et al.* [59].

Figure 5.28: Schematic showing the v component for the GF6-AOA4-V20 case (video available in the online version)

The streamwise mean flow \bar{u} for the GF6-AOA4-V30 case is shown in Figure 5.28. A higher velocity on the suction side as compared to the pressure side is seen. The mean velocity in

the wake is also seen clearly.

Here again, cross-correlation between the v' fluctuations between two points (separated by Δz) along the span is carried out. Figure 5.30 shows the spanwise correlation for $V = 30m/s$ and $V = 20m/s$. Due to a smaller FOV, the spanwise correlation plot is approximated with a Gaussian distribution using the least squares method. The spanwise correlation length is the integral of the spanwise correlation coefficient over the span which turns out to be 4.1cm for the V30 case and 2.75cm for the V20 case. Although higher Reynolds number flows has more turbulence associated with it and one might expect lower correlation lengths, the higher correlation length is possibly due to higher energy of the vortical structures.

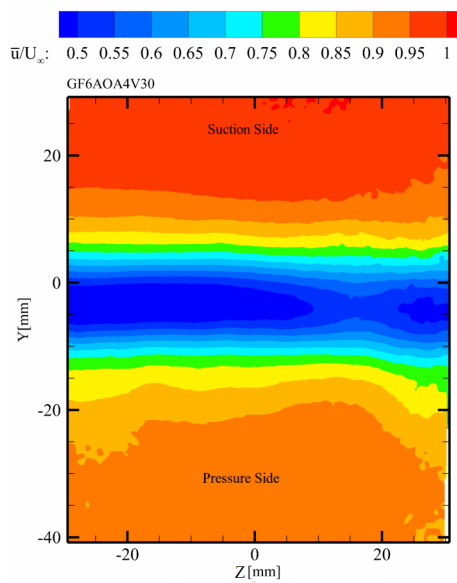


Figure 5.29: Streamwise mean flow, \bar{u} for GF6-AOA4-V30 case

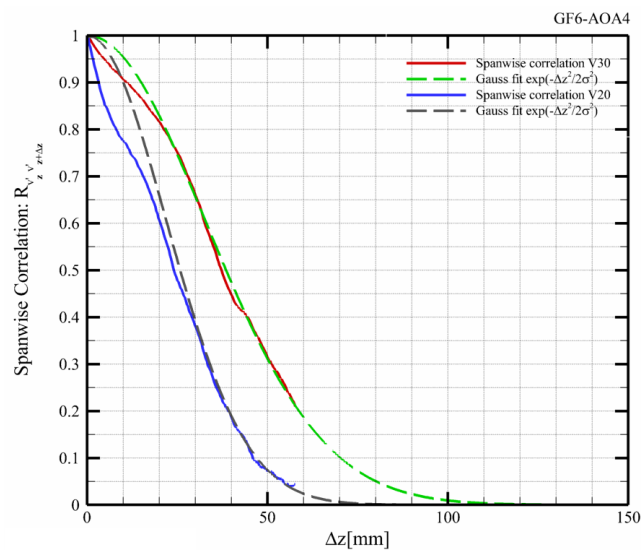


Figure 5.30: Spanwise Correlation length obtained for GF6-AOA4-V20/30 cases

Chapter 6

Conclusions

No amount of experimentation can ever prove me right; a single experiment can prove me wrong.

Albert Einstein

Time-resolved particle image velocimetry as seen throughout the thesis provides an enhanced quantitative description of the flow. TR-PIV was used to obtain, at a high spatial and temporal resolution, the flow dynamics associated with a Gurney flap at low Mach and high Reynolds number. A part of the thesis focussed on validating the two modes of shedding as an additional lift increment mechanism in a Gurney flap in case of a fully developed turbulent boundary layer. A major part of the thesis focussed on the aeroacoustic investigation of a Gurney flap as a “precursor” to understanding noise in complex flaps used in the aerospace industry. To understand the mechanism of noise generation the *causality correlation* approach was used. In the first phase of the thesis, *non-simultaneous* measurements of the flow using TR-PIV and acoustics using microphones were carried out. An assumption that the vortex shedding which resulted in a tonal peak in the acoustic spectra was in essence a periodic phenomena was made. However, poor quality results of correlation and coherence were obtained that were mostly attributed to random phase changes in the shedding process. Since an uncertainty in the angle of attack was to be avoided i.e. testing in an open jet, a method which allowed laser light to pass through an acoustically transparent material such as Kevlar as a part of a closed test section was used in the second phase. In this phase, *simultaneous* measurements of the flow and acoustics were successfully carried out. The main conclusions keeping in mind the research objectives provided in section 2.3 on the flow dynamics and aeroacoustics are summarized below.

Flow Dynamics:

The flow structure surrounding a Gurney flap was successfully visualized and quantified by

obtaining TR-PIV measurements at acquisition frequencies as high as 8kHz. Flow statistics showed an upstream recirculation region, upper and lower separating shear layers and a main recirculation region whose size varied with Gurney flap size and angle of attack downstream of the flap. The instantaneous velocity and vorticity fields showed the flapping motion of the von Kármán wake and corresponding vortex roll-up and shedding process. It was found that the shedding mechanism in a Gurney flap was similar to that of a bluff body as explained by Gerrad. Hence, the Strouhal numbers of the vortex shedding for various Gurney flaps were close to that of a bluff body in a flow. The power spectral density of flow fluctuations as well as the acoustic spectra, however, did not indicate any second mode of shedding. Proper orthogonal decomposition modes indicate periodic vortical structures convecting downstream as well as a flapping motion present in the wake. Thus, in presence of a turbulent boundary layer and for flows at Reynolds number 0.25-0.4 million, the mechanism that a Gurney flap produces additional lift due to increased circulation caused by second mode of shedding is found to be not true. The convective velocity U_c of the vortices downstream was evaluated using the concept of coherence. As measured by Stereoscopic PIV, the periodic vortex shedding is found to be highly correlated in the spanwise direction (correlation length of 4cm for the GF6-AOA4-V30 case) simplifying the problem to 2D thereby showing that accurate results can be obtained using planar PIV. The large spanwise correlation length also indicate add-ons such as serrations could be useful in breaking-down such coherent structures.

Aeroacoustics:

In the case of a Gurney flap, the tonal peaks were clearly audible and correspond to the vortex shedding frequency. The acoustic spectra showed the Strouhal number corresponding to the shedding frequency remained almost constant when the Reynolds number is varied, while increasing the angle of attack decreased the Strouhal number due to an increase in boundary layer thickness. Decreasing the flap size led to an increase in the shedding frequency and a decrease in the Strouhal number due to the reduction in the vertical distance between the separating shear layers.

Causality correlation is an advanced noise source diagnostics technique applied in the thesis that takes into account the integrated information of pressure fluctuations generated in the far-field and relates it to the near-field fluctuations. The maximum normalised correlation values between the far-field pressure fluctuations and v' i.e. $R_{v'p'}(X, Y)$ are found to be in the range of 0.3-0.6 in the *downstream* region of the flap for different cases. It is highest for the GF6-AOA8-V30 case $R_{v'p'}=0.55$. The dynamics in the upstream recirculation region was not responsible in the production of noise. In all cases, three distinct peaks in the wake region and two others where higher correlation values of $R_{v'p'}$ in the domain were found. The other two peaks are possibly due to the flapping motion of the von Kármán wake. As acoustic sources are essentially due to unsteady turbulent motions, TR-PIV measurements proved to be insightful when the normalised correlation coefficient $R_{v'p'}(X, Y, \tau)$ is computed. The results indicate the location of the actual source of noise to be the flap, which is expected, considering that at low Mach numbers the dipole term associated with the unsteady surface pressure (or lift) has the main contribution to noise. The high values of correlation further downstream are due to the presence of an upstream source (the flap) and are not sources of sound themselves. Thus, TR-PIV in a way clears the ambiguity expressed by other researchers in the past in interpreting the high values of correlation to be sources of sound. Limitations of the causality correlation technique are that correlation mathematically is used

to see if a ‘linear’ relationship exists between two variables and more importantly does not incorporate ‘surfaces’ which play a very important role in scattering the sound. Current efforts by the group of Henning are in developing novel methods such as intensity analysis that use these simultaneous measurements to identify regions in turbulent flows involved in high production of fluctuating energy that radiate acoustic perturbations.

As a continuation of the current thesis, two key areas of further research are identified:

- **Pressure reconstruction and far-field noise estimation**

A Poisson solver is one of the methods that can be applied to reconstruct pressure from the velocity data (Van Oudheusden [80]). The pressure obtained can be used with acoustic analogies to predict far-field noise. The predicted acoustic fluctuations can then be compared (and correlated) to the microphone data obtained in the far-field. Further, unsteady lift can be obtained using PIV and can also be used for far-field noise prediction (Gutin’s principle).

- **Application to complex flaps: Flap side edge noise**

Several studies on this topic have been done in the past, for example Angland [81]. It is believed that the noise is generated by the unsteady and highly turbulent tip vortices. There is a good potential in applying the causality correlation technique to flap side edge noise to identify flow structures in the region that are highly correlated with noise. This makes newer designs of flaps with low-acoustic emissions possible. The photographs (Figure 6.1) captured by the author indicate flap side edge noise during landing indicated by the low pressure area behind the flaps (easily identified by the condensation of water vapour).



(a)

(b)

Figure 6.1: Flap side edge noise: Transavia flight landing at Rotterdam Airport

Appendix

Non-simultaneous measurements

Poor quality results of causality correlation are obtained when non-simultaneous measurements of flow and acoustics are carried out. It is found that the high Reynolds number flow considered in the thesis causes random phase changes in the vortex shedding process, bringing the overall values of correlation down as shown in Figure 6.2.

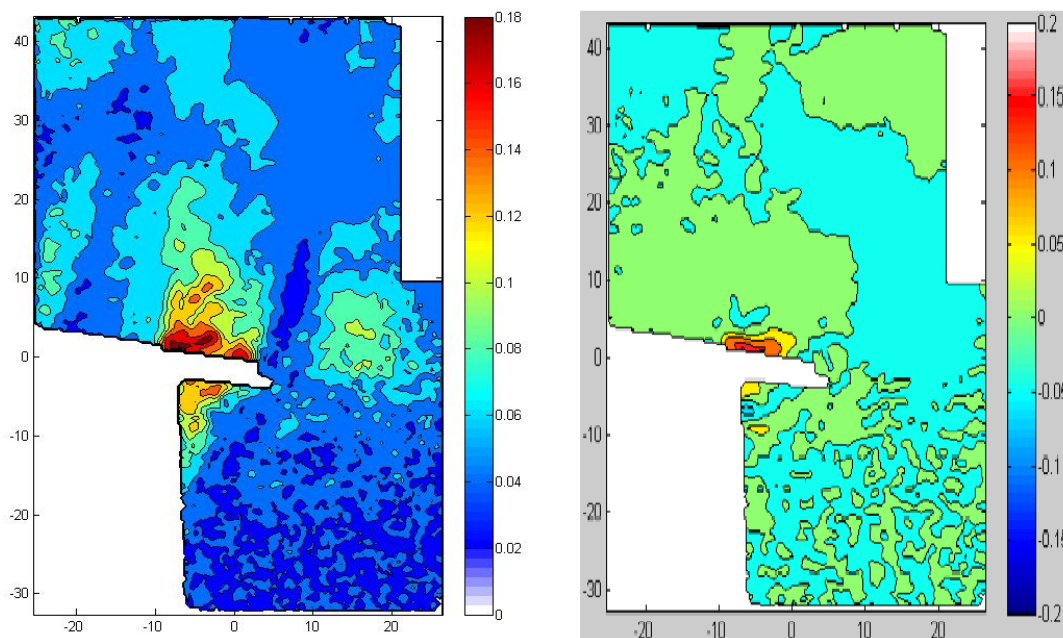


Figure 6.2: Non-simultaneous measurement GF6-AOA8-V30: Maximum value of $R_{v'p'}$ and as a function of τ , $R_{v'p'}(\tau)$

Simultaneous measurement: Zoomed in case

Few zoomed in measurements near the flap are carried out using a 200mm lens. Similar results as seen in the thesis for $R_{v',p'}$, $R_{v',p'}(\tau)$, $\gamma_{v',p'}$ and phase difference are obtained for the GF4-AOA4-V20 case as shown in Figure 6.3.

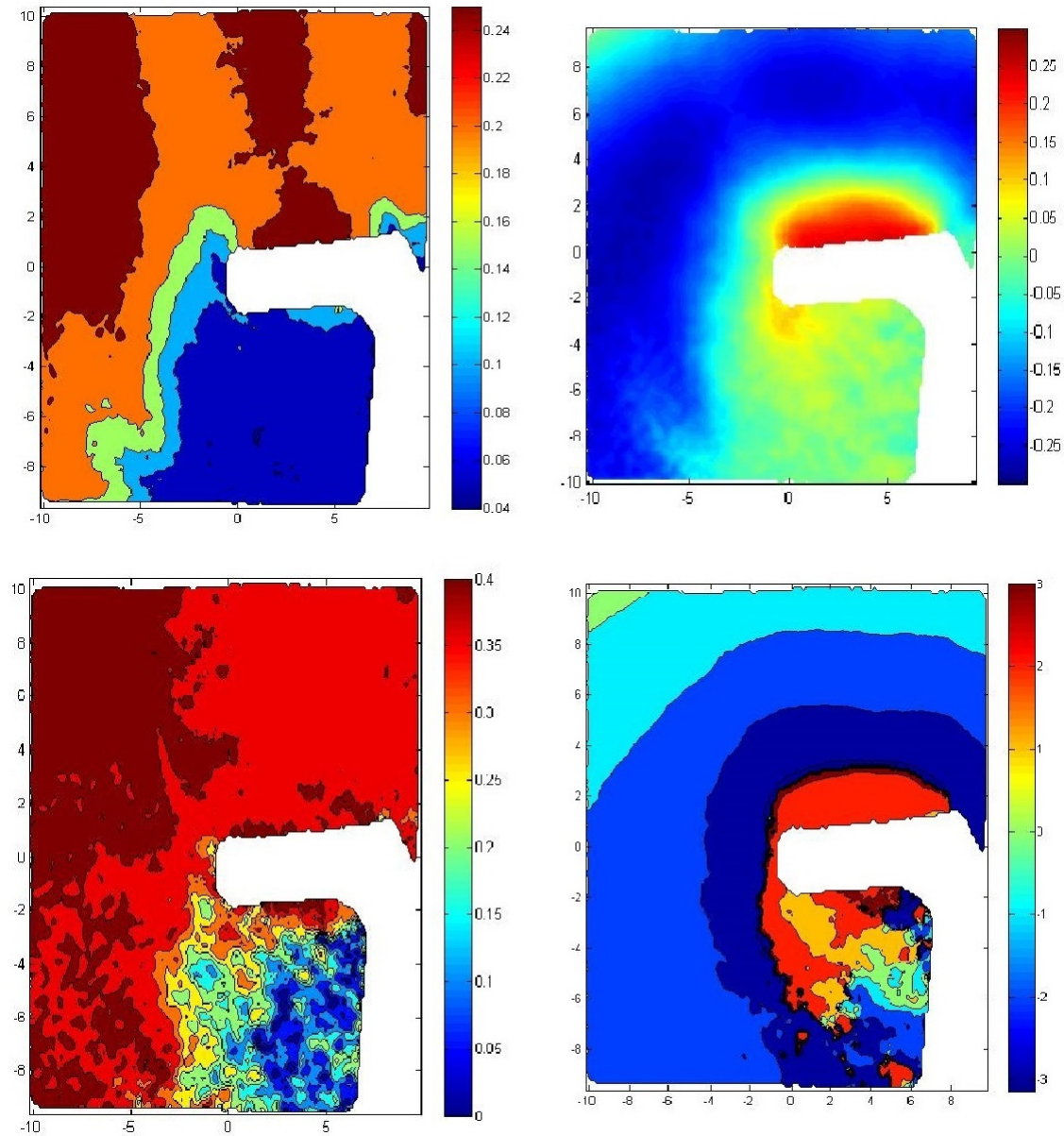


Figure 6.3: Simultaneous measurement, Correlation - Maximum value of $R_{v',p'}$ (top left) and $R_{v',p'}(\tau)$ (top right), Coherence: $\gamma_{v',p'}$ at shedding frequency and the corresponding phase difference plot

Bibliography

- [1] Wikipedia. Takeoff and landing — wikipedia, the free encyclopedia, 2015. [Online; accessed 13-October-2015].
- [2] Stefan Oerlemans. *Detection of aeroacoustic sound sources on aircraft and wind turbines*. University of Twente, 2009.
- [3] H Ising, B Kruppa, et al. Health effects caused by noise: evidence in the literature from the past 25 years. *Noise and Health, Inter-disciplinary International Journal*, 6(22):5, 2004.
- [4] International civil aviation organization(icao), environmental report 2013.
- [5] W Schröder. Aeroacoustics research in europe: The ceas-asc report on 2003 highlights. *Journal of sound and vibration*, 278(1):1–19, 2004.
- [6] Nicolas E Antoine and Ilan M Kroo. Aircraft optimization for minimal environmental impact. *Journal of aircraft*, 41(4):790–797, 2004.
- [7] John-Paul Clarke. The role of advanced air traffic management in reducing the impact of aircraft noise and enabling aviation growth. *Journal of Air Transport Management*, 9(3):161–165, 2003.
- [8] Wolfgang Neise. Engines as pacemakers for reduction of noise and emission, 2004.
- [9] R Vos. Advanced aircraft design i, lecture notes msc course, 2011.
- [10] Porsche Gurney flap. Rennlist.com, 2015.
- [11] Wikipedia. Gurney flap — wikipedia, the free encyclopedia, 2015. [Online; accessed 9-October-2015].
- [12] H Lee and Ilan M Kroo. Two dimensional unsteady aerodynamics of miniature trailing edge effectors. *AIAA paper*, 1057:9–12, 2006.
- [13] H.T. Lee, S.R. Bieniawski, and I.M. Kroo. Miniature trailing edge effector for aerodynamic control, August 12 2008. US Patent 7,410,133.
- [14] Scott J Johnson, Jonathon P Baker, CP Van Dam, and Dale Berg. An overview of active load control techniques for wind turbines with an emphasis on microtabs. *Wind Energy*, 13(2-3):239–253, 2010.

- [15] JR Zayas, CP van Dam, R Chow, JP Baker, and EA Mayda. Active aerodynamic load control for wind turbine blades. In *European Wind Energy Conference*. Athens, Greece, 2006.
- [16] JAC Kentfield. The potential of gurney flaps for improving the aerodynamic performance of helicopter rotors. In *AIAA international powered lift conference*, pages 283–292, 1993.
- [17] Philippe Gigu-ccedil, re, Guy Dumas, and Jean Lemay. Gurney flap scaling for optimum lift-to-drag ratio. *AIAA journal*, 35(12):1888–1890, 1997.
- [18] Yachen Li, Jinjun Wang, and Panfeng Zhang. Effects of gurney flaps on a naca0012 airfoil. *Flow, turbulence and combustion*, 68(1):27–39, 2002.
- [19] Bruce L Storms and Cory S Jang. Lift enhancement of an airfoil using a gurney flap and vortex generators. *Journal of Aircraft*, 31(3):542–547, 1994.
- [20] Yachen Li, Jinjun Wang, and Panfeng Zhang. Influences of mounting angles and locations on the effects of gurney flaps. *Journal of Aircraft*, 40(3):494–498, 2003.
- [21] Mark D Maughmer and Götz Bramesfeld. Experimental investigation of gurney flaps. *Journal of Aircraft*, 45(6):2062–2067, 2008.
- [22] David Jeffrey, Xin Zhang, and David W Hurst. Aerodynamics of gurney flaps on a single-element high-lift wing. *Journal of Aircraft*, 37(2):295–301, 2000.
- [23] Cory S Jang, James C Ross, and Russell M Cummings. Numerical investigation of an airfoil with a gurney flap. *Aircraft Design*, 1(2):75, 1998.
- [24] Roy Myose, Michael Papadakis, and Ismael Heron. Gurney flap experiments on airfoils, wings, and reflection plane model. *Journal of Aircraft*, 35(2):206–211, 1998.
- [25] Bruce L Storms and James C Ross. Experimental study of lift-enhancing tabs on a two-element airfoil. *Journal of aircraft*, 32(5):1072–1078, 1995.
- [26] Yachen Li and Jinjun Wang. Experimental studies on the drag reduction and lift enhancement of a delta wing. *Journal of aircraft*, 40(2):277–281, 2003.
- [27] Julia A Cole, Bernardo AO Vieira, James G Coder, Amandeep Premi, and Mark D Maughmer. Experimental investigation into the effect of gurney flaps on various airfoils. *Journal of Aircraft*, 50(4):1287–1294, 2013.
- [28] JJ Wang, YC Li, and K-S Choi. Gurney flaplift enhancement, mechanisms and applications. *Progress in Aerospace Sciences*, 44(1):22–47, 2008.
- [29] Robert H Liebeck. Design of subsonic airfoils for high lift. *Journal of aircraft*, 15(9):547–561, 1978.
- [30] Danh Neuhart and Odisc Pendergraft. A water tunnel study of gurney flaps. 1988 [NASA TM-4071].
- [31] JH Gerrard. The mechanics of the formation region of vortices behind bluff bodies. *Journal of Fluid Mechanics*, 25(02):401–413, 1966.

- [32] DR Troolin, EK Longmire, and WT Lai. Time resolved piv analysis of flow over a naca 0015 airfoil with gurney flap. *Experiments in Fluids*, 41(2):241–254, 2006.
- [33] Daniel Troolin. *A quantitative study of the lift-enhancing flow field generated by an airfoil with a Gurney flap*. PhD thesis, University of Minnesota, 2009.
- [34] Tianshu Liu and Javier Montefort. Thin-airfoil theoretical interpretation for gurney flap lift enhancement. *Journal of Aircraft*, 44(2):667–671, 2007.
- [35] Michael J Lighthill. On sound generated aerodynamically. i. general theory. *Proceedings of the Royal Society of London. Series A. Mathematical and Physical Sciences*, 211(1107):564–587, 1952.
- [36] N Curle. The influence of solid boundaries upon aerodynamic sound. *Proceedings of the Royal Society of London. Series A. Mathematical and Physical Sciences*, 231(1187):505–514, 1955.
- [37] Alan Powell. Theory of vortex sound. *The journal of the acoustical society of America*, 36(1):177–195, 1964.
- [38] JE Ffowcs Williams and David L Hawkings. Sound generation by turbulence and surfaces in arbitrary motion. *Philosophical Transactions of the Royal Society of London A: Mathematical, Physical and Engineering Sciences*, 264(1151):321–342, 1969.
- [39] Michael S Howe. *Theory of vortex sound*, volume 33. Cambridge University Press, 2003.
- [40] Tim Colonius and Sanjiva K Lele. Computational aeroacoustics: progress on nonlinear problems of sound generation. *Progress in Aerospace sciences*, 40(6):345–416, 2004.
- [41] Meng Wang, Jonathan B Freund, and Sanjiva K Lele. Computational prediction of flow-generated sound. *Annu. Rev. Fluid Mech.*, 38:483–512, 2006.
- [42] Christophe Schram. *Prediction of the Sound Produced by Vortex Pairing based on Particle Image Velocimetry*. PhD thesis, TU Eindhoven, VKI, ULB, 2003.
- [43] Michael Gloor, Stefan Bühler, and Leonhard Kleiser. Flow dynamics and aeroacoustics of heated coaxial jets at subsonic mach numbers. In *20th AIAA/CEAS Aeroacoustics Conference. Atlanta, GA, DOI*, volume 10, pages 6–2014, 2014.
- [44] Avraham Hirschberg and Christophe Schram. A primitive approach to aeroacoustics. In *Sound-Flow Interactions*, pages 1–30. Springer, 2002.
- [45] Jie-Zhi Wu, Hui-Yang Ma, and M-D Zhou. *Vorticity and vortex dynamics*. Springer Science & Business Media, 2007.
- [46] Markus Raffel, Christian E Willert, Jürgen Kompenhans, et al. *Particle image velocimetry: a practical guide*. Springer, 2013.
- [47] RJ Adrian and J Westerweel. *Particle Imaging Velocimetry*. Cambridge University Press, 2010.
- [48] F Scarano. Flow measurement techniques, lecture notes msc course, 2011.

- [49] J Westerweel. Fundamentals of digital particle image velocimetry. *Measurement science and technology*, 8(12):1379, 1997.
- [50] Ajay K Prasad. Stereoscopic particle image velocimetry. *Experiments in fluids*, 29(2):103–116, 2000.
- [51] Georg Eitelberg. Experimental simulations, lecture notes msc course, 2013.
- [52] P Sijtsma. Acoustic beamforming for the ranking of aircraft noise. 2012.
- [53] Daniele Violato. *3D flow organization and dynamics in subsonic jets*. PhD thesis, TU Delft, 2013.
- [54] Dushyant Parkhi. Aeroacoustics of cavity flow using time-resolved particle image velocimetry, msc thesis, 2009.
- [55] Valentina Koschatzky. *An experimental study on the aeroacoustics of wall-bounded flows: Sound emission from a wall-mounted cavity, coupling of time-resolved PIV and acoustic analogies*. TU Delft, Delft University of Technology, 2011.
- [56] Christian Haigermoser. Application of an acoustic analogy to piv data from rectangular cavity flows. *Experiments in fluids*, 47(1):145–157, 2009.
- [57] Daniele Violato and Fulvio Scarano. Three-dimensional evolution of flow structures in transitional circular and chevron jets. *Physics of Fluids (1994-present)*, 23(12):124104, 2011.
- [58] F Scarano. Tomographic piv: principles and practice. *Measurement Science and Technology*, 24(1):012001, 2013.
- [59] V Lorenzoni, M Tuinstra, and F Scarano. On the use of time-resolved particle image velocimetry for the investigation of rod–airfoil aeroacoustics. *Journal of Sound and Vibration*, 331(23):5012–5027, 2012.
- [60] Arne Henning, Kristian Kaepernick, Klaus Ehrenfried, Lars Koop, and Andreas Dillmann. Investigation of aeroacoustic noise generation by simultaneous particle image velocimetry and microphone measurements. *Experiments in fluids*, 45(6):1073–1085, 2008.
- [61] TE Siddon. Noise source diagnostics using causality correlations. *AGARD CP*, 131:7–1, 1973.
- [62] Hie K Lee and HS Ribner. Direct correlation of noise and flow of a jet. *The Journal of the Acoustical Society of America*, 52(5A):1280–1290, 1972.
- [63] M Schaffar. Direct measurements of the correlation between axial in-jet velocity fluctuations and far field noise near the axis of a cold jet. *Journal of Sound and Vibration*, 64(1):73–83, 1979.
- [64] Patrick M Hurdle, WC Meecham, and Brent K Hodder. Investigation of the aerodynamic noise generating region of a jet engine by means of the simple source fluid dilatation model. *The Journal of the Acoustical Society of America*, 56(6):1708–1721, 1974.

- [65] J Panda, RG Seasholtz, and KA Elam. Investigation of noise sources in high-speed jets via correlation measurements. *Journal of Fluid Mechanics*, 537:349–385, 2005.
- [66] A Henning, L Koop, and K Ehrenfried. Simultaneous particle image velocimetry and microphone array measurements on a rod-airfoil configuration. *AIAA journal*, 48(10):2263–2273, 2010.
- [67] Arne Henning, Andreas Schröder, Ingo Krebs, and Janos Agocs. Aeroacoustic investigations on a cold jet by means of simultaneous piv and microphone measurements. In *Proceedings of the 15th international symposium on applications of laser techniques to fluid mechanics, Lisbon, Portugal*, 2010.
- [68] Arne Henning, Björn Wrede, and Reinhard Geisler. Aeroacoustic investigation of a high-lift device by means of synchronized piv and microphone measurements. In *16th Int Symp on Applications of Laser Techniques to Fluid Mechanics, Lisbon 2012*, 2012.
- [69] Atsushi Nashimoto, Tsuneo Akuto, Yuichi Nagase, Takeshi Yoda, Tomonori Nakano, and Nobuyuki Fujisawa. Detection of aerodynamic noise sources over a rotating radiator fan blade for automobile. Technical report, SAE Technical Paper, 2007.
- [70] Arne Henning, Björn Wrede, and Andreas Schröder. About the ambiguity of noise source localization based on the causality correlation technique. In *17th Int Symp on Applications of Laser Techniques to Fluid Mechanics, Lisbon 2014*, 2014.
- [71] David ES Breakey, John A Fitzpatrick, and Craig Meskell. Aeroacoustic source analysis using time-resolved piv in a free jet. *Experiments in fluids*, 54(5):1–16, 2013.
- [72] Gal Berkooz, Philip Holmes, and John L Lumley. The proper orthogonal decomposition in the analysis of turbulent flows. *Annual review of fluid mechanics*, 25(1):539–575, 1993.
- [73] Knud Erik Meyer, Jakob M Pedersen, and Oktay Özcan. A turbulent jet in crossflow analysed with proper orthogonal decomposition. *Journal of Fluid Mechanics*, 583:199–227, 2007.
- [74] Stefan Pröbsting. Coherent structures at the serrated trailing-edge of a naca 0012, msc thesis, 2011.
- [75] Maarten Debrouwere. An assessment of acoustically transparent wind tunnel walls, msc thesis, 2013.
- [76] Frank M White and Isla Corfield. *Viscous fluid flow*, volume 3. McGraw-Hill New York, 2006.
- [77] Stephen B Pope. *Turbulent flows*. Cambridge university press, 2000.
- [78] Stefan Pröbsting. *Airfoil Self-Noise*. PhD thesis, TU Delft, 2015.
- [79] Sjoerd W Rienstra and Avraham Hirschberg. An introduction to acoustics. *Eindhoven University of Technology*, 18:19, 2003.
- [80] BW Van Oudheusden. Piv-based pressure measurement. *Measurement Science and Technology*, 24(3):032001, 2013.

- [81] David England. *Aerodynamics and aeroacoustics of flap side-edges*. PhD thesis, University of Southampton, 2008.

